

UNIVERSITY OF CALIFORNIA

Los Angeles

A New Tool for Cold Ion-Molecule Chemistry

A dissertation submitted in partial satisfaction  
of the requirements for the degree  
Doctor of Philosophy in Physics

by

Gary Chen

2019

© Copyright by

Gary Chen

2019

ABSTRACT OF THE DISSERTATION

A New Tool for Cold Ion-Molecule Chemistry

by

Gary Chen

Doctor of Philosophy in Physics

University of California, Los Angeles, 2019

Professor Wes Campbell, Chair

The dissertation of Gary Chen is approved.

Eric Hudson

Paul Hamilton

James Larkin

Wes Campbell, Committee Chair

University of California, Los Angeles

2019

*Omitted for brevity*

## CONTENTS

|  |             |
|--|-------------|
| <b>List of Figures . . . . .</b>                             | <b>viii</b> |
| <b>Preface . . . . .</b>                                     | <b>xiv</b>  |
| <b>Curriculum Vitae . . . . .</b>                            | <b>xv</b>   |
| <b>1 Introduction . . . . .</b>                              | <b>1</b>    |
| <b>2 Chemical Rate Constants . . . . .</b>                   | <b>2</b>    |
| 2.1 Average Dipole Orientation Theory (ADO) . . . . .        | 3           |
| 2.1.1 Radially Symmetric Adiabatic Capture Theory . . . . .  | 3           |
| 2.1.2 Ion-Dipole Interaction . . . . .                       | 6           |
| <b>3 The Cryogenic Buffer Gas Beam (CBGB) . . . . .</b>      | <b>12</b>   |
| 3.1 Design . . . . .   | 14          |
| 3.1.1 Heat Load and Thermal Conductivity . . . . .           | 17          |
| 3.1.2 Gas Fill Lines . . . . .                               | 20          |
| 3.2 Beam Density and Extraction . . . . .                    | 24          |
| 3.2.1 Direct Beam Measurement and Parameterization . . . . . | 28          |
| 3.2.2 Beam Density at Ion Trap . . . . .                     | 33          |
| 3.3 Beam Velocity . . . . .                                  | 33          |
| 3.4 Beam Shuttering . . . . .                                | 36          |
| <b>4 Trapping and Cooling Ions . . . . .</b>                 | <b>40</b>   |
| 4.1 Ion Trapping . . . . .                                   | 40          |

|       |   |    |
|-------|---|----|
| 4.2   | Vacuum Requirements . . . . .   | 43 |
| 4.3   | ${}^9\text{Be}^+$ Laser Cooling . . . . .   | 45 |
| 4.4   | Imaging System . . . . .  | 48 |
| 4.5   | Determining Excited State Population . . . . .  | 50 |
| 4.6   | Time of Flight Mass Spectrometer (TOF-MS) . . . . .   | 54 |
| 4.6.1 | TOF Signal Integration . . . . .  | 56 |
| 4.7   | Dual Species Loading . . . . .  | 57 |
| 5     | $\text{Be}^+({}^2\text{S}_{1/2}/{}^2\text{P}_{3/2}) + \text{H}_2\text{O}$ . . . . .   | 60 |
| 5.1   | Optical Control of Reactions between Water and Laser-Cooled $\text{Be}^+$ Ions . . . . .  | 60 |
| 5.1.1 | Prologue . . . . .  | 60 |
| 5.1.2 | Introduction . . . . .  | 60 |
| 5.1.3 | Experimental . . . . .  | 61 |
| 5.1.4 | Results and Discussion . . . . .  | 63 |
| 5.1.5 | Conclusion . . . . .  | 65 |
| 6     | $\text{Be}^+ + \text{H}_2\text{O}/\text{HOD}/\text{D}_2\text{O}$ . . . . .  | 69 |
| 6.1   | Isotope-selective chemistry in the $\text{Be}^+({}^2\text{S}_{1/2}) + \text{HOD} \rightarrow \text{BeOD}^+/\text{BeOH}^+ + \text{H/D}$ reaction . . . . . | 69 |
| 6.2   | Introduction . . . . .  | 69 |
| 6.3   | Experimental . . . . .  | 71 |
| 6.4   | Results and Discussion . . . . .  | 72 |
| 6.5   | Conclusion . . . . .  | 75 |
| 7     | Low Temperature $\text{C}^+ + \text{H}_2\text{O}$ . . . . .   | 76 |
| 7.1   | Formyl Isomer Production . . . . .  | 76 |

|       |   |    |
|-------|---|----|
| 7.2   | O <sub>2</sub> Titration . . . . .                                | 79 |
| 7.3   | <sup>15</sup> N <sub>2</sub> Titration . . . . .                  | 80 |
| 7.3.1 | Branching Ratio Determination . . . . .                           | 82 |
| 8     | Conclusion and Future Outlook . . . . .                           | 85 |
| A     | Pressure Calibration . . . . .                                    | 86 |
| B     | Chemical Rate Equations . . . . .                                 | 89 |
| B.1   | Be <sup>+</sup> + H <sub>2</sub> O + H <sub>2</sub> . . . . .     | 89 |
| B.2   | Be <sup>+</sup> + H <sub>2</sub> O/HOD/D <sub>2</sub> O . . . . . | 90 |
| B.3   | C <sup>+</sup> + H <sub>2</sub> O . . . . .                       | 90 |
|       | References . . . . .  | 92 |

## LIST OF FIGURES

|  |    |
|--|----|
| 2.1 Numerical solutions for eq. (2.16) as a function of maximum angle $K$ . In the limit of large $K$ , we find an intuitive solution where $\theta_1$ averages towards 0. . . . .   | 8  |
| 2.2 Numerical solution to eq. (2.17) as a function of the ratio of rotational energy and the monopole-dipole term. The low ratio behavior is not immediately obvious, but the greater the ratio between the rotational energy and monopole-dipole term, the more $\theta_2$ tends towards $\pi/2$ . . . . .  | 9  |
| 2.3 Dipole locking constant $C$ parameterized by the dipole moment $\mu_D$ and polarizability $\alpha$ .[45] . . . . .   | 11 |
|  |    |
| 3.1 Schematic of target species entrainment within a buffer gas beam cell. With high densities of buffer gas particles, an introduced target species undergoes collisions with the buffer gas such that it cools. At high enough densities, flow dynamics cause the target species to become entrained in the buffer gas flow and are carried out of the cell with greater efficiency. . . . . | 13 |
| 3.2 Cross sectional view of CBGB in solidworks. Components include copper sheath for PTR, aluminum radiation shield with chevron baffles, copper shield and experimental cell, and skimmer mounted in stem chamber. The baffles allow for gas to flow into the cold region of the beam apparatus, while preventing 300 K black body radiation from hitting the inner shield and cell. . . . .  | 16 |
| 3.3 Cross sectional view of CBGB with side walls removed from the outer vacuum chamber, 40 K aluminum radiation shield, and inner 4 K cryopumping shield exposing the inner experimental cell. A skimmer is mounted in the stem region. . . . .  | 17 |
| 3.4 The water fill line, sealed by an ultratorr fitting and heated by nichrome wire. A shut off valve and vernier valve are used to regulate the flow of water into the buffer gas cell. . . . .   | 22 |

|  |    |
|--|----|
| 3.5 A kapton film serves as the back wall of the buffer gas cell with a hole punctured for the insertion of the water fill line. The kapton surface seals the back of the cell for a stronger forward beam, while limiting the heat load from a room temperature fill line, and resisting ice formation allowing for continuous and consistent operation with water for over 10 hours. . . . .   | 23 |
| 3.6 Theoretically derived buffer gas beam properties of interest given the physical dimensions of our cell in particular: $d_{aperture} = 9$ mm. A) $\gamma$ extraction ratio, dotted red line indicates $\gamma = 1$ where hydrodynamic entrainment begins. B) Number density of buffer gas species within the experimental cell, given an enclosed back wall. The density of target species introduced should stay under 1% of the buffer gas density for other properties to hold. C) Number of collisions a target species particle would expect before extraction out of the cell, the dotted red line indicates 100 collisions before extraction, when rotational degrees of freedom are characteristically thermalized. . . . . | 28 |
| 3.7 Fitted linear behavior of H <sub>2</sub> O entrained in a Ne buffer gas beam 30 cm from cell aperture. The onset of hydrodynamic entrainment seems to occur around 20 SCCM up through 60/65 SCCM where the H <sub>2</sub> O extracted into the beam has a clear linear form of $(9.2 \times 10^8 \text{ cm}^{-3}/\text{SCCM})f - 2 \times 10^{10} \text{ cm}^{-3}$ . . . . .   | 29 |
| 3.8 Projected beam densities with a Ne flow rate of 30 SCCM with various distances of interest within the chamber. Beam densities shown are without throttling of the H <sub>2</sub> O flow valve. . . . .   | 31 |
| 3.9 Projected beam densities at the trap center over various nominal Ne flow rates and smallest skimmer aperture size. Beam densities shown are without throttling of the H <sub>2</sub> O flow valve. . . . .   | 32 |
| 3.10 Angled longitudinal scan of Yb fluorescence collected by PMT at $\approx 24$ cm from cell aperture. A fit of all isotopic peaks yields mggm . . . . .   | 36 |
| 3.11 Ratios of water and neon from the beam when the Uniblitz shutter is opened and closed. Detection is done via RGA placed 30 cm from the cell aperture. . . . .   | 38 |

|   |    |
|---|----|
| 3.12 Fluorescence decays of loaded Be <sup>+</sup> ions exposed to a cold water beam with an inline shutter either opened, in green ( $\tau = 7.23 \times 10^{-3}$ s) or closed, in blue ( $\tau = 6.37 \times 10^{-2}$ s) . . . . .  | 38 |
| 3.13 Fluorescence decays of loaded Be <sup>+</sup> ions exposed to a cold water beam with an inline shutter opened, in green ( $\tau = 5.37 \times 10^{-2}$ s) or closed, in red ( $\tau = 7.59 \times 10^{-3}$ s) . . . . .  | 39 |
| 4.1 The ion trap inside of the experimental vacuum chamber. An Einzel lens and imaging objective are seen on the vertical axis. . . . .   | 42 |
| 4.2 Stability diagram of the experimental ion trap with parameters defined in table 4.1. The trap is set up to be stable for ions of interest, including high mass reaction products, from Be <sup>+</sup> , and C <sup>+</sup> at $m/z = 9, 12$ to CO <sub>2</sub> H <sup>+</sup> at $m/z = 45$ . . . . .  | 43 |
| 4.3 Differential pumping region in between the stem and ion trap chambers with gate valves on either end. Blank copper CF gaskets with apertures of 4 mm and 10 mm are placed towards the stem and ion chamber respectively to limit conductance of background gasses while allowing the cryogenic beam through. An Agilent Twistorr 84 FS turbo pump keeps the region at pressures around $10^{-10}$ Torr and a leak valve allows for controlled introduction of secondary gasses. . . . .                                 | 45 |
| 4.4 Electronic structure of <sup>9</sup> Be <sup>+</sup> , laser cooling is done with 313 nm light. . . . .   | 47 |
| 4.5 AOM's running at 400 MHz are used to tune the initially blue detuned primary beam on resonance with the <sup>2</sup> S <sub>1/2</sub> to <sup>2</sup> P <sub>3/2</sub> transition. A double passed AOM tunes the primary beam to the <sup>2</sup> S <sub>3/2</sub> to <sup>2</sup> P <sub>3/2</sub> transition to re-pump any <sup>2</sup> P <sub>3/2</sub> —> <sup>2</sup> S <sub>3/2</sub> decays. A third AOM creates a first order beam 200 MHz red to aid the capture of hot ablated Be <sup>+</sup> ions. . . . . | 47 |
| 4.6 The iXon3 camera is mounted onto a 3 axis translation stage as well as the enclosed imaging pathway. The imaging tubes include the Sill objective lens at the end, inserted into the reentrant flange, an angled mirror, and a 313 nm bandpass filter placed at the camera input. . . . .   | 49 |

|      |   |    |
|------|---|----|
| 4.7  | Laser cooled Coulomb crystal of $\text{Be}^+$ ions in the LQT imaged with the reentrant imaging system. . . . .   | 50 |
| 4.8  | A set of ion images taken at various 313 nm powers run thorough a maximum filter algorithm that identifies local maxima, representing individual ions (circled in red). gaps in the ion chain are due to reactions with background $\text{H}_2$ producing $\text{BeH}^+$ , which occupy crystal sites without fluorescing. . . . .  | 52 |
| 4.9  | Individual ions identified from images in figure 4.8. Integrated pixel values with subtracted background counts shown for each image, a set's averaged value is shown in brackets. . . . .  | 53 |
| 4.10 | P-state fraction curve fitted to incident laser power at a fixed detuning of $\delta = \Gamma/2$ . Total fluorescence value is normalized by fitted efficiency parameter $a$ to yield $\rho_{pp}$ . . . . .   | 54 |
| 4.11 | text . . . . .  | 55 |
| 4.12 | Image of the single laser, dual ablation set up. The 1064 nm YAG pulse is split into two paths, and recombined such that they proceed through the same focusing element into the chamber to hit two different targets. . . . .  | 58 |
| 4.13 | TOF trace of simultaneous $\text{Be}^+$ and $\text{C}^+$ ablation loading averaged over 10 shots. A soft A-ramp is applied after loading, ejecting any unintentionally loaded $\text{Cn}^+$ clusters. The $\text{C}^+$ peak is narrowed from sympathetic cooling with the laser cooled $\text{Be}^+$ ions. . . . .  | 59 |
| 5.1  | (A) Typical fluorescence decay measurement. The inset images are a subset of the original ion fluorescence images recorded by the camera. The red curve is an exponential fit (with a free offset) to the data, which gives the total reaction rate. (B) Total reaction rate coefficient as a function of $\text{Be}^+$ ( ${}^2\text{P}_{3/2}$ ) state population can be used to separate the contributions from the ground and excited states of $\text{Be}^+$ . . . . . | 63 |
| 5.2  | The temporal evolution of $\text{Be}^+$ in the trap as a function of reaction time as well as the solutions of differential equations fitted to the kinetics data with $P_{\text{P}} = 26\%$ . . . . .  | 66 |

|   |    |
|---|----|
| 5.3 TOF signal (averaged over 10 trials) at reaction time $t = 0$ and 70 s with (A) $P_P = 7\%$ (A) and (B) $P_P = 26\%$ . A clear $m/z = 19$ peak emerges when more $\text{Be}^+$ ions are excited to ${}^2\text{P}_{3/2}$ state. The $\text{BeOH}^+ / \text{H}_3\text{O}^+$ ratio for this case ( $P_P = 26\%$ ) is measured to be $\eta(0.26) = 0.039 \pm 0.006$ by integrating both peaks in B when $t = 70$ s. . . . .   | 67 |
| 5.4 Energetics of both the ground- and excited-state reaction pathways for the $\text{Be}^+ + \text{H}_2\text{O}$ reaction. Whereas reaction 5.1 proceeds on a single adiabatic PES, the reactions involving excited $\text{Be}^+$ depend on nonadiabatic transitions between different PESs (yellow circles). The submerged well on the ground-state reaction pathway prevents 46% of the trajectories to reflect back to the entrance channel. (Taken from [53]) . . . . .  | 68 |
| 6.2 (left) Averaged (8 traces) RGA analog scan showing peaks at each isotopologue $m/z$ . Points around the peak of each isotopologue were averaged for a more accurate partial pressure. (right) The branching ratio $\eta$ of the reaction $\text{Be}^+ + \text{HOD}$ into $\text{BeOD}^+ + \text{H}$ (with a $\text{Be}^+$ P-state fraction of $P_P \approx 2\%$ ) as a function of initial H fraction in an HOD, $\text{H}_2\text{O}$ , $\text{D}_2\text{O}$ mixture. Shared fitting the branching ratio $\eta$ with a constant value fit is shown with a weighted average of $\eta = 0.58 \pm 0.14$ . . . . .  | 72 |
| 6.1 (A) A typical TOF signal (5 sample average) at reaction time $t = 0$ s and 60 s with $P_P \approx 2\%$ . (B) The temporal evolution of $\text{Be}^+$ , $\text{BeOH}^+$ , and $\text{BeOD}^+$ in the trap as a function of reaction time, as well as the solutions of differential equations fitted to the kinetics data with $P_P \approx 2\%$ . (C) The RGA signal (8 traces average) gives relative initial $\text{H}_2\text{O}$ , HOD, $\text{D}_2\text{O}$ sample ratio, which is $\rho_1 : \rho_2 : \rho_3 = (1.00 \pm 0.02) : (2.45 \pm 0.05) : (1.58 \pm 0.02)$ . (D) The product fraction for $\text{BeOD}^+$ production ( $\eta$ ) of reactions (6.8 and 6.9) as a function of $\text{Be}^+({}^2\text{P}_{3/2})$ state population. The S-state branching ratio is found to be $\eta_s = 0.56 \pm 0.03$ , in agreement with the following calculated combined value with different initial H fractions. . . . . | 73 |
| 7.1 text . . . . .  | 79 |

|     |  |    |
|-----|--|----|
| 7.2 | text   | 80 |
| 7.3 | TOF trace of reaction products of $\text{Be}^+$ and $\text{C}^+$ after exposure to both water from the CBGB beam, and CO (10 s) before titration with $^{15}\text{N}_2$ (10 s). There is a distinct lack of $\text{N}_2\text{H}^+$ , indicating full conversion of $\text{HOC}^+ \longrightarrow \text{HCO}^+$ .   | 82 |
| 7.4 | $^{15}\text{N}_2$ introduced into the ion chamber after trapped $\text{Be}^+$ and $\text{C}^+$ are exposed to water from the CBGB for set times.   | 84 |
| A.1 | Fitted curves for $\text{H}_2$ and $\text{H}_2\text{O}$ detection between the ion gauge and RGA. The reported pressure between the ion gauge and RGA is nearly identical for $\text{H}_2\text{O}$ with a slope of 1.1, but noticeably different for $\text{H}_2$ with a slope of 0.59.   | 87 |
| A.2 | (A) A typical fluorescence decay measurement of $\text{Be}^+ + \text{H}_2$ . The inset images are a subset of the original ion fluorescence images recorded by the camera. The red curve is an exponential fit (with a free offset) to the data, which gives the total reaction rate. (B) A fit of $\text{Be}^+ + \text{H}_2$ fluorescence decay at various P state excitation fractions. A statistical rate coefficient for full excitation of $(1.2 \pm 0.3_{\text{state}}) \times 10^{-9}$ $\text{cm}^3/\text{s}$ is in agreement with existing literature. | 88 |

## PREFACE

## CURRICULUM VITAE

- 2009 – 2013                    B.S. in Physics, University of Maryland (UMD), College Park, Maryland
- 2013 – Present                Ph.D. student in Physics, University of California, Los Angeles (UCLA).

# **CHAPTER 1**

## **Introduction**

This thesis chronicles the experimental work done to realize an apparatus for cold ion-molecule chemistry of species of astrochemical interest, and attempts to understand chemistry in general along the way.

## CHAPTER 2

### Chemical Rate Constants

When describing the rates of chemical reactions, it is usually described by the order of reaction. Usually the order of reaction is dependent on the sum of the order the constituents contribute to the reaction. For example, if we have a reaction of:



The appearance of products  $[C]$  and  $[D]$  is directly equivalent to the disappearance of  $[A]$  and  $[B]$ . The rate constant is then defined as:

$$k = \frac{\Gamma}{[A]^m[B]^n}$$

Where  $k$  is the rate constant, and  $\Gamma$  is the reaction rate in time. The order of the reaction is defined as the sum of the constituent power dependencies  $m + n$ . For gas phase reactions, the dependencies are usually of order unity, as it is unlikely to have multiple collisions during a single reaction lifetime. For bi-molecular reactions that we are exploring, we would expect the rate to be a second order rate, which gives a solution of:

$$\frac{[A]}{[B]} = \frac{[A]_0}{[B]_0} e^{([A]_0 - [B]_0)kt}$$

Where the rate constant  $k = (([A]_0 - [B]_0)\tau)^{-1}$ . In reality, we are only trapping a few ions in the trap while flooding the chamber with neutral reactants from either the beam or a leak valve. In either case, the concentration of one reactant is held effectively fixed, while the

other is depleted. From here, we yield the pseudo-first-order reaction rate constant, which takes a second order reaction and simplifies it to a first order rate equation.

$$\frac{d[A]}{dt} = -k[B][A]$$

$$[A] = [A]_0 e^{-k[B]t} \quad (2.1)$$

Where  $[A]$  and  $[B]$  are the concentrations of the scarce and flooded reactants respectively. We can readily identify the rate constant  $k = ([B]\tau)^{-1}$ , with dimensions  $\text{cm}^3/\text{s}$ . The reactions discussed in this thesis are exclusively of the pseudo-first-order.

## 2.1 Average Dipole Orientation Theory (ADO)

Under the understanding that the reactions of interest follow a pseudo-first order model, we are only considering single collisions between the two reactants. To figure out the characteristic rate of the rate constant  $k$ , we want to model the interaction between the reactants, whether it be neutral-neutral, to ion-dipole. To do this, we consider adiabatic capture theory, a study of the long range potentials between particles to yield a reaction rate constant. A caveat is that the adiabatic capture theory is long ranged, only finding the rate at which a collision will occur, not necessarily when a reaction will happen. The probability of a reaction occurring requires modeling of short range interactions within the reaction complex.

### 2.1.1 Radially Symmetric Adiabatic Capture Theory

A general method of calculating the rate constant of two particles with a given potential, finding the collisional cross section, which is then averaged over a velocity distribution to find the rate constant.<sup>[56]</sup> Starting with the attractive potential, we find that it is a summation of interactions with coefficients  $C_n$ , where  $n$  is the order of the interaction potential on the

intermolecular distance  $r$ .

$$V(r) = \sum_n -\frac{C_n}{r^n} \quad (2.2)$$

We may write the effective potential in the center of mass frame as:

$$V_{eff} = \frac{l^2}{2\mu_R r^2} - \sum_n \frac{C_n}{r^n} \quad (2.3)$$

Where  $\mu_R$  is the reduced mass of the two particles. If  $n > 2$ , we can derive the capture cross-section and rate constant as follows. First, we find the position  $r_0$  corresponding to the maximum of the effective potential, which is the maximum of the centrifugal barrier.

$$\begin{aligned} \frac{\partial V_{eff}(r_0)}{\partial r} &= 0 \\ \therefore r_0 &= \left( \frac{n\mu_R C_n}{l^2} \right)^{1/n-2} \end{aligned}$$

Substituting  $r_0$  back into equation 2.3, we find the maximal value of the effective potential:

$$V_{eff}(r_0) = \left( \frac{l^2}{\mu_R} \right)^{\frac{n}{n-2}} \frac{n-2}{2n} (nC_n)^{-\frac{2}{n-2}} \quad (2.4)$$

This then defines the energy necessary for a collision, for if  $E_{col}$  exceeds  $V_{eff}(r_0)$ , the reactants will be able to surmount the centrifugal barrier and collide. Thus, we may define the maximum value for the angular momentum  $l$  and the impact parameter  $b$ .

$$\begin{aligned} l_{max} &= (\mu_R n)^{1/2} (C_n)^{1/n} \left( \frac{2E_{col}}{n-2} \right)^{\frac{n-2}{2n}} \\ b_{max} &= \frac{l_{max}}{\mu_R v} \end{aligned}$$

We can then define a collision cross section dependent on the collision energy:

$$\begin{aligned}\sigma(E_{col}) &= \pi b_{max}^2 \\ &= \frac{\pi}{2} n \left( \frac{2}{n-2} \right)^{\frac{n-2}{2}} \left( \frac{C_n}{E_{col}} \right)^{\frac{2}{n}}\end{aligned}$$

Integrating the collision cross section with a Maxwell Boltzmann distribution yields a generalized rate constant as a function of temperature and  $n$ .

$$k(T) = \int_0^\infty v f(v) \sigma(v) dv \quad (2.5)$$

$$= \sqrt{\frac{2\pi}{\mu_R}} n \left( \frac{2}{n-2} \right)^{\frac{n-2}{2}} C_n^{2/n} (k_B T)^{\frac{n-4}{2n}} \Gamma \left( 2 - \frac{2}{n} \right) \quad (2.6)$$

For instance, we are interested in the dipole-dipole interactions of order  $n = 3$ , as well as the ion-neutral interactions of order  $n = 4$ . For the dipole-dipole interaction:

$$\begin{aligned}C_3 &= \mu_{D,1} \mu_{D,2} \cos(\theta) \\ k(T) &= 4 \sqrt{\frac{\pi}{3\mu_R}} \Gamma \left( \frac{1}{3} \right) (\mu_{D,1} \mu_{D,2} \cos(\theta))^{2/3} (k_B T)^{-1/6}\end{aligned} \quad (2.7)$$

Where  $\mu_{D,i}$  is the  $i$ th particle's dipole moment, and  $\theta$  is the angle between the two dipoles. Similar treatment for  $n = 4$  yields:

$$\begin{aligned}C_4 &= \frac{\alpha q^2}{2} \\ k(T) &= 2\pi q \sqrt{\frac{\alpha}{\mu_R}}\end{aligned} \quad (2.8)$$

Where  $\alpha$  is the polarizability of the neutral reactant, and  $q$  is the monopole charge. The corresponding  $k$  value in eq. (2.8) is known as the Langevin rate constant, which is famously temperature independent.

### 2.1.2 Ion-Dipole Interaction

Unlike the Langevin interaction, the ion-dipole term has an angular term defined with respect to the inter-molecular axis. A few approximations are taken to give an average dipole orientation theory pioneered and expanded on by Su and Bowers.[45, 46] This can also be extrapolated to include quadrupole interactions.[47]

The Langevin term of the ion and ion-induced dipole interaction is as follows:

$$V_L(r) = -\frac{\alpha q^2}{2r^4} \quad (2.9)$$

In the case of the ion-dipole interaction:

$$V_D(r, \theta) = -\frac{q\mu_D}{r^2} \cos(\theta) \quad (2.10)$$

The method outlined in section 2.1.1 finds the rate constant by dealing with a two body problem only needing to consider the  $r$  degree of freedom. The inclusion of the  $\theta$  term complicates this, but to first order, we can parameterize  $\theta$  as a function of  $r$ . What we want to achieve is to write down the potential as such:

$$\begin{aligned} V(r) &= -\frac{\alpha q^2}{2r^4} - \frac{q\mu_D}{r^2} \cos(\bar{\theta}(r)) \\ \bar{\theta} &= \frac{\int \theta P(\theta) d\theta}{\int P(\theta) d\theta} \end{aligned} \quad (2.11)$$

Where  $P(\theta)$  is the probability of finding the dipole oriented with angle  $\theta$ . To determine the average orientation of the dipole, we consider the following cases:

1.  $P(\theta)$  is inversely proportional to the angular velocity:

$$P(\theta) \propto 1/\dot{\theta}$$

2. An orientation has a probability weighted by the circumference of an angle:

$$C = 2\pi l \sin(\theta)$$

$$P(\theta) \propto \sin(\theta)$$

The angular probability is proportional to both effects:

$$P(\theta) \propto \frac{\sin(\theta)}{\dot{\theta}} \quad (2.12)$$

We can relate the angular velocity to the angular kinetic energy and the total energy in the system:

$$\begin{aligned} KE_{rot} &= \frac{1}{2} I \dot{\theta}^2 \\ E_{tot} &= KE_{rot} + V_D \end{aligned} \quad (2.13)$$

Redefining equation 2.12 with equation 2.13, we find:

$$P(\theta) \propto \frac{\sin(\theta)}{\sqrt{E_{rot} - V_D}} \quad (2.14)$$

Combining equations eqs. (2.14) and (2.11) yields a total averaged dipole orientation.

$$\bar{\theta} = \frac{\int \frac{\theta \sin(\theta) d\theta}{\sqrt{E_{rot} + q\mu_D/r^2 \cos(\theta)}}}{\int \frac{\sin(\theta) d\theta}{\sqrt{E_{rot} + q\mu_D/r^2 \cos(\theta)}}} \quad (2.15)$$

From here, two situations arise:

1.  $E_{rot} = E_1 < \frac{q\mu_D}{r^2}$ : There is not enough rotational energy to overcome the dipole locking. The solution is oscillatory, but  $\theta$  has an  $r$  dependent bound. We let the maximal capture angle that rotational energy  $E_1$  allows be defined as  $K$ .

$$E_1 = -\frac{q\mu_D}{r^2} \cos(K)$$

When substituted into equation 2.15, we find:

$$\bar{\theta}_1 = \frac{\int_0^K \frac{\theta \sin(\theta) d\theta}{\sqrt{\cos(\theta) - \cos(K)}}}{\int_0^K \frac{\sin(\theta) d\theta}{\sqrt{\cos(\theta) - \cos(K)}}} \quad (2.16)$$

After some math (something something integration by infinite series) and get a result of:

$$\bar{\theta}_1 = \frac{2\sqrt{2}A}{\sqrt{1 - \cos(K)}}$$

where  $A \equiv \int_0^{\pi/2} \frac{a^2 \cos(\phi)^2 d\phi}{\sqrt{q - a^2 \sin(\phi)^2}}$

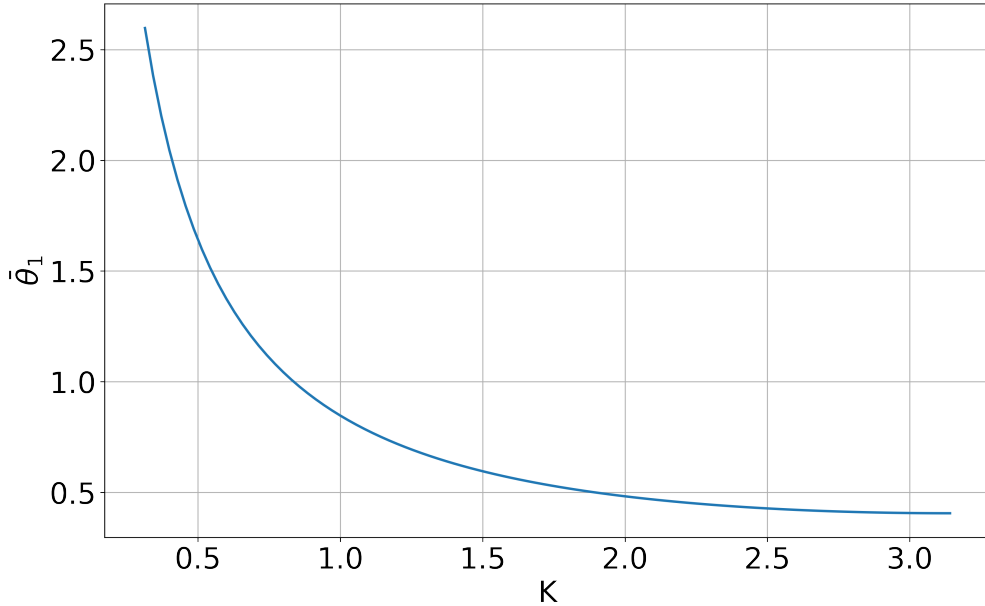


Figure 2.1: Numerical solutions for eq. (2.16) as a function of maximum angle  $K$ . In the limit of large  $K$ , we find an intuitive solution where  $\theta_1$  averages towards 0.

2.  $E_{rot} = E_1 > \frac{q\mu_D}{r^2}$ : The rotational energy is enough to overcome the dipole locking and  $\theta$  can swing around in a complete circle

$$\bar{\theta}_2 = \frac{\int_0^\pi \frac{\theta \sin(\theta) d\theta}{\sqrt{E_2 + q\mu_D/r^2 \cos(\theta)}}}{\int_0^\pi \frac{\sin(\theta) d\theta}{\sqrt{E_2 + q\mu_D/r^2 \cos(\theta)}}} \quad (2.17)$$

We no longer have bounds on the angles the dipole is allowed over, but the behavior is still dependent on the strength of the internal energy and dipole force.

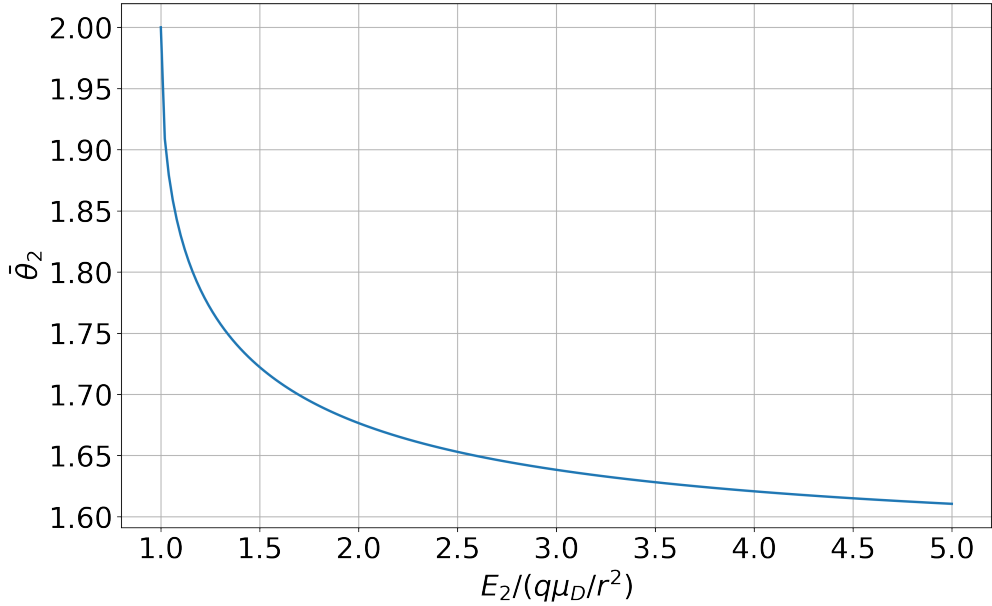


Figure 2.2: Numerical solution to eq. (2.17) as a function of the ratio of rotational energy and the monopole-dipole term. The low ratio behavior is not immediately obvious, but the greater the ratio between the rotational energy and monopole-dipole term, the more  $\theta_2$  tends towards  $\pi/2$ .

Let's say we have the forms for  $\bar{\theta}_1$  and  $\bar{\theta}_2$ , we want to write down the full form of  $\theta$ . We can combine the two weighted by the probability of each as a function of internal energy.

$$\bar{\theta}(r) = \bar{\theta}_1(r)F_1 + \bar{\theta}_2(r)F_2 \quad (2.18)$$

Where the weightings  $F_i$  are found via:

$$P(\epsilon)d\epsilon = \frac{1}{k_B T} e^{-\frac{\epsilon}{k_B T}} d\epsilon$$

For diatomics, the energies of rotational states is defined as:

$$\epsilon = B_e J(J+1)$$

Where the rotational constant is  $B_e = \frac{\hbar^2}{2\mu R^2}$ ,  $\mu$  is the reduced mass of the molecule, and  $R$  is the inter-nuclear separation. We can then use equation 2.5 and get a cross section and rate constant. The form is similar to that of just a Langevin term, but now with a dipole interaction term added onto it.

$$k_{ADO} = \frac{2\pi e}{\sqrt{\mu}} \left( \sqrt{\alpha} + C\mu_D \sqrt{\frac{2}{\pi k_B T}} \right) \quad (2.19)$$

Where  $C$  is the dipole locking constant. All of the terms aside from  $C$  come from the integration over a Boltzmann distribution in  $v$ .  $C$  itself can be numerically solved by iteratively integrating over combinations of  $\mu_D$  and  $\alpha$ .[45][48]

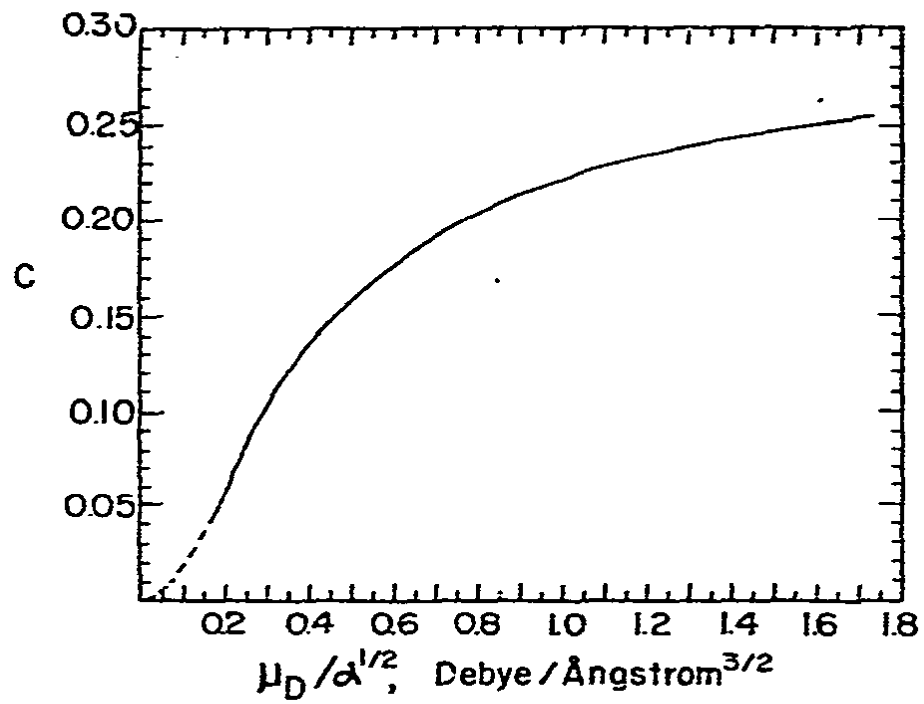


Figure 2.3: Dipole locking constant  $C$  parameterized by the dipole moment  $\mu_D$  and polarizability  $\alpha$ .[45]

## CHAPTER 3

### The Cryogenic Buffer Gas Beam (CBGB)

To reach reaction temperatures around 10K from a beam of molecules with trapped ions, a cryogenic buffer gas beam (CBGB) of neon with entrained water is employed. Numerous other methods of creating cold beams of molecules exist, from Zeeman decelerators [30], to Stark decelerators. CBGB's in particular have the benefit of being species agnostic, where the resultant beam properties are not dependent on the target species at hand, rather, the buffer gas species.

By holding a cell filled with a noble gas above its vapor pressure, a volume of gas can be held at cryogenic temperatures. Other species of molecules or atoms may be introduced into the buffer gas cell via ablation, fill line, etc. The target species particles are then sympathetically cooled via collisions with the cold buffer gas. An aperture at one end of the cell allows for the extraction of the buffer gas and entrained target species into a ballistic beam. Holding the buffer gas cell temperature to above 17 K for neon, and 4 K for helium, in high vacuum allows us to accumulate an appreciable stagnation number density within the cell to produce a beam of entrained target particles.

The properties of interest are a function of the flow regime of the beam, which is determined by the choice of gas, its flow rate, and the dimensions of the cell it is held in. It's convenient to use the Reynolds number at the aperture to characterize the flow regime, which can be written as:

Add  
ci-  
ta-  
tions  
for  
de-  
cel-  
er-  
a-  
tors



Figure 3.1: Schematic of target species entrainment within a buffer gas beam cell. With high densities of buffer gas particles, an introduced target species undergoes collisions with the buffer gas such that it cools. At high enough densities, flow dynamics cause the target species to become entrained in the buffer gas flow and are carried out of the cell with greater efficiency.

$$\begin{aligned} Re &\approx \frac{2d_{aperture}}{\lambda} \\ &\approx \frac{8\sqrt{2}\dot{N}\sigma}{d_{aperture}\bar{v}} \end{aligned} \quad (3.1)$$

Where  $d_{aperture}$  is the diameter of the aperture and  $\lambda$  is the mean free path of the buffer gas particles.[21] When the Reynolds number is low,  $Re < 1$ , we find that there are on average  $> 1$  collisions at the aperture, meaning the particles escape with little to no interactions with other particles and is called the effusive regime. At high Reynolds numbers,  $Re > 100$ , in the supersonic regime, there are many collisions and forward velocity boosting as well as internal velocity distribution narrowing occurs. In between, we find the intermediate regime, where we observe the onset of hydrodynamic entrainment of target species with mild forward velocity boosting. In all cases, the gasses inside the cell at thermal equilibrium follow the Maxwell-Boltzmann distribution.

$$f(v) = \left(\frac{m}{2\pi kT}\right)^{3/2} 4\pi v^2 e^{-\frac{mv^2}{2kT}} \quad (3.2)$$

Where the mean velocity is:

$$\bar{v} = \sqrt{\frac{8k_B T}{\pi m}} \quad (3.3)$$

The goal for our beam is three fold, to produce a **slow, dense, localized** beam of our target species that can make it down into the ion trap region. The velocity and density of the target species are both related to the flow regime of the buffer gas, and to reach our goal, it's ideal for us to aim for a beam that operates within the intermediate regime, between effusive and supersonic. Producing a localized beam ensures that we are introducing the minimal unwanted gas load into the ion trap chamber, and that we may quickly and reliably shutter the beam to start and stop the chemical reactions. In the following sections, we will discuss the design of the apparatus and characterization of the beam density, extraction, forward velocity, and shuttering.

### 3.1 Design

The CBGB apparatus design has various stages, a room temperature 300 K outer aluminum vacuum chamber, onto which a Pulse Tube Refrigerator (PTR) is mounted, an aluminum radiation shield mounted to the 40 K PTR cooling stage, and an inner copper cryopumping shield and experimental cell connected to the 4 K PTR cooling stage. Connected to the vertical vacuum chamber, a "stem" region protrudes out from the beam side as seen in figures figs. 3.2 and 3.3 where a large Agilent Varian-V 551 turbo pump evacuates the entire volume. The beam comes out of the experimental cell and shield, through a set of apertures, into the stem region where skimmers and shutters are mounted to manipulate the beam.

A Cryomech PT415 PTR with a remote head option was attached to the top plate of the vacuum chamber with a large bellows mount to isolate the chamber from the mechanical vibrations caused by the PTR motor head. The chamber was pumped down to normal operating pressures, where then 4 retaining screws were tightened to just above the bellows' compressed height. This maintains mechanical decoupling between the outer vacuum

chamber and the PTR while running.

We want to minimize the mechanically coupling onto the PTR due to the fragility of the pulse tube walls; small amounts of force applied onto a mechanically connected component would risk torquing the walls to break. Thus, all components inside the CBGB are mechanically connected to the top plate of the vacuum chamber via 8-32 stainless steel (SS316) threaded rods. Thermal connections are made with copper braids welded onto L-shaped brackets that mount between platforms secured to the PTR cooling stages, and the shields.

Not only are all the inner shields connected to the top plate, but so are the feedthroughs including gas fill lines. This ensures that any and all connections made into the CBGB are not disturbed when opening the outer vacuum chamber to expose the inner components.

The design of the shields themselves is informed by the choice of buffer gas species. Commonly used buffer gas species are helium and neon, while helium provides a slower beam, it is more technically challenging to implement. The main technical difference comes from the cryopumping requirements; where neon only needs surfaces to be held at 17 K to continually cryopump, helium requires (coconut) activated charcoal held at 4 K or lower. Aside from the difficulty of getting surfaces to 4 K these volumes of charcoal can become saturated and require purging, limiting one's operating time (few hours). On the other hand, neon ice formed on the 17 K surface will act as a cryopump for more neon gas, allowing for many hours of continuous operation with no appreciable build up of background gas. Our experiment uses neon as a buffer gas for its technical simplicity, the lower achievable temperature with the helium does not yield dramatic gains in the final reaction temperature.

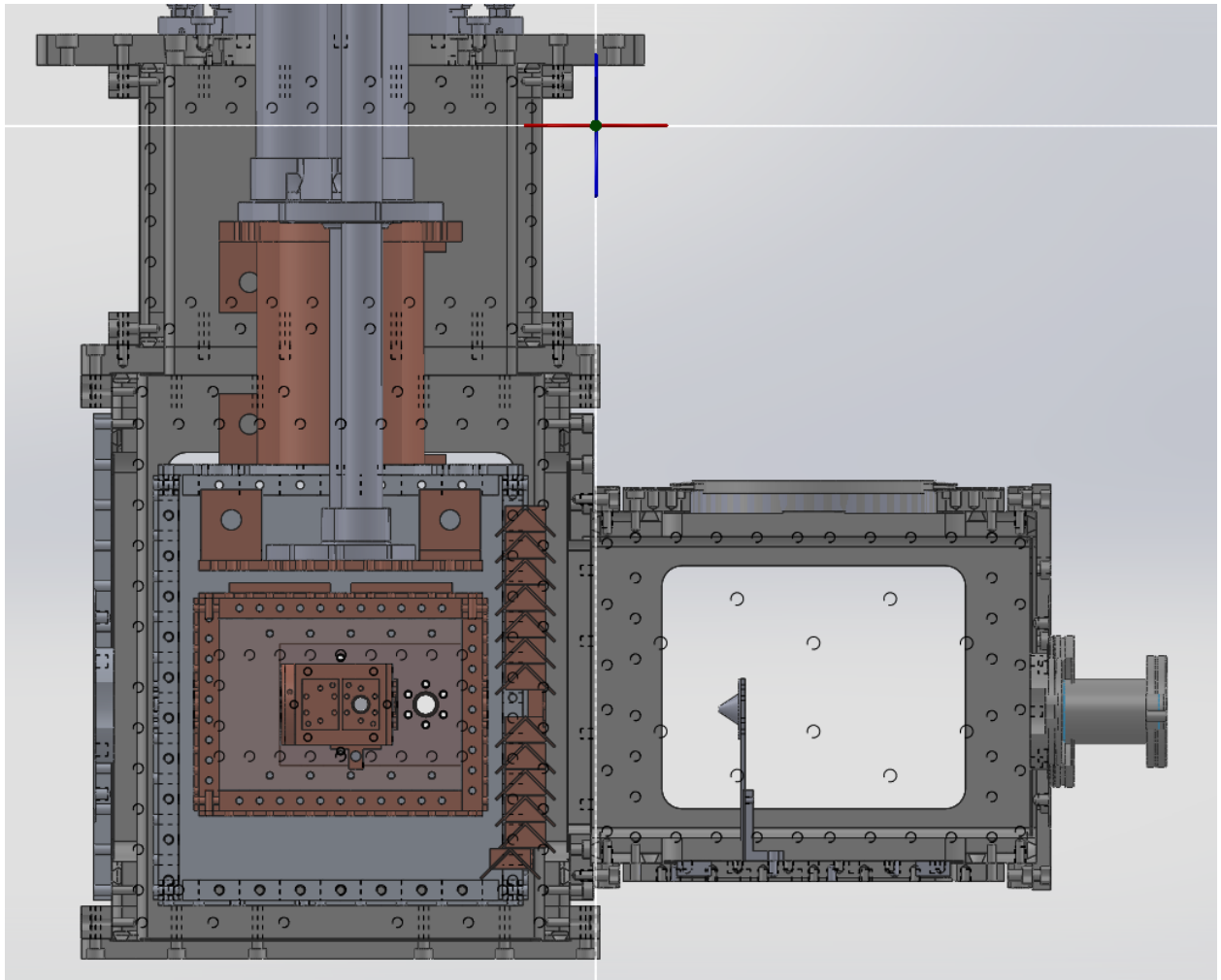


Figure 3.2: Cross sectional view of CBGB in solidworks. Components include copper sheath for PTR, aluminum radiation shield with chevron baffles, copper shield and experimental cell, and skimmer mounted in stem chamber. The baffles allow for gas to flow into the cold region of the beam apparatus, while preventing 300 K black body radiation from hitting the inner shield and cell.

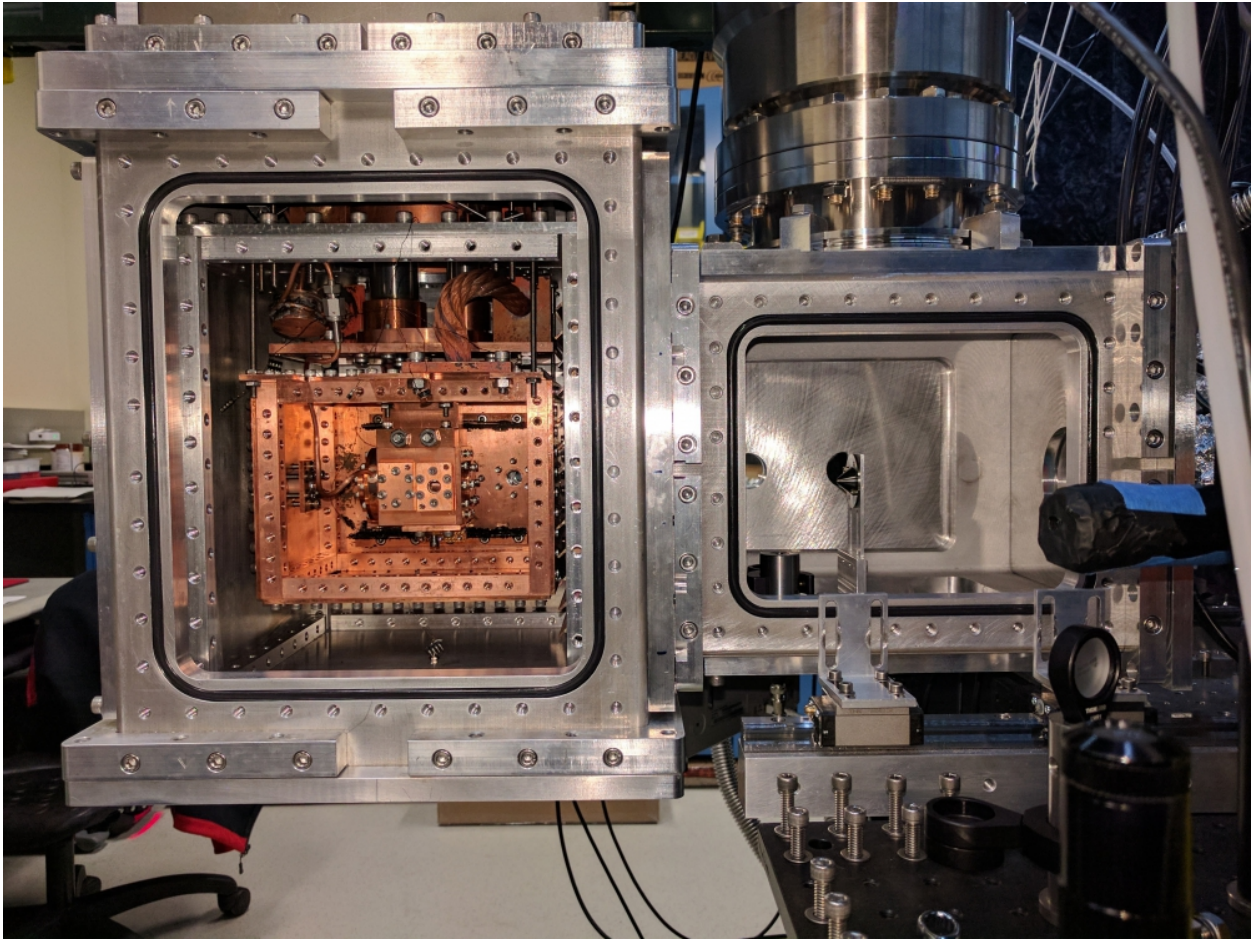


Figure 3.3: Cross sectional view of CBGB with side walls removed from the outer vacuum chamber, 40 K aluminum radiation shield, and inner 4 K cryopumping shield exposing the inner experimental cell. A skimmer is mounted in the stem region.

### 3.1.1 Heat Load and Thermal Conductivity

To produce a beam of cold particles, various components need to be held within specific temperature ranges to ensure proper operation. Considering neon as the buffer gas species of choice, we maintain the experimental cell at 20 K to prevent the neon from freezing to the walls and maintain a high stagnation density that allows for tuning of the flow regime. Conversely, we need the cryopumping shield surrounding the experimental cell to maintain

a temperature  $< 17$  K so that the neon that escapes the cell is readily captured, as the turbo connected to the stem chamber cannot keep up with the gas load. A lack of proper cryopumping results in high densities in the chamber, which scatters the beam.

The PTR 40 K cooling stage has 40 W of cooling power, while the lowest 4 K stage has only 4 W. The low cooling power of the lowest stage means that extra care is needed to minimize the heat transfer to the stage from the higher temperature regions including black body radiation and conducted heat from high temperature surfaces.

Material choices used in the CBGB are dictated by their thermal conductivity down to the temperature ranges of interest. At room temperature, thermal conductivity ( $k$ ) of a material is dominated by transfer of energy via phonons through the material. In this regime, different alloys and purities of a material do not greatly affect the conductivity. But once we enter cryogenic temperatures, the conductivity is dominated by electron motion through the material, meaning that purer samples have fewer imperfections to scatter off of, yielding higher conductivities.

Al 6061 was chosen for the radiation shield for its thermal conductivity ( $k_{Al6061}(T = 40$  K) = 70 W/(m K)[?]), ease of machining, as well as lightweight properties. The thermal mass of the aluminum shield coupled with its relatively lower thermal conductivity (compared to Cu 10100) means the cool down of this region limits the cool down process to 6 hr until at workable temperatures. The face of the aluminum shield on the outgoing beam side was fitted with a set of stacked chevron baffles as seen in figure 3.2. The baffle design blocks stray light from entering the radiation shield, while enabling gas to pass from the enclosed shields into the stem region, preventing high density regions from forming and scattering the beam. Conversely, the baffles allow for gas within the stem region to reenter the cryogenic shields and facilitate cryopumping of stray particles.

The copper region contains the experimental cell, enclosed by a copper shield that acts as a cryopumping surface at the appropriate temperatures. At cryogenic temperatures, it's convenient to characterize the conductivity of a copper with the residual resistance ratio ( $RRR = \frac{R(T=295\text{ K})}{R(T=4\text{ K})}$ ), where  $R(T)$  is the measured resistance at temperature  $T$ , which can be

related to the thermal conductivity with the Wiedemann-Franz Law.<sup>[?]</sup> Cu 10100, or oxygen free copper, was chosen for these components for its high thermal conductivity through to 4 K,  $RRR = 2000$ ,  $k_{Cu10100}(4 \text{ K}) = 10^4 \text{ W}/(\text{m K})$  compared to <sup>[?]</sup>.

Because it is heat sunk into the same cooling stage as the experimental cell, the copper shield does not act as a radiation shield for it does not redirect the heat load away from the experimental cell's cooling surfaces. For the experimental cell to hold an appreciable vapor pressure, while the thermally linked shield acts as a cryopumping surfaces, the two components will need to held at different temperatures. The experimental cell is held at a higher temperature than that of the cryopumping shield with a resistive heater, which is monitored and controlled with a temperature sensor diode (DT-670) and a Lakeshore controller (Model 325). A SS316 ( $k_{SS316}(T = 40 \text{ K}) \approx 7 \text{ W}/(\text{m K})$ ) stand off is used to create a poor thermal bridge between the two regions, allowing for a constant thermal gradient.

The main heat loads onto the system are those from the black body radiation, as well as the stainless steel rods supporting the shields from the top mounting plate. The temperature over the system may be determined by solving the heat/diffusion equation given proper boundary conditions. We use Fourier's Law to approximate the conductive heat loads through individual pieces

$$\dot{Q} = \frac{A}{l} k \Delta T \quad (3.4)$$

Where  $\dot{Q}$  is the rate of heat transfer,  $A$  is the cross sectional area of the component in question,  $l$  is the length of the component, and  $k$  is the thermal conductivity of the material. In general, we should be using the integral form where we have a temperature dependent thermal conductivity,  $k(T)$ , but approximate it to be constant. The main conductive heat loads come from the SS316 rods that mechanically anchor the shield components to the top chamber plate. On the 4 K cryopumping shield, there are 4 such rods, in total, contributing  $\approx 60 \text{ mW}$  of power to the 4 K cooling stage.

Aside from the conductive heat load, black body radiation is the main source of heat load onto the cold regions. We describe the power radiated from a source with the Stefan-

Boltzmann law:

$$\dot{Q} = A\epsilon\sigma T^4 \quad (3.5)$$

Where  $A$  is the area of the emitting object,  $\epsilon$  is the emissivity of the surface, and  $\sigma$  is the Stefan-Boltzmann constant. To find the power incident between two surfaces (1, 2) though, we find the form to be:

$$\dot{Q} = \sigma A(T_1^4 - T_2^4) \frac{\epsilon_1 \epsilon_2}{\epsilon_1 + \epsilon_2 - \epsilon_1 \epsilon_2} \quad (3.6)$$

In order to characterize the beam inside the CBGB, fused silica windows were mounted onto every shield to allow for optical access. These may pose a problem, as this line of sight allows for radiation coming from room temperature sources to heat up the inner components. The peak wavelength of a black body source at a temperature  $T$  is described by Wien's displacement law:

$$\lambda_{max} \approx \frac{2900}{T} \mu\text{m} \quad (3.7)$$

One can see the peak wavelength from a room temperature source is around  $93 \mu\text{m}$ , which is readily blocked by our fused silica windows. In total, the maximal approximate incident black body power onto the 4 K region, including a 20% fudge factor, is on the order of 200 mK.

### 3.1.2 Gas Fill Lines

To have a functioning beam, we need to introduce both the buffer gas as well as the target species gas from room temperature without over burdening the cooling stage, or plugging the fill lines. The buffer gas fill line is made of thin walled SS316, minimizing the thermal connection between the room temperature mounting and the cold experimental cell. It is thermally anchored to the 40K cooling stage and then brazed onto a plate that mounts

to the experimental cell. To avoid local freezing of the buffer gas, the tubing must avoid cryopumping shield as contact. During normal operation, the buffer gas should be run to clear out the fill lines in atmosphere to flush out any atmospheric gasses that could have migrated into the tube. Since the tube goes down to cryogenic temperatures, any trace gasses will freeze and accumulate in the tubing and block the gas flow.

More care must be taken for the design of the water fill line, as it cannot make contact with any mildly cooled metal surface for fear of local freezing. The mating of the fill line to the experimental cell must also prevent excessive heat loads onto the cell while still enclosing the back side to preserve beam flux. With the design help of David Patterson, we utilize a thick walled 1/8" copper tube, with the tip bent at 90°, that enters from the bottom of the CBGB (figure 3.4), through the shields, into the back of the experimental cell. On the outside, the copper tube enters the CBGB through an Ultratorr fitting welded to an slotted plate that bolts to the bottom of the chamber in a recessed pocket. The combination of an Ultratorr fitting with the sliding plate allows for easy adjustment of the height and insertion depth of the bent end. By slathering the o-ring in the recessed pocket with silicon vacuum grease, one may also adjust the tubing in situ, but the CBGB should be gated off from the rest of the experiment as there is a high risk of letting in some atmosphere.

Inside the CBGB, leaving the back of the cell open with a hole eliminated conductive heat transfer between the fill line and the cell, but did not allow for a reliable beam. Ice readily formed on the nearby copper surfaces and slowly closed the back opening, decreasing the effective  $A_{aperture}$  of the cell as a function of time, thus changing the flow properties. The back was replaced with a 0.001" film of kapton with a cross cut into the middle for the fill line as seen in figure 3.5. The poor thermal conductivity of kapton (0.5 W/(m K)) ensures minimal conductive heat load to the cell, prevents ice from forming, while also closing the back of the cell. With the kapton, the beam may be run continuously with water entrained in the neon buffer gas for over 10 hours without any change in beam properties. Collisions with buffer gas particles within the cell transferring heat between the fill line and cell walls added < 0.05W of heat load. Solving the integral form of Fourier's Law in cylindrical coordinates

(3.8), we find that the heat load through the kapton is only 0.019 W.

$$\dot{Q} = \frac{2\pi k l (T_1 - T_2)}{\ln(r_2 - r_1)} \quad (3.8)$$



Figure 3.4: The water fill line, sealed by an ultratorr fitting and heated by nichrome wire. A shut off valve and vernier valve are used to regulate the flow of water into the buffer gas cell.

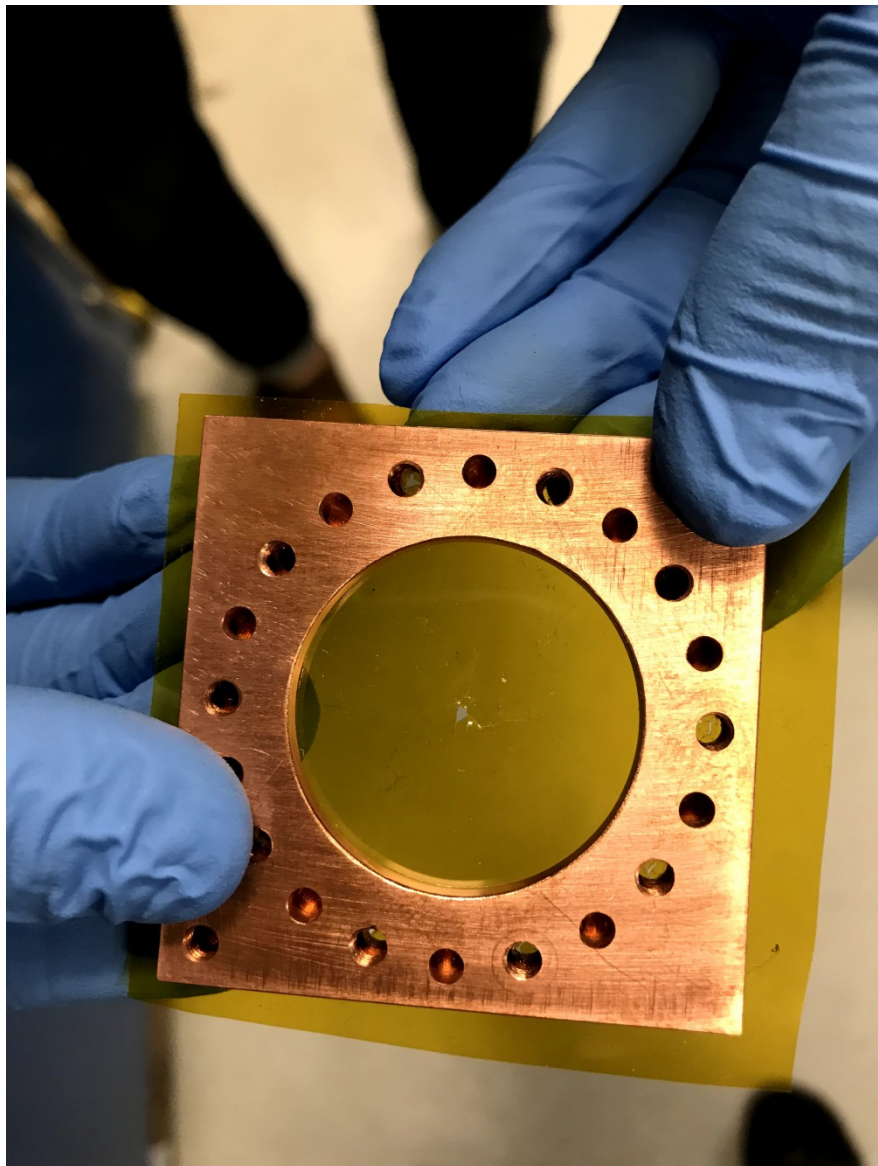


Figure 3.5: A kapton film serves as the back wall of the buffer gas cell with a hole punctured for the insertion of the water fill line. The kapton surface seals the back of the cell for a stronger forward beam, while limiting the heat load from a room temperature fill line, and resisting ice formation allowing for continuous and consistent operation with water for over 10 hours.

## 3.2 Beam Density and Extraction

We need to have a fairly dense beam of our target species to reach the ion trap center in order to get a reasonable signal to noise of the cold molecule reaction as opposed to the warm background reactions. A dense beam coupled with good cryopumping ensures that the signals seen are primarily, if not solely due to the introduction of the cold beam.

The downstream properties of a beam all start with the buffer gas stagnation density within the experimental cell. The stagnation density is the steady state buffer gas density that is determined by the physical dimensions of the cell, including the aperture, and the gas throughput, or number flow rate going in. Experimentally, it's preferable to use volumetric flow rates when operating the apparatus, so for calculations, that needs to translate to number flow rate using the ideal gas law:

$$\dot{N} = \frac{Pf}{k_B T}$$

where  $P$  is pressure and  $f$  is the volumetric flow rate, this translates to about  $4 \times 10^{17}$  particles/s<sup>-1</sup> for 1 SCCM of gas flow. By solving for the number density in the flow out of an aperture with molecular flow, we find that the stagnation density within the cell can be shown as:

$$C_{ap} = A \frac{\bar{v}}{4}$$

$$n_b = \frac{4\dot{N}}{A_{aperture} \bar{v}} \quad (3.9)$$

In general, buffer gas beams operate with stagnation densities around  $10^{15} - 10^{17}$  cm<sup>-3</sup>. Outside of the cell, we can describe the density of the beam as a function of distance. [32]

$$n(z) = \frac{n_0}{2} \left( 1 - \frac{z}{\sqrt{z^2 + a^2}} \right) \quad (3.10)$$

Where  $z$  is the distance from the aperture into the vacuum side,  $n_0$  is the initial number density,  $a$  is the radius of the aperture. In the far-field, this goes to:

$$n(z) = \frac{n_0 a^2}{4z^2}$$

But there is something that we must consider, that is that we aren't seeing the full aperture while we are at all locations, we are actually seeing an appended area due to the inclusion of apertures and skimmers in the way. While only  $n_0$  is only dependent on the aperture size of the cell,  $n(z)$  will have a set value defined by the smallest aperture in the beam path. For us, although our cell aperture is  $\approx 9$  mm in diameter, we have multiple apertures and skimmers in the way, the smallest of which is a skimmer from Beam Dynamics with a diameter of 2 mm.

Sympathetic cooling occurs through collisions between the hot target species being introduced and the cryogenic buffer gas particles. We may consider each hard sphere collision to transfer heat from the hot target species ( $T_s$ ) to the cold buffer gas at constant temperature ( $T_b$ ).

$$\Delta T_s = -\frac{T_s - T_b}{k}$$

Where  $k \equiv \frac{(m_b + m_s)^2}{2m_b m_s}$ . For the  $N^{\text{th}}$  collision, we can write the change in temperature:

$$T_s(N) - T_s(N-1) = -\frac{T_s(N-1) - T_b}{k}$$

For large values of  $N$ , where the change in temperature becomes small, we can turn the discrete equations into a differential form.

$$\frac{dT_s(N)}{dN} = -\frac{T_s(N) - T_b}{k}$$

Which we can solve with the condition that  $T_s(0) = T_0$

$$\begin{aligned} \frac{T_s(N)}{T_b} &= \left( \frac{T_0}{T_b} - 1 \right) e^{-\frac{N}{k}} + 1 \\ &\approx \frac{T_0}{T_b} e^{-\frac{N}{k}} + 1 \end{aligned}$$

Assuming an ablation loading process in which  $T_0 = 1 \times 10^4$  K, we find that it still only takes  $\approx 12$  collisions to thermalize the target species within a factor of 2 of the buffer gas temperature. In general  $\approx 100$  collisions are needed to relax rotational states to the same range. Vibrational degrees of freedom may take upwards of  $10^4$  collisions to fully thermalize if the elastic collision energy is much lower than the internal vibrational level.

By finding the mean free path, we can consider the characteristic length the particles travel to be thermalized with the buffer gas, this is then compared to the characteristic length of the cell to determine the effectiveness of the cooling.

$$\lambda = \frac{A_{\text{aperture}} \bar{v}}{4f\sigma \sqrt{m_s/m_b}}$$

If a species is introduced into the buffer gas cell that has a lower vapor pressure than that is allowed at the current temperature, it will be lost when it comes in contact with the cell walls. The rate of this loss can be described as the characteristic time of diffusion of a particle in the buffer gas to the physical dimensions of the cell set the diffusion time constant:

$$\tau_{\text{diff}} = \frac{16}{9\pi} \frac{A_{\text{cell}} n_{0,b} \sigma}{\bar{v}} \quad (3.11)$$

where  $\sigma$  represents the collisional cross section for the buffer gas with the target species. On the other hand, we have the characteristic pump out time given by the conductance of a cell aperture:

$$\tau_{\text{pump}} = \frac{4V_{\text{cell}}}{\bar{v} A_{\text{aperture}}} \quad (3.12)$$

By combining equations eqs. (3.11) and (3.12), we can get a dimensionless ratio,  $\gamma$  that characterizes the extraction fraction out of the cell.

$$\gamma = \frac{\tau_{\text{diff}}}{\tau_{\text{pump}}} = \frac{\sigma f}{L_{\text{cell}} \bar{v}} \quad (3.13)$$

Notice that the  $\gamma$  factor does not depend on aperture size, this is generally true, but increasing the aperture size will lower your number density within the cell, which then influences the characteristic length scale of thermalization. Larger apertures thus run the risk of not allowing your particles to fully thermalize in rotational/vibrational states. But decreasing the aperture size can make alignment as well as controlling the number density more difficult, as finer control over the flow rate is necessary for equivalent flow regimes.

Using equations eqs. (3.13) and (3.9), knowing the physical dimensions of the experimental cell, we find that we may derive theoretical characteristics of the buffer gas beam. During normal operation, our main control over the buffer gas beam is the manipulation of the Ne flow rate, so as a function of buffer gas flow rate ( $f$ ), we may see how key properties are affected.

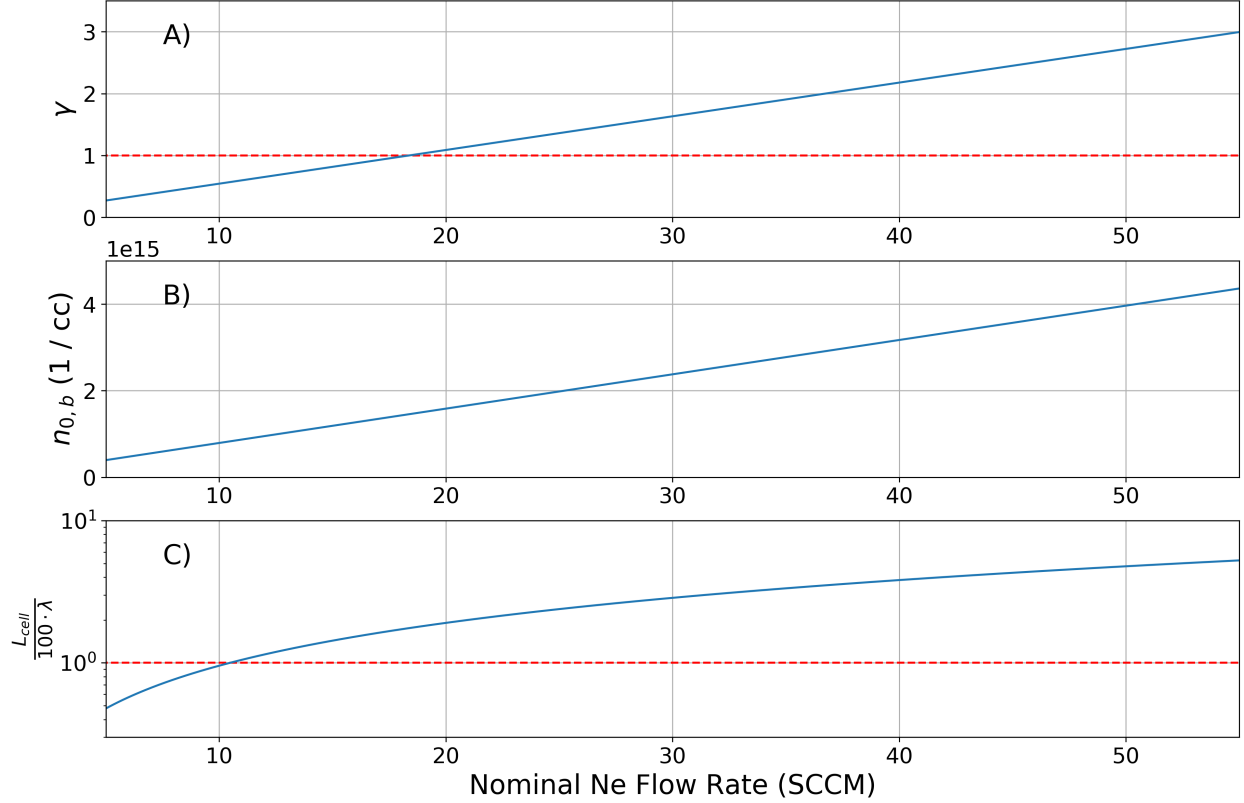


Figure 3.6: Theoretically derived buffer gas beam properties of interest given the physical dimensions of our cell in particular:  $d_{aperture} = 9$  mm. A)  $\gamma$  extraction ratio, dotted red line indicates  $\gamma = 1$  where hydrodynamic entrainment begins. B) Number density of buffer gas species within the experimental cell, given an enclosed back wall. The density of target species introduced should stay under 1% of the buffer gas density for other properties to hold. C) Number of collisions a target species particle would expect before extraction out of the cell, the dotted red line indicates 100 collisions before extraction, when rotational degrees of freedom are characteristically thermalized.

### 3.2.1 Direct Beam Measurement and Parameterization

Although we can make statements about the properties of the buffer gas itself in the beam, we are most interested in the properties of the target species introduced into the cell. In

particular, understanding the extraction ratio  $\gamma$ , as well as the velocity, gives us a good handle on the target species characteristics.

To observe the extraction of the target species from the cell, a residual gas analyzer (RGA) is used to determine the density of the beam in the ballistic regime upstream from the ion trap. To ensure the highest possible signal, the Swagelok vernier flow valve used to regulate water vapor flow into the cell is fully opened. During normal operation of the beam in conjunction with the ion trap, the valve is set to a much smaller opening to ensure the properties of the beam are dominated by the buffer gas species, as well as to control the reaction rates.

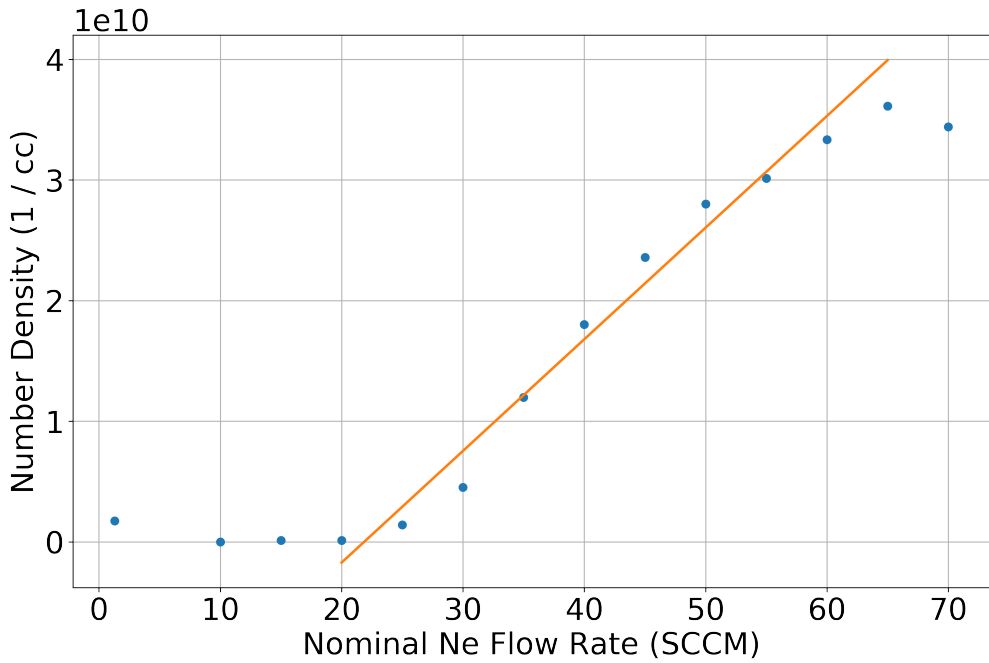


Figure 3.7: Fitted linear behavior of  $\text{H}_2\text{O}$  entrained in a Ne buffer gas beam 30 cm from cell aperture. The onset of hydrodynamic entrainment seems to occur around 20 SCCM up through 60/65 SCCM where the  $\text{H}_2\text{O}$  extracted into the beam has a clear linear form of  $(9.2 \times 10^8 \text{ cm}^{-3}/\text{SCCM})f - 2 \times 10^{10} \text{ cm}^{-3}$ .

We find that theoretical calculations and experimental results agree that the onset of hydrodynamic entrainment occurs at a buffer gas flow rate of  $\approx 20$  SCCM. We can combine

the results here with equations eqs. (3.3), (3.9) and (3.10) to map out beam densities subject to all other possible parameters we may want to adjust, over our entire experimental apparatus. We start by scaling a combination of equations eqs. (3.9) and (3.10) by  $\alpha$ , a buffer gas to target species density scaling factor.

$$n(z) = \alpha \frac{f}{A_{\text{aperture}} \bar{v}} \left( 1 - \frac{z}{\sqrt{z^2 + a^2}} \right)$$

But this only holds true for the region in which the number density is linearly dependent to the buffer gas flow rate, not over all possible ranges; we've seen that the target species only behaves linearly in the hydrodynamic regime. This means that we should be equating the function of  $n(z)$  with the linear fit performed on the data for the parameters the data was taken at.

$$mf + b = \alpha \frac{f}{A_{\text{aperture},0} \bar{v}_0} \left( 1 - \frac{z_0}{\sqrt{z_0^2 + a_0^2}} \right)$$

Where  $z_0 = 30$  cm, being the distance of the RGA from the cell aperture, and  $z = 0 = 2$  mm, for the smallest aperture seen during the experimental run. We also define the experimental scaling factors:

$$\begin{aligned} \alpha &= \frac{m}{\beta} + \frac{b}{\beta f} \\ \beta &= \frac{1}{A_{\text{aperture},0} \bar{v}_0} \left( 1 - \frac{z_0}{\sqrt{z_0^2 + a_0^2}} \right) \end{aligned}$$

Thus, we obtain a form that includes experimentally derived scaling factors that allows us to project the target species density over the length of the system.

$$n(z) = \frac{mf + b}{A_{\text{aperture}} \bar{v} \beta} \left( 1 - \frac{z}{\sqrt{z^2 + a^2}} \right) \quad (3.14)$$

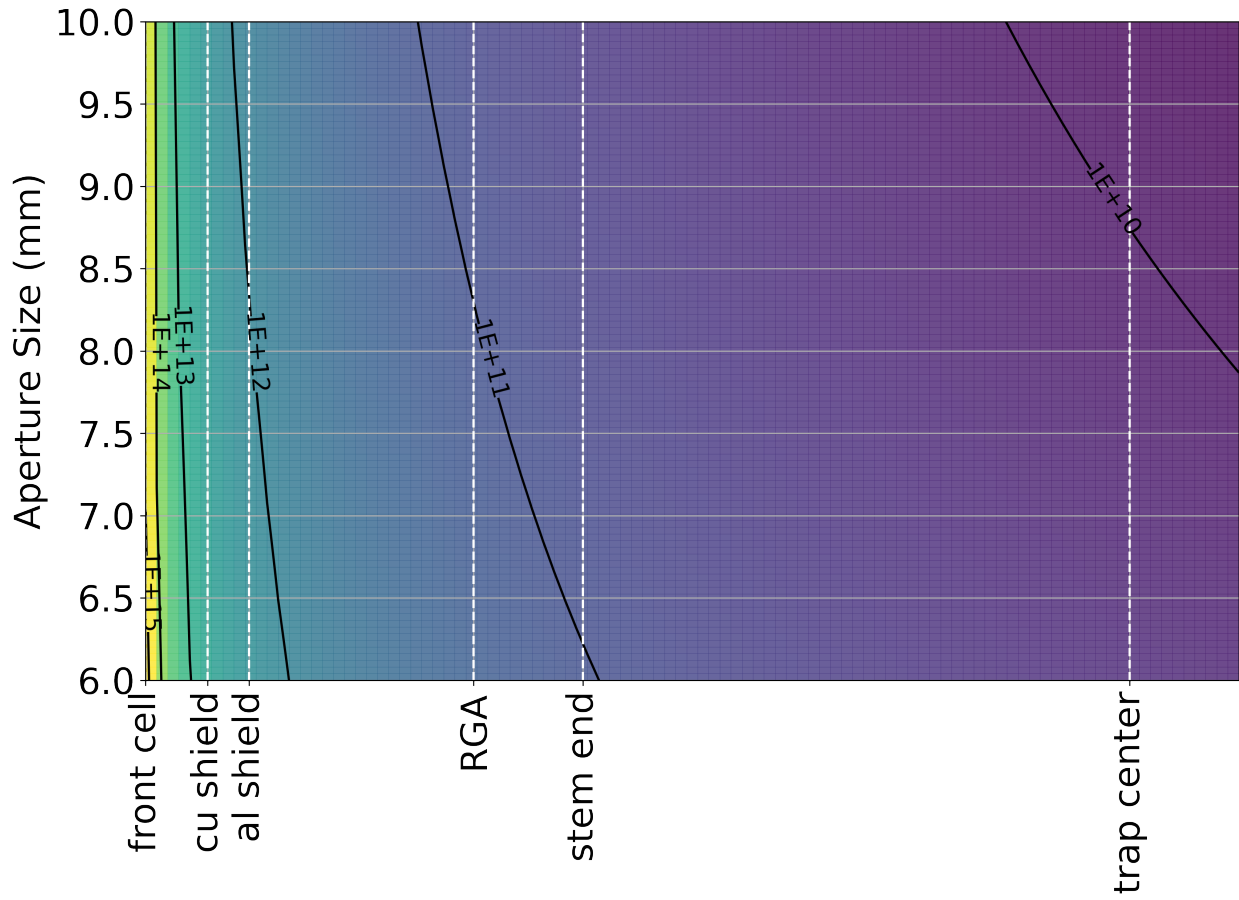


Figure 3.8: Projected beam densities with a Ne flow rate of 30 SCCM with various distances of interest within the chamber. Beam densities shown are without throttling of the H<sub>2</sub>O flow valve.

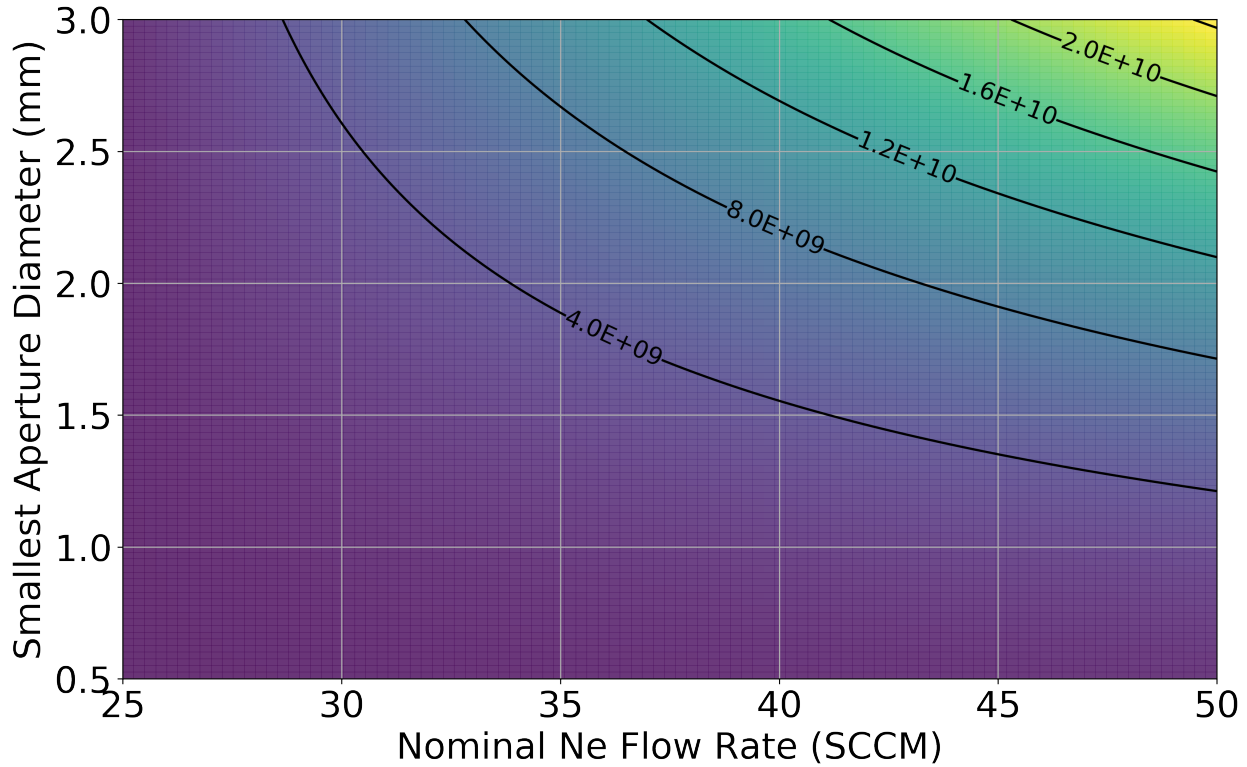


Figure 3.9: Projected beam densities at the trap center over various nominal Ne flow rates and smallest skimmer aperture size. Beam densities shown are without throttling of the H<sub>2</sub>O flow valve.

One should not forget the mass dependence in the thermal velocity equation, which leads us to conclude that the choice of the species is a statement of the dominant species in the beam. If we choose to calculate the thermal velocity of the target species found in the beam due to the theoretical thermal velocity of the buffer gas species, that indicates that the beam properties are still dominated by the buffer gas species. At target species/buffer gas ratios greater than 1/100, we may start to see the effects of the target species on not only the beam density, but also forward velocity.

### 3.2.2 Beam Density at Ion Trap

Determining the water density in the beam at the ion trap is more difficult than in the CBGB and stem region. During normal operation of the CBGB, neither the RGA, nor the ion gauge in the trap chamber, which are off the beam axis and in a nipple, are unable to detect a change in the background water pressure. With the characterization of the  $\text{Be}^+ + \text{H}_2\text{O}$  reaction pathways, we were able to validate both experimentally and theoretically, the rate constant and that it follows the ADO model (Section 5.1). The procedure using this method as well as subsequent results are discussed in Section 7.1.

## 3.3 Beam Velocity

Over the various flow regimes; effusive, intermediate, and supersonic, the forward velocity and distributions change drastically from 150 m/s up to 800 m/s. We first consider the edge cases of the effusive and supersonic regimes. In the effusive regime, we make the assumption that the particles in the cell are non-interacting. We may rewrite the equation 3.2 as a function of the mean velocity  $\bar{v}$  into a simpler form .

$$f(v) = \frac{32}{\pi^2} \frac{v^2}{\bar{v}^3} e^{-4v^2/\pi\bar{v}^2} \quad (3.15)$$

To get the velocity distribution in the beam, we can calculate the distribution of particles incident on an aperture in the cell.

$$\begin{aligned} f_{beam}(v) &= \frac{v}{\bar{v}} f(v) \\ &= \frac{32}{\pi^2} \frac{v^3}{\bar{v}^4} e^{-4v^2/\pi\bar{v}^2} \end{aligned}$$

For low Reynold's numbers ( $\text{Re} < 1$ ) the flow at the aperture is purely molecular, which means that there are few to no collisions. This allows us to continue to use the Maxwell-

Boltzmann distribution to describe the forward velocity [22].

$$\bar{v}_{\parallel} = \int_0^{\infty} v f(v) dv \approx 1.2 \bar{v} \quad (3.16)$$

The spread of the forward velocity of an effusive beam is the full width half max (FWHM) of the Maxwell-Boltzmann distribution:  $\Delta \bar{v} \approx 1.5 \bar{v}$ . As the Reynolds number increases, one can reach the supersonic regime ( $Re > 100$ ) where the forward velocity reaches  $1.4 \bar{v}$  and the distribution drastically narrows.[22, 32]

But as the flow regime nears the supersonic regime, forward collisions around the aperture cause boosting of the average velocity as well as a decrease in the velocity spread.

Supersonic beam velocities can be shown to be:[32]

$$v_{\infty} = \sqrt{\frac{2k_b T_0}{m} \frac{\gamma}{\gamma - 1}}$$

Where  $\gamma$  is the heat capacity ratio  $C_p/C_v$ , and  $T_0$  is the original temperature of the source.

The intermediate regime in between the effusive and supersonic regimes is particularly difficult to model, for there are some collisions at the aperture unlike the effusive regime, causing some boosting and narrowing, but not enough to treat the behavior as fully fluid-like. The section 3.2 results show that we can produce a beam in this intermediate regime by demonstrating clear hydrodynamic entrainment.

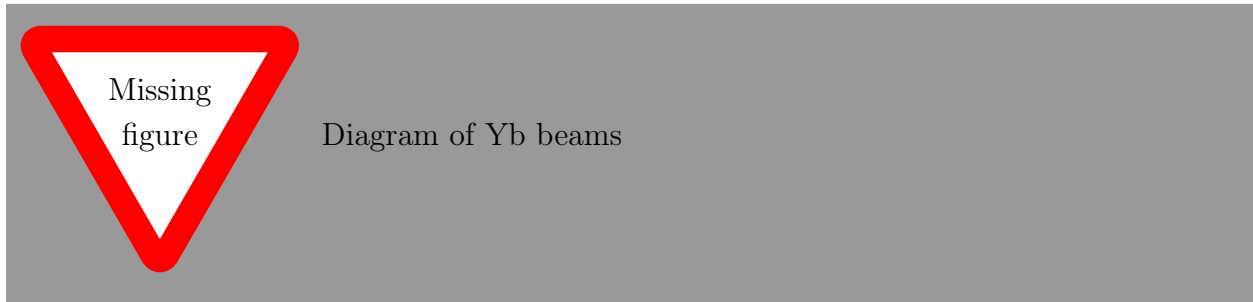
To better understand the reaction temperatures we will be able to reach, we need a characterization of the beam's velocity, more specifically, the velocity of the target species entrained within the buffer gas. The ideal target species is one with a reliable loading method and can be directly detected in small amounts. Ytterbium metal is known to have good ablation properties and the produced neutrals have well known spectra. By ablating ytterbium foil inside of the experimental cell while the neon gas is being introduced, the ytterbium is cooled by the buffer gas and carried out of the cell. As long as the target species number density is a trace amount in comparison to the bulk buffer gas number

density (0.1%), the flow characteristics are dominated by the buffer gas species [21]. Based upon the results of our direct RGA measurements of the beam density, we know that the cell parameters used in the previous measurement land us in the intermediate flow regime due to the clear evidence of hydrodynamic entrainment.

To determine the velocity of the beam, we ablate an ytterbium target mounted inside the experimental cell where both neon and water are being introduced. The resulting beam is then hit with a 399 nm laser to excite the Yb isotope transitions. The laser is scanned over 3.5 GHz, encompassing all possible Yb isotope peaks. Two scans were taken, one with the 399 nm light perpendicular to the beam path, and the other where the laser is coming in with an angle of 57.3°. The resulting spectra are then fitted with summed Gaussian functions with predetermined isotopic shifts, giving us the center ( $^{174}\text{Yb}$ ) frequency, as well as the widths of the lines. Between the transverse and angled scans, we find an offset in the spectrum caused by the doppler shift, seen in figure 3.10:

$$\Delta f = \frac{\Delta v}{v} f \cos(\theta) \quad (3.17)$$

Where  $f$  is the fundamental center frequency,  $\Delta f$  is the offset observed,  $v$  is the forward velocity of the excited  $^{174}\text{Yb}$ , and  $\theta$  is the angle of the beam with respect to the beam. Using equation 3.17, we find the forward velocity of the beam is around 150 m/s, within the expected range for a hydrodynamically entrained beam. The fitted shared widths give us a beam temperature of 20 K, which is exactly what the experimental cell was held to.



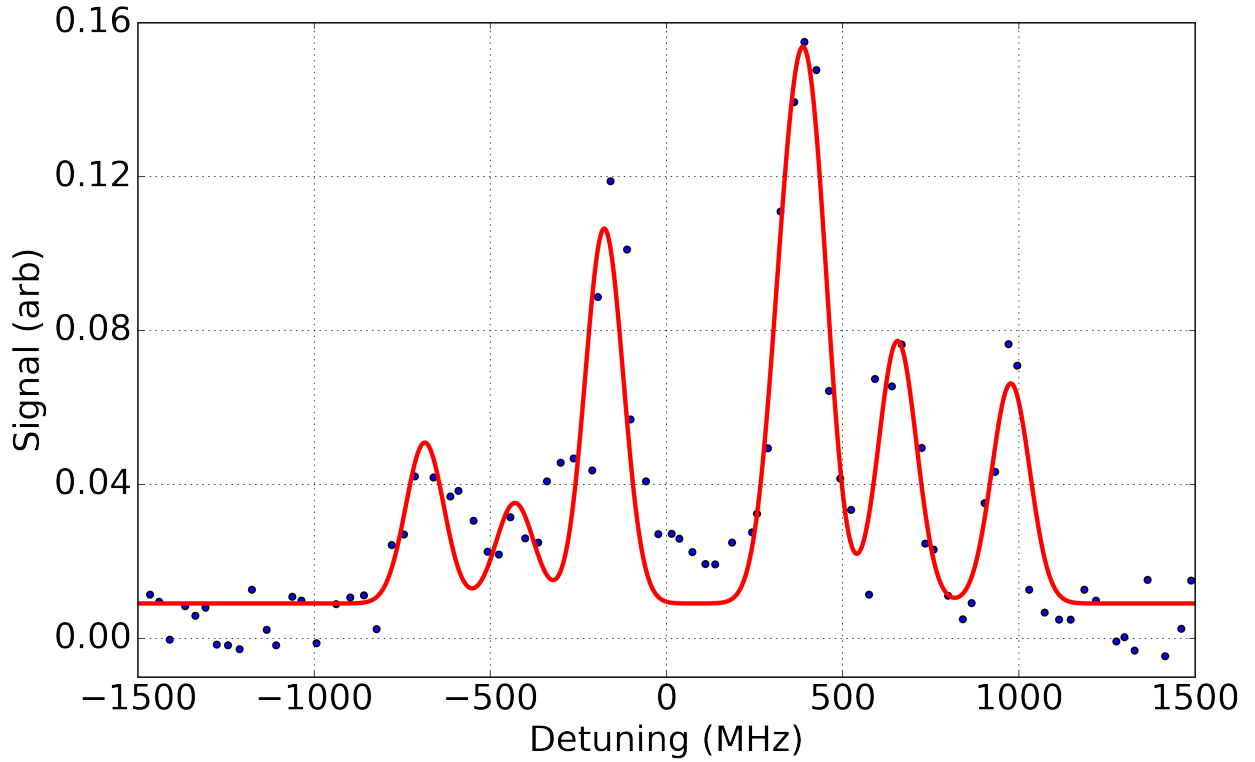


Figure 3.10: Angled longitudinal scan of Yb fluorescence collected by PMT at  $\approx 24$  cm from cell aperture. A fit of all isotopic peaks yields mggm

We find that the Yb is entrained within the neon and sympathetically cooled to the cell's temperature. The water that is also introduced in the beam will also be at a similar temperature and forward velocity as long as the neon density is much larger than that of the water when the beam dynamics is dominated by the properties of the buffer gas species.

### 3.4 Beam Shuttering

With the RGA in the beam path, we were able to open and close a shutter in the beam path and see an extinction of the water signal, but a more accurate representation would be from the ions in the trap themselves. We know that the trapped  $\text{Be}^+$  ions will react with  $\text{H}_2\text{O}$  to predominately produce  $\text{BeOH}^+$ , which we see as a drop in the fluorescence. Figure 3.13

shows fits of the fluorescence decay as a beam from the CBGB is suddenly blocked by our shutter in the beam line. Comparing the fitted reaction rates, we find that they agree with the background rates found as shown in figure 3.12. This indicates to us that we indeed have a beam of cryogenic water coming from the CBGB, as seen by the sudden extinction of the  $\text{Be}^+ + \text{H}_2\text{O}$  reaction.

To accurately control the reactions occurring in the ion trap, it is ideal to be able to quickly turn the beam on and off. Controlling the fill lines outside of the chamber is not ideal, as thin tubing was used, yielding very low conductances. The characteristic time of flow through a tube can be shown to be  $\tau_{tube} = CV$ , where  $C$  is the conductance and  $V$  is the volume of the tube in question. Turning on and off the flow outside of the chamber would give time constants in the range of seconds. To more deterministically control the beam flux, we insert a vacuum compatible Uniblitz VS35 35mm Optical Shutter in the beam line. The shutter does not create a seal within the chamber, background gasses may flow around and influence the beam.

Running the beam with the shutter in between the RGA and experimental cell, we find that there is a distinct difference in the  $\text{H}_2\text{O}$  signal when the shutter is open and closed. Using laser cooled  $\text{Be}^+$ , we find the difference in the reaction rate both independently, as well as in situ, figs. 3.12 and 3.13.

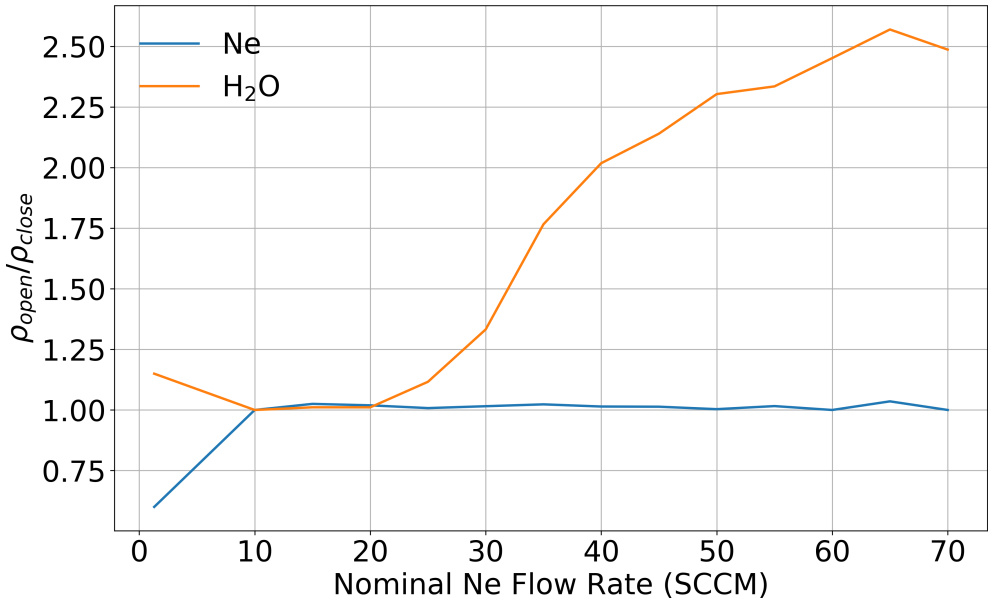


Figure 3.11: Ratios of water and neon from the beam when the Uniblitz shutter is opened and closed. Detection is done via RGA placed 30 cm from the cell aperture.

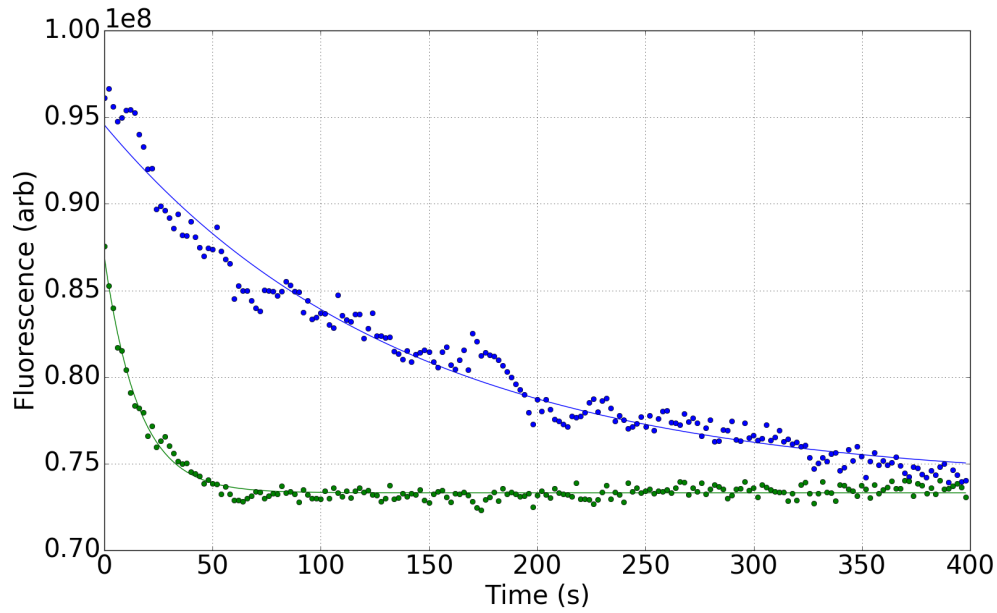


Figure 3.12: Fluorescence decays of loaded  $\text{Be}^+$  ions exposed to a cold water beam with an inline shutter either opened, in green ( $\tau = 7.23 \times 10^{-3}\text{s}$ ) or closed, in blue ( $\tau = 6.37 \times 10^{-2}\text{s}$ )

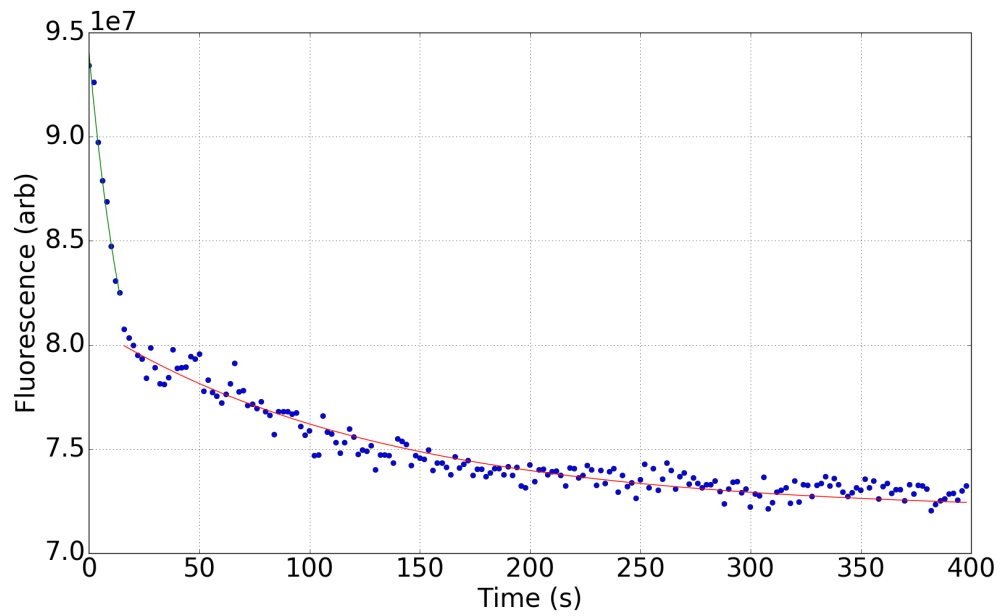


Figure 3.13: Fluorescence decays of loaded  $\text{Be}^+$  ions exposed to a cold water beam with an inline shutter opened, in green ( $\tau = 5.37 \times 10^{-2}\text{s}$ ) or closed, in red ( $\tau = 7.59 \times 10^{-3}\text{s}$ )

# CHAPTER 4

## Trapping and Cooling Ions

### 4.1 Ion Trapping

Use RF fields at 1MHz in a linear quadrupole ion trap (LQT) to trap charged particles spatially.[51]

Consider a 3 dimensional potential that could trap a particle, we may assume the form:

$$\Phi = \frac{\Phi}{r_0^2} \sum_{i=1}^3 \alpha_i r_i^2$$

Where  $r_0$  is the distance to the potential surfaces and  $r_{1,2,3}$  correspond to  $x$ ,  $y$ , and  $z$  respectively. But by Laplace's equation,  $\Delta\Phi = 0$ , we don't get a confining potential as one of the terms  $\alpha_i$  must be negative, leading to a saddle-like potential. To get around this, we may vary the potential in time to create a pseudo-potential that can confine a subset of ions:

$$\Phi_0(t) = V_{DC} + V_{rf} \cos(\Omega_{rf}t)$$

Solving for the equations of motion, we find:

$$\ddot{r}_i + \frac{2\alpha_i e}{mr_0^2} (V_{DC} + V_{AC} \cos(\Omega_{rf}t)) r_0 = 0 \quad (4.1)$$

To solve this, we make changes of variable:

cite  
the  
OG  
Paul

$$a = \frac{8eV_{DC}}{mr_0^2\Omega_{rf}^2} \quad (4.2)$$

$$q = \frac{4eV_{DC}}{mr_0^2\Omega_{rf}^2} \quad (4.3)$$

$$\tau = \frac{1}{2}\Omega_{rf}t$$

To then find the characteristic Mathieu equation:

$$\frac{\partial^2 u}{\partial \tau^2} + (a - 2q \cos(2\tau))u = 0 \quad (4.4)$$

A diagram showing stable solutions to equation 4.4 with the experimental trap values is shown in figure 4.2. To provide full 3 dimensional trapping, DC end cap voltages of around 200 V are applied to contain the ions axially.

Considering our linear quadrupole trap, where we have radial symmetry, the conditions for the  $x$  and  $y$  orientations are the same, where  $a_x = a_y = -\frac{1}{2}a_z$  as well as  $q_x = q_y = -\frac{1}{2}q_z$ . As long as we are in a regime where  $a \ll q^2 \ll 1$ , we can approximate the pseudo-potential as a harmonic oscillator where multiples of the secular frequency are the allowed modes.

$$\omega_i = \gamma_i \frac{\Omega_{rf}}{2} \quad (4.5)$$

Where  $\gamma_i = \sqrt{a_i + \frac{q_i^2}{2}}$ . Inside this harmonic potential, the ions may move around up until the point at which they would hit the trap rods. Keeping with the harmonic potential approximation, we can characterize the maximum energy an ion may have in the trap to be when the energy of the ion at the condition where it would be displaced far enough to hit a rod.

$$E_0 = \frac{m}{2e}\omega_{sec}^2 r_0^2 \quad (4.6)$$

Compiling the relevant trap parameters and using equations eqs. (4.5) and (4.6):

| Parameter      | Value         |
|----------------|---------------|
| $r_0$          | 6.85 mm       |
| $\Omega_{rf}$  | $(2\pi)3$ MHz |
| $V_{DC}$       | 2 V           |
| $V_{rf}$       | 250 V         |
| $\omega_{sec}$ | 83 kHz        |
| $E_0(m/z = 9)$ | 3 eV          |

Table 4.1: Experimental trap parameters predominantly used in this thesis.

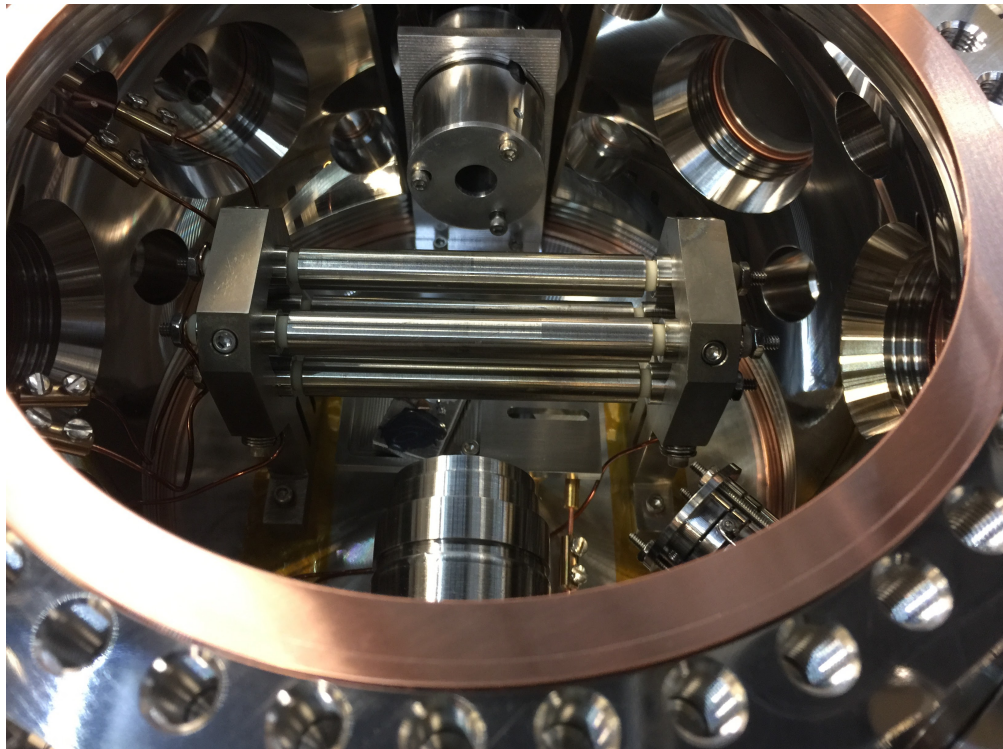


Figure 4.1: The ion trap inside of the experimental vacuum chamber. An Einzel lens and imaging objective are seen on the vertical axis.

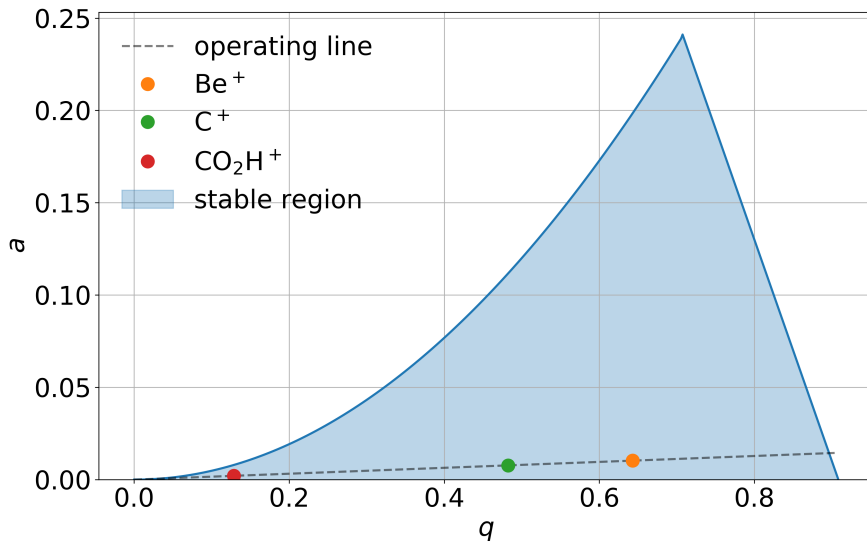


Figure 4.2: Stability diagram of the experimental ion trap with parameters defined in table 4.1. The trap is set up to be stable for ions of interest, including high mass reaction products, from  $\text{Be}^+$ , and  $\text{C}^+$  at  $m/z = 9$ , 12 to  $\text{CO}_2\text{H}^+$  at  $m/z = 45$ .

## 4.2 Vacuum Requirements

To reliably laser cool and trap ions into crystals for long periods of time, it is ideal to have ultra-high vacuum (UHV) which is generally defined as having a pressure  $< 10^{-9}$  Torr. Collisions with background gasses can be elastic, imparting energy to the ions, possibly enough to prevent a crystal from forming, or they can be inelastic, where a reaction may occur. In both instances, the rate at which these collisions occur is dependent on the density of the background gas in question, and the interaction potential.

For our experiment, we want to look at the reactions between our ions and  $\text{H}_2\text{O}$  introduced via the CBGB, meaning we need to limit the background  $\text{H}_2\text{O}$  content such that we may confidently say the reaction products are solely due to the cold water from the beam. Water is difficult to completely eliminate from a chamber because it sticks to the surfaces of walls when bouncing around, taking more time to reach a pump than other molecules or atoms.

We bake out chamber and all relevant components including the RGA nipple and TOF drift tube, while the turbo pump is constantly on.

We may verify the pressures within the chamber by looking at the reaction rate of:



Which has been observed to be  $k_{4.7} = (1.3 \pm 0.4) \times 10^{-9}$ , in goo agreement with the Langevin rate  $k_L = 1.6 \times 10^{-9}$ .[34] By monitoring the rate of fluoresce decay with the imaging system scaled by the P-state fraction, we find the pressure in our chamber is of  $\approx 10^{-10}$  torr of almost exclusively  $\text{H}_2$ , verified separately with the ion gauge.

As mentioned before, we want to introduce water into the beam via the CBGB, this poses a background water problem, as we need to connect the CBGB system with the ion trap chamber without introducing large amounts of  $\text{H}_2\text{O}$ . We directly connected the CBGB stem chamber to the ion trap chamber and turned on the cooling so that the cold CBGB surfaces act as cryopumps for background water. When we opened the gate valve, we found that the background pressure of water leaking in from the CBGB region reached values of  $10^{-8}$  torr. Since the CBGB region is constantly being opened and closed, it is regularly exposed to atmosphere, where then the surfaces collect water. Although the cold shields are effective in pumping the water out, there is still too much unbaked surface area that outgasses water. To get around this issue, we introduce differential pumping region consisting of a CF 2.75" cross with gate valves on either end, pumped by an Agilent 84FS turbo pump, and a leak valve for further utility, seen in figure 4.3. Inside of each gate valve, we added blank copper CF gaskets with centered apertures to reduce the conductance between the CBGB chamber and ion trap chamber while allowing the beam to pass through as unimpeded as possible. The aperture facing the CBGB is 4 mm in diameter, while the one facing the ion trap chamber is 10 mm in diameter. The cross is then baked to remove as much water content as possible. Subsequent tests observing reaction 4.7 while the cross is opened to the ion trap chamber show no observable difference in background pressure, while having all gate valves opened increased the background pressure to  $\approx 2 \times 10^{-9}$  torr, with no discernible contribution from

$\text{H}_2\text{O}$ .

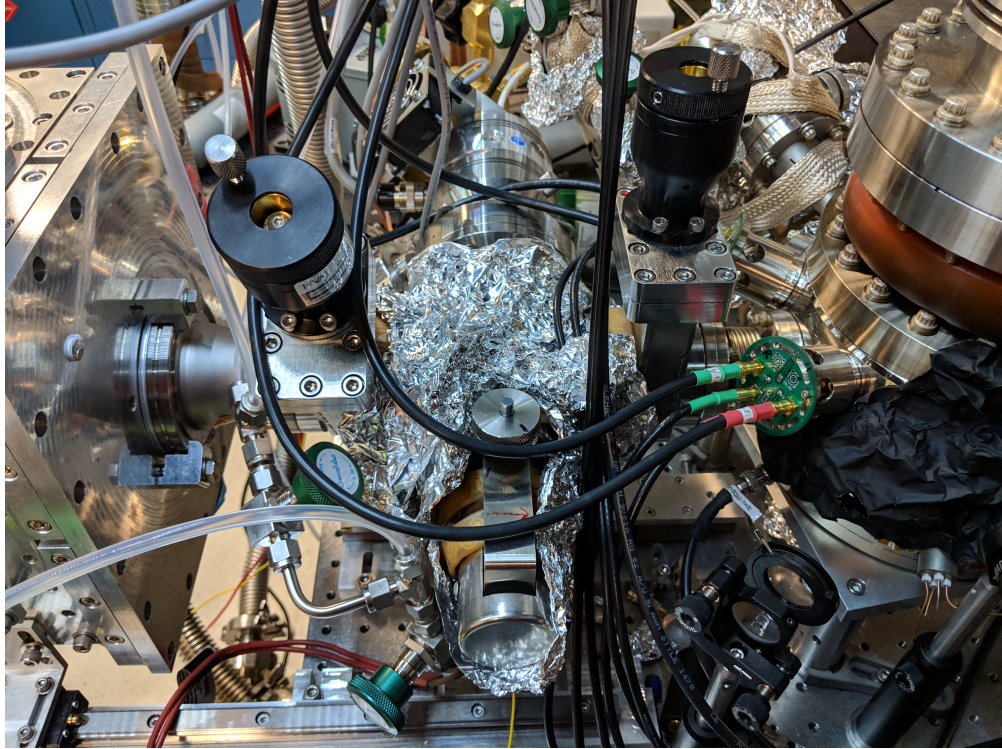


Figure 4.3: Differential pumping region in between the stem and ion trap chambers with gate valves on either end. Blank copper CF gaskets with apertures of 4 mm and 10 mm are placed towards the stem and ion chamber respectively to limit conductance of background gasses while allowing the cryogenic beam through. An Agilent Twistorr 84 FS turbo pump keeps the region at pressures around  $10^{-10}$  Torr and a leak valve allows for controlled introduction of secondary gasses.

### 4.3 ${}^9\text{Be}^+$ Laser Cooling

To reach the low reaction temperatures desired for our experiment, we need both a cold molecule source as well as a cold and controlled ion source. We may trap  $\text{Be}^+$  ions, but given the trap depth of 3 eV, the range of reaction temperatures is vast. Using laser cooling of translational modes of the ions on a closed transition allows us cool down the ion such that clouds and crystals form with temperatures not exceeding 500 mK.[50]

Our atom of choice is  ${}^9\text{Be}$ , which is the only stable isotope of beryllium with a nuclear spin of  $I = 3/2$ . Being an alkaline earth atom,  ${}^9\text{Be}$  has two valence electrons, and by stripping one off, we are left with an ion with a structure very similar to those of alkali atoms. The states of interest for our work are the  ${}^2\text{S}_{1/2}$  ground state and  ${}^2\text{P}_{3/2}$  excited state. In the ground state, the hyperfine splitting between the lower  $F = 2$  and  $F = 1$  manifolds is 1.25 GHz [??](#). Defining the cooling transition on the  ${}^2\text{P}_{3/2}$  state from the  $F = 2$  ground manifold allows one to access a stretch transition between the ground  $m_F = 2$  to excited  $m'_F = 3$  states with magnetic fields on the order of  $2 \times 10^{-5}$  T.[??](#) In principle, this scheme does not require any repumping out of the  $S$  orbital  $F = 1$  manifold. Our apparatus does not easily accommodate magnetic field coils necessary to resolve the hyperfine states, requiring repumping out of the  $F = 1$  manifold. Acousto-optic modulators (AOMs) driven at 400 MHz are used to bridge the 1.25 GHz hyperfine splitting.

Addressing the  ${}^2\text{S}_{1/2} \longrightarrow {}^2\text{P}_{3/2}$  transition is done with a Toptica TA-FHG Pro tuned to 313 nm with a peak power of 400 mW. The fundamental laser light is blue-detuned by 400 MHz from the cooling transition, which is then passed through a 400 MHz AOM to put it on resonance. The unperturbed, transmitted light, is then double passed through another 400 MHz AOM to repump the population that has fallen into the ground  $F = 1$  manifold as shown in figures [4.4](#) and [4.5](#). An additional AOM driven at 200 MHz creates red sidebands for both cooling and repump lights create our "re-cooling" beams aimed at cooling particularly hot  $\text{Be}^+$  ions produced after ablation that would otherwise be lost in A-ramping.

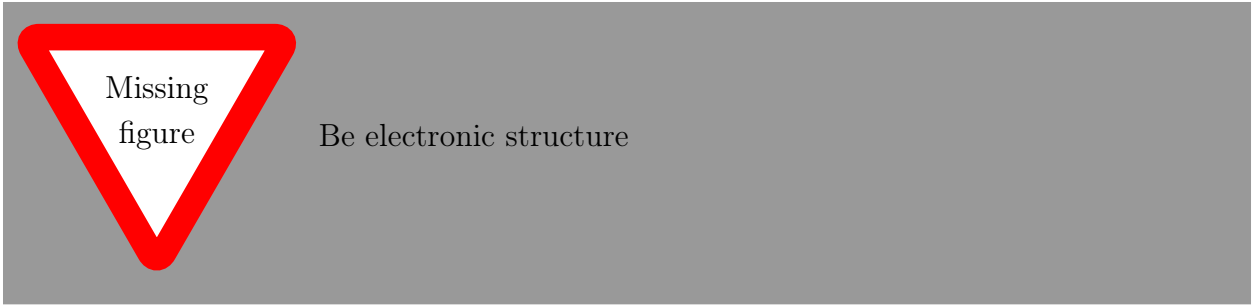


Figure 4.4: Electronic structure of  ${}^9\text{Be}^+$ , laser cooling is done with 313 nm light.



Figure 4.5: AOM's running at 400 MHz are used to tune the initially blue detuned primary beam on resonance with the  ${}^2\text{S}_{1/2}$  to  ${}^2\text{P}_{3/2}$  transition. A double passed AOM tunes the primary beam to the  ${}^2\text{S}_{3/2}$  to  ${}^2\text{P}_{3/2}$  transition to re-pump any  ${}^2\text{P}_{3/2} \longrightarrow {}^2\text{S}_{3/2}$  decays. A third AOM creates a first order beam 200 MHz red to aid the capture of hot ablated  $\text{Be}^+$  ions.

As we excite the cooling transition, force is being imparted onto the ion via absorption of the photons and spontaneous emission. We can define the force to be the product of the scattering rate of a two level system and the momentum of each photon.

$$\begin{aligned}
 F &= p\Gamma\rho_{pp} \\
 &= \hbar k\Gamma \frac{1}{2} \frac{s}{1 + s + 4 \left( \frac{\delta - \vec{k} \cdot \vec{v}}{\Gamma} \right)^2}
 \end{aligned} \tag{4.8}$$

Where  $k$  is the photon's wavenumber,  $\Gamma$  is the linewidth of the excited transition, and  $\rho_{pp}$  is the probability of finding the ion in the excited  ${}^2\text{P}_{3/2}$  state characterized by the saturation parameter  $s = I/I_s = I/(\frac{\pi hc}{3\lambda^3 \tau})$  and laser detuning  $\delta = \omega_0 - \omega_l$ . We can see that the force the ion feels is dependent on the laser detuning from resonance, which in turn is dependent on the doppler shift of the ion with respect to the laser  $\vec{k} \cdot \vec{v}$ . In general, the laser frequency ( $\omega_l$ ) is red detuned from the cooling transition ( $\omega_l < \omega_0$ ). In this instance, if the ion is moving towards the laser such that the velocity ( $v$ ) and  $k$  vector are anti-aligned, we see a positive doppler shift in the frequency ( $+kv$ ), decreasing the effective detuning, increasing the scattering rate. When the ion is moving away from the laser while  $\omega_l < \omega_0$  is true, we see that the detuning increases, lowering the scattering rate. Each time the ion absorbs a photon, it gains a momentum kick in the photon's direction, meaning the ion preferentially absorbs light that causes it to lose momentum. After absorption, the ion emits a photon after  $\tau = \Gamma^{-1}$  time, isotropically, which averages to zero. We can Taylor expand equation 4.8 for small values of  $v$  to find this velocity dependence.

$$F(v) = F(v = 0) + \beta v$$

Where we define the damping coefficient:

$$\beta = 4\hbar k^2 \frac{s \frac{\delta}{\Gamma}}{1 + s + 4 \left( \frac{\delta}{\Gamma} \right)^2}$$

Since the ion trap is not a perfect harmonic potential, which would require hyperbolic trap electrodes, the ion's trajectory is mixed along each axis, allowing for the 3 dimensional laser cooling with just one beam angled from both radial and axial axes of the trap.

## 4.4 Imaging System

Using the 313 nm laser, we fluoresce the  $\text{Be}^+$  ions and cool them down to a cloud or crystal in the ion trap. The scattered light is observed via our imaging system shown in figure 4.6. The components include the Andor iXon3 camera with EM gain, a 313 nm band pass filter,

angled mirror, enclosing lens tubes, and Sill objective lens with 0.2 NA, and 40 mm working distance. The alignment of our objective lens to camera imaging plane yields a magnification of about  $\times 5.5$ . All of the imaging components are rigidly mounted onto the 3 axis translation stage allowing us to move the focal point without changing the magnification.

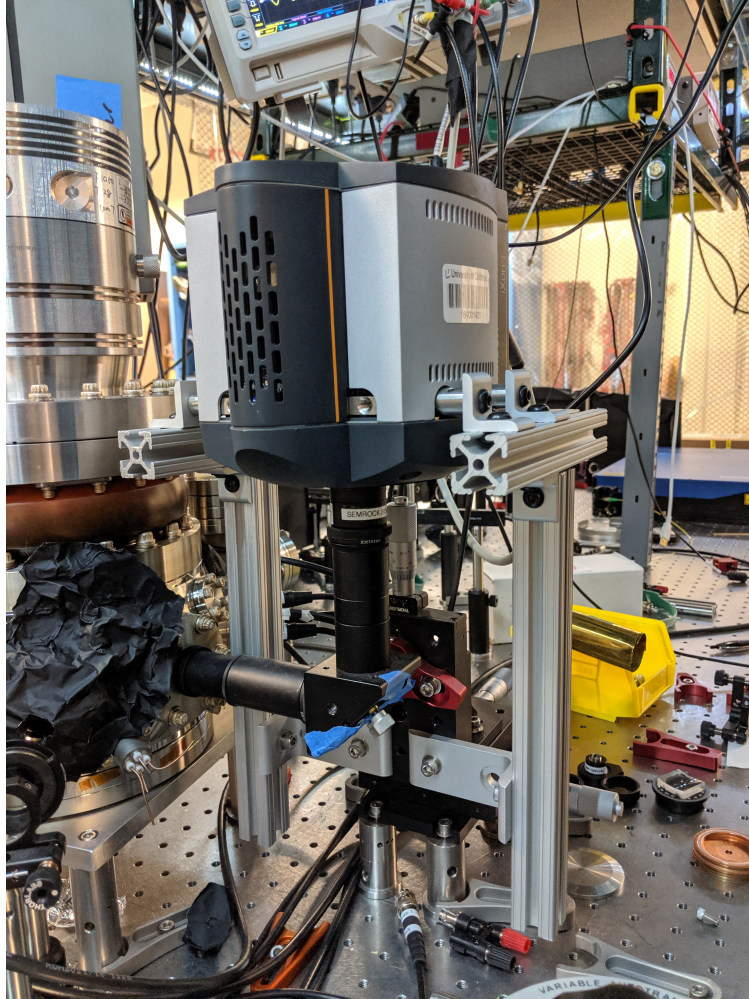


Figure 4.6: The iXon3 camera is mounted onto a 3 axis translation stage as well as the enclosed imaging pathway. The imaging tubes include the Sill objective lens at the end, inserted into the reentrant flange, an angled mirror, and a 313 nm bandpass filter placed at the camera input.

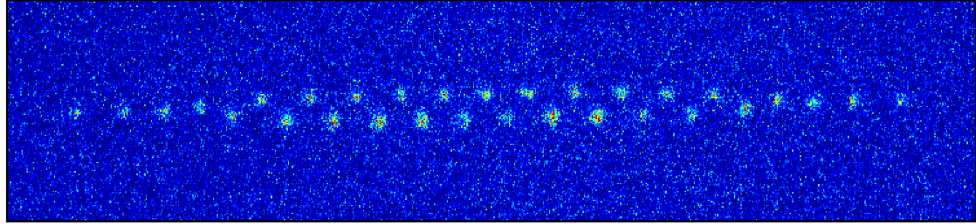


Figure 4.7: Laser cooled Coulomb crystal of  $\text{Be}^+$  ions in the LQT imaged with the reentrant imaging system.

The total efficiency of our imaging system is:

$$\epsilon = \Omega\alpha\beta\gamma \quad (4.9)$$

Where  $\Omega$  is the solid angle the reentrant objective appends,  $\alpha$  is the camera's quantum efficiency at 313 nm,  $\beta$  is the camera's exposure time, and  $\gamma$  is the camera's gain. For a fluorescing ion scattering at  $\Gamma \times (\rho_{pp} \approx 0.20)$ , we expect on the order of  $10^5$  counts per ion after the imaging inefficiencies.

## 4.5 Determining Excited State Population

Having a single ion in the trap while sweeping the frequency or power would be ideal to determine the saturation parameter, and thus the fraction of  $\text{Be}^+$  in the excited  ${}^2\text{P}_{3/2}$  state. But due to the size and depth of our ion trap, we cannot reliably load only one ion, nor can we guarantee there only being one ion. On top of that, the most common residual gasses in a vacuum chamber,  $\text{H}_2\text{O}$  and  $\text{H}_2$  both readily react with  $\text{Be}^+$  in the excited state limiting the available interrogation time. Instead of a continuous measurement, we analyze images of ion chains at various laser powers and find the fluorescence per ion to fit to a generalized form of the scatter rate ( $\Gamma_d$ ):

$$\begin{aligned}\Gamma_d &= a\rho_{pp} \\ &= \frac{a}{2} \frac{s}{1 + s + 4(\delta/\Gamma)^2}\end{aligned}\tag{4.10}$$

Where the parameter  $a$  consists of all the efficiency parameters in equation 4.9. To get the P-state fraction,  $\text{Be}^+$  ions are loaded into the trap and A-ramps are applied until a chain is formed and the laser detuning adjusted until we see maximum fluorescence on the camera, which coincides with a detuning of  $\Gamma/2$ . Then images of the ions are taken at various laser powers and run through a maximum filter algorithm to identify the locations of individual  $\text{Be}^+$  ions as seen in figure 4.8. The portion of the image not an ion is then averaged to obtain the background pixel value, which is then subtracted from each localized ion image. The pixel values over each localized ion is then summed to yield a total fluorescence value, which is then averaged for each image, as shown in figure 4.9. By performing a least squares fit on the collected fluorescence per ion as a function of incident power, we find the generalized efficiency  $a$ , revealing the P-state fraction at each power in  $\rho_{pp}$ , shown in figure 4.10.

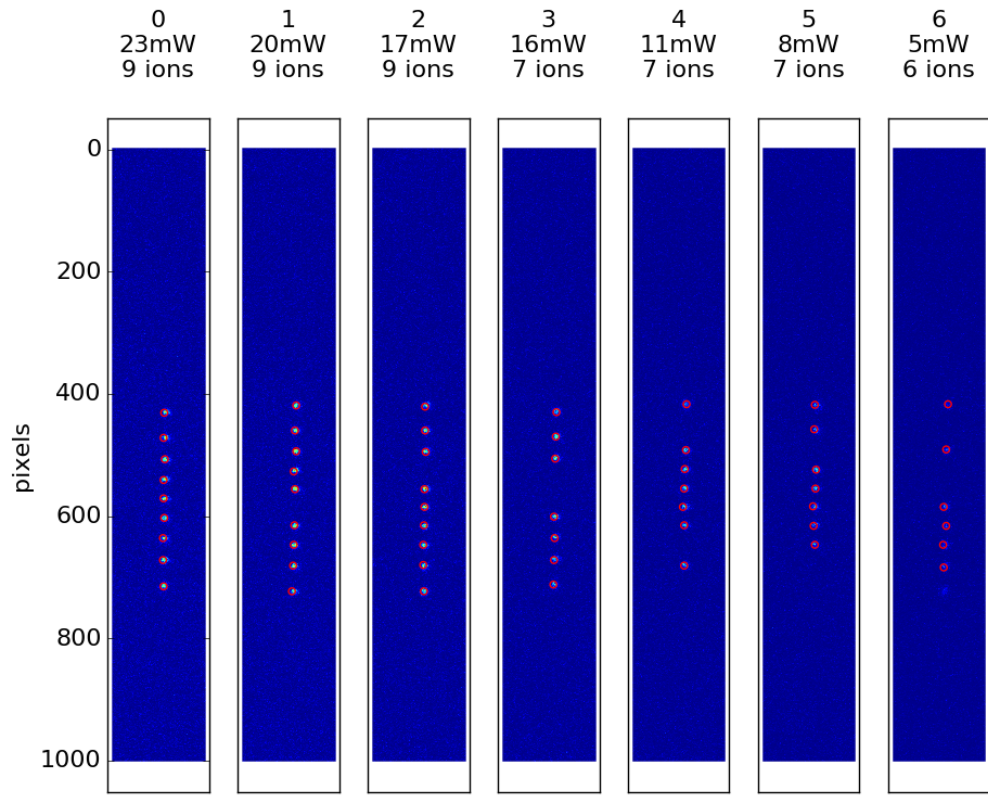


Figure 4.8: A set of ion images taken at various 313 nm powers run thorough a maximum filter algorithm that identifies local maxima, representing individual ions (circled in red). gaps in the ion chain are due to reactions with background H<sub>2</sub> producing BeH<sup>+</sup>, which occupy crystal sites without fluorescing.

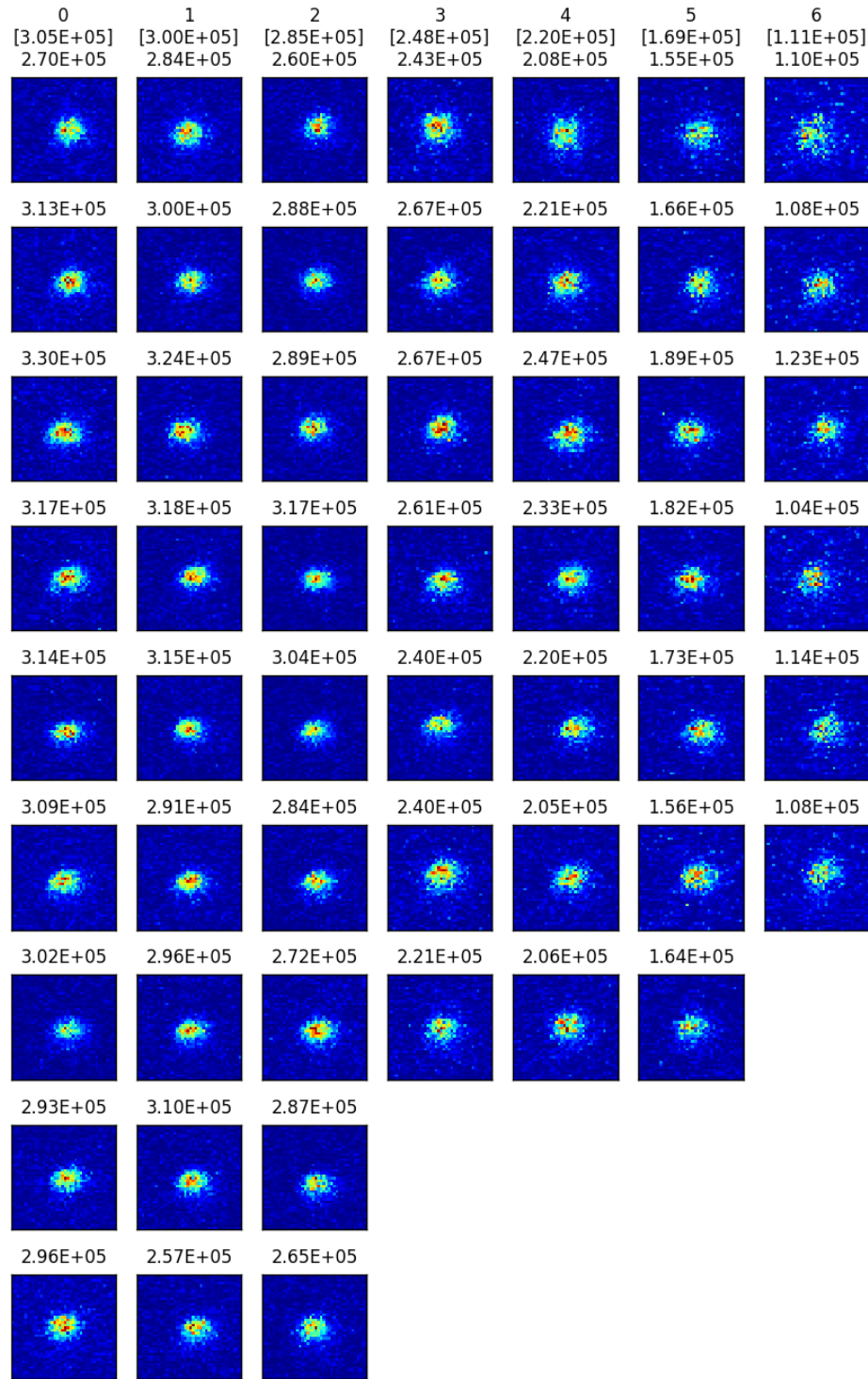


Figure 4.9: Individual ions identified from images in figure 4.8. Integrated pixel values with subtracted background counts shown for each image, a set's averaged value is shown in brackets.

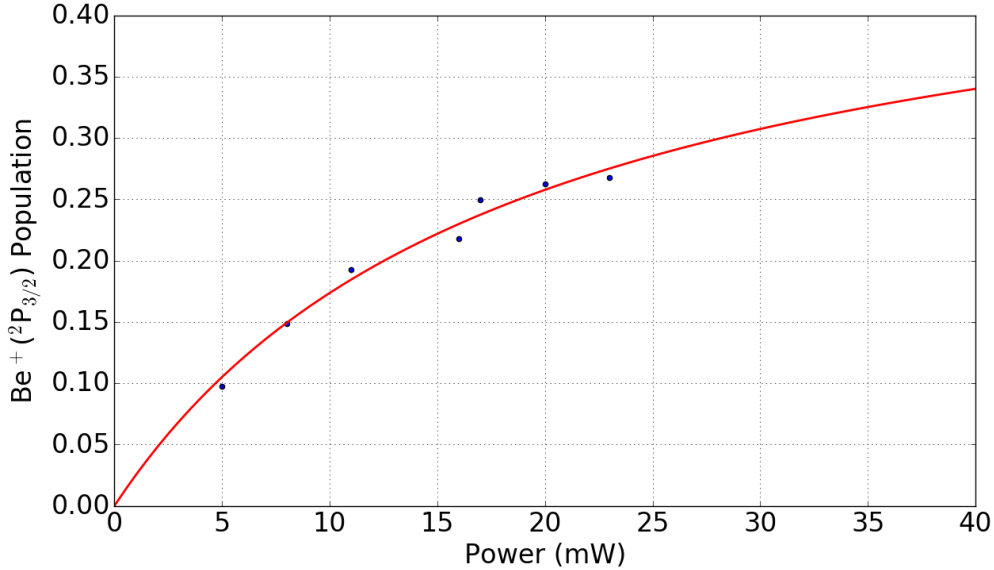


Figure 4.10: P-state fraction curve fitted to incident laser power at a fixed detuning of  $\delta = \Gamma/2$ . Total fluorescence value is normalized by fitted efficiency parameter  $a$  to yield  $\rho_{pp}$ .

## 4.6 Time of Flight Mass Spectrometer (TOF-MS)

One of the key components of this experiment is the fact that charged reaction products stay within the ion trap, allowing us to accumulate all stages of a reaction network. Direct identification of the species via fluorescence is ideal, as the signal is unambiguous, and generally unique to a species. Leaning on direct fluorescence becomes increasingly difficult as more and more species are introduced. In our particular case, it becomes prohibitively difficult, as we may expect to trap 10's of species at once, where in some cases, the exact reaction products are not known. To identify what is in our trap, we use a species agnostic detection method in the form of a time of flight mass spectrometer (TOF-MS).

The TOF works by switching the rod voltages from a trapping RF potential to one where the ions are ejected out of one side. When trapping, RF voltages are applied onto diagonal rods, while DC voltages on the others. During ejection, the trapping region turns into the acceleration region as adjacent pairs of rods ramp to constant voltages where the pair of "back" rods are at a higher potential than the pair of "front" rods seen in figure 4.11.

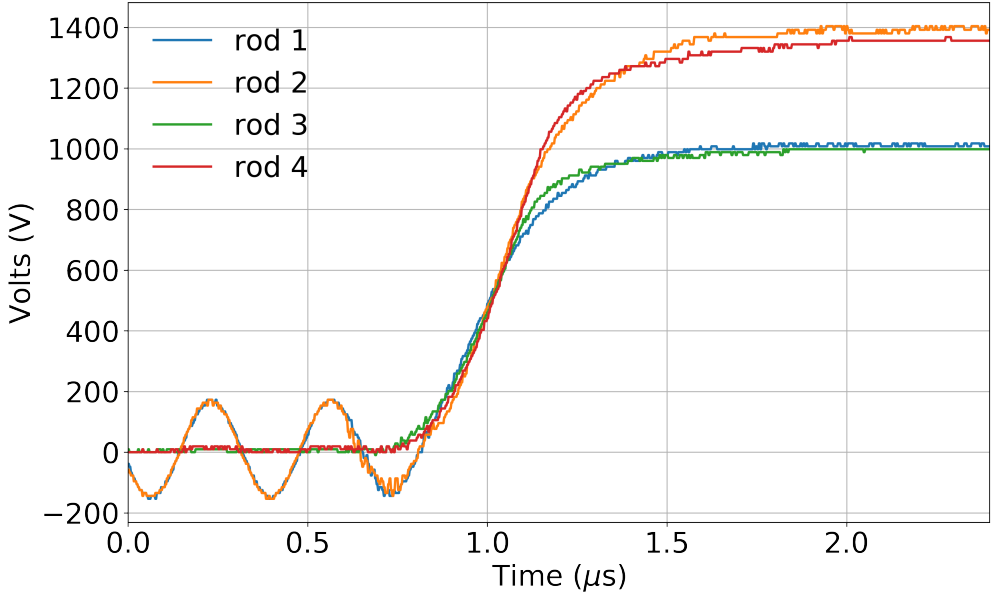


Figure 4.11: text

Ideally, during ejection the ions in the ion trap feel the same potential such that they are ejected radially. Since they are accelerated by the same potential, species of different masses are ejected at different velocities. The ions are then focused through Einzel lenses and travel down a drift tube and are detected on a micro-channel plate (MCP) which we read to record ion arrival times. To first order, the mass to charge ratio ( $m/z$ ) is then proportional to  $t^2$  where  $t$  is the arrival time, which is proportional to the drift tube length  $D$ . It may seem like greater mass separation is achieved with a longer drift tube, but that is not the case.

We made the assumption that the ions are accelerated by the same potential, but in reality, the ions occupy a finite spacial extent in which the potential felt by an ion is related to its location within the trapping region at the time of ejection. An ion in the center of the trap at the time of ejection will have a distance  $d_0$  to travel in the acceleration region, while those towards the back/front pair of rods will have distances  $d = d_0 \pm \delta d$ . As these ions fly down the drift tube, although the ions initially closer to the front have a shorter distance to travel, the ones originating further back have a higher velocity and will catch up and overtake the slower ions. This mismatch will cause the ion arrival times of a single species to

spread out as  $D$  increases past the point where all the ions overlap.

On top of considering the spacial extent of the ions in the trap, we must also consider the multiple acceleration regions. The rods that the trap consists of produce a fairly uniform electric field within the trap region  $E_d$ , but outside, there is still an accelerating electric field  $E_s$ , but primarily from the front rods. Accounting for all the possible components, we find that the drift tube length  $D$  can be parameterized by the other values.??

$$D = 2d_0 k_0^{3/2} \left( 1 - \frac{1}{k + \sqrt{k}} \right) \quad (4.11)$$

Where  $k = (E_s + E_d)/E_s$ . Our TOF apparatus design and electronics were extensively developed by Steven Schowalter and Christian Schneider of the Hudson group.[36, 35] The length  $D = 320$  mm long, and  $d_0 = 4.8$  mm.

#### 4.6.1 TOF Signal Integration

The MCP detector produces a current proportional to the number of ions that activate its surface, which is then read by a fast oscilloscope. An example TOF trace is shown in Figure 4.13 where we see that laser cooling of  $\text{Be}^+$  narrows the peaks of both  $\text{Be}^+$  as well as  $\text{C}^+$  such that the mass resolution  $m/\Delta m \approx 200$  for  $m/z$  values between 9 and 45. To determine the total number of ions, we integrate the current as a function of arrival time to find a total charge for each calibrated amu range (colored regions in Figure 4.13). A difficulty is determining whether or not an integrated peak corresponds to an ion, or simply noise. For each TOF trace, we find a region of high mass (e.g.  $m/z > 45$ ), where there aren't any ions and bin single amu chunks to produce a histogram. This histogram is then fitted to a Gaussian to determine the standard deviation, where then we may find a 90% confidence interval ( $\approx 1.3\sigma$ ). This value then defines our signal threshold, if an integrated signal is below this value, it is rejected and a zero is returned with error bars equal to this threshold, otherwise it is considered a true ion signal.

## 4.7 Dual Species Loading

Although loading and cooling Be<sup>+</sup> ions is fairly straight forward, it is not as clear as how to load C<sup>+</sup> ions into the trap with Be<sup>+</sup> reliably. Early attempts involved using the home-made electron gun to dissociate CO gas introduced via leak valve, where all possible ionized products of CO were detected (C<sup>+</sup>, O<sup>+</sup>, and CO<sup>+</sup>). Even when loading into an empty trap, it was not possible to reliably isolate the C<sup>+</sup> via A-ramping of the trap RF voltage. Prolonged use of the electron gun directly towards the ion trap also caused charging that would slowly dissipate and change the trap parameters. On top of these complications, it would not have worked in conjunction with ablation loading Be<sup>+</sup>, as these cannot occur simultaneously.

Instead of using two different methods to load the different ion species, ablating samples of both species simultaneously was found to be the best method. A sample of Be metal was placed on top of a piece of graphite on the target holder so that both samples were in view of the ablation laser. The set up shown in figure 4.12 allowed us to separate the Minilite ablation laser into two beam with independent alignment and focal planes. The polarization of the laser light is rotated with a half-waveplate, which then enters a polarizing beam splitter (PBS), allowing for tuning of power into either path. The vertically polarized reflected light is reflected off a second PBS and is steered up to the objective lens and then focused into the chamber. The horizontally polarized light transmitted through the first PBS is aligned through an adjustable telescope system. This light is then realigned with the vertically polarized light on the second PBS, co-propagating into the chamber. This "delay stage" for the horizontal light allows for independent focusing and alignment onto a target.

---

draw  
on  
fig-  
ure

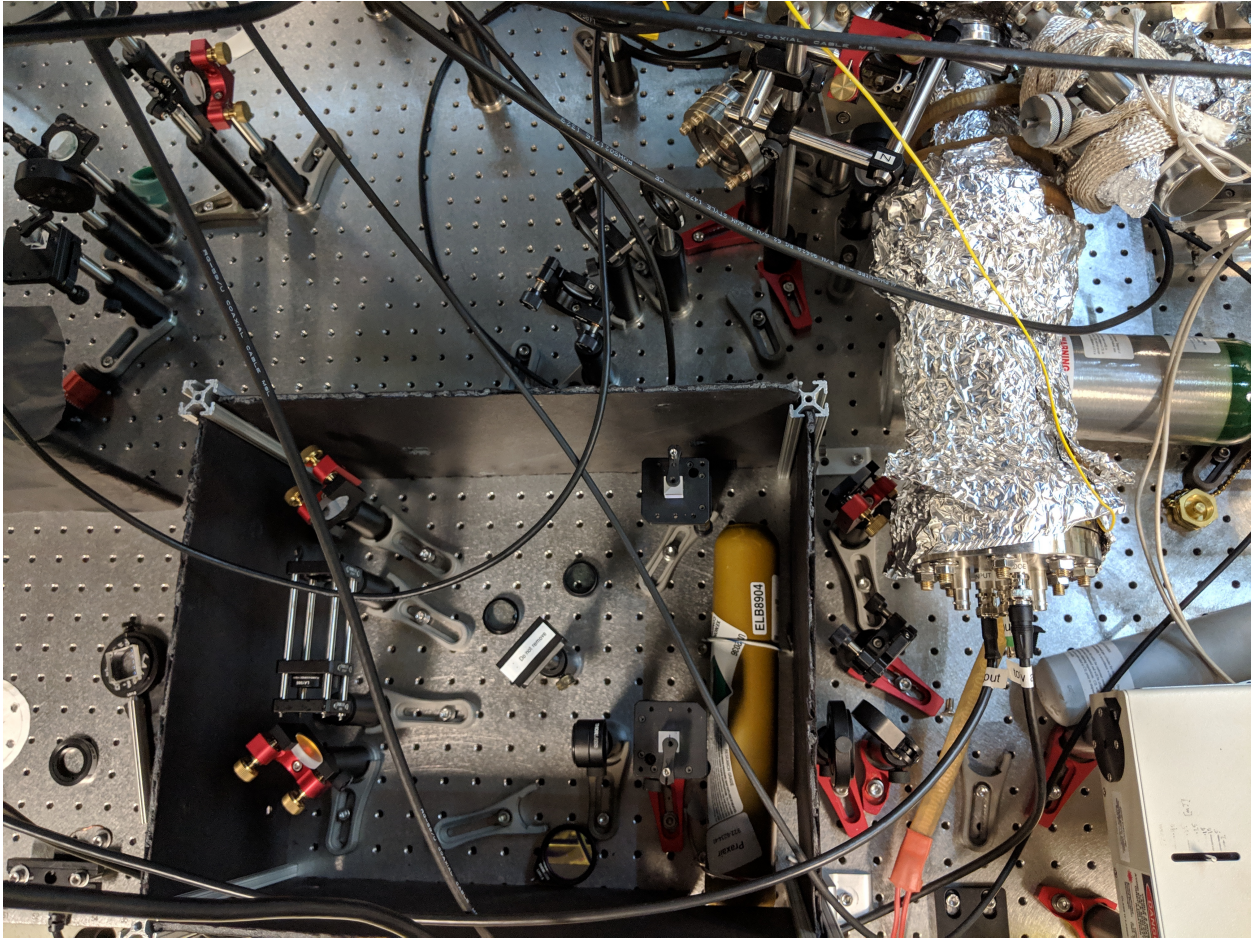


Figure 4.12: Image of the single laser, dual ablation set up. The 1064 nm YAG pulse is split into two paths, and recombined such that they proceed through the same focusing element into the chamber to hit two different targets.

Blocking one beam allowed for adjustments for the ablation of each species independently. When loading  $\text{C}^+$ , we found a strong dependence of the trapped species and the fluence. Lower fluence created not only  $\text{C}^+$ , but clusters of,  $\text{C}_2^+$ , and  $\text{C}_3^+$  as well. Tight focusing of the beam improves the efficiency of creating only  $\text{C}^+$ , but some  $\text{Cn}^+$  is still usually produced. By changing the trap's  $a$  parameter (A-ramp) via changing the  $V_{DC}$  (4.2), we can change the stability diagram for the trap, causing higher  $m/z$  ions to become more unstable. The higher mass  $\text{Cn}^+$  ions are preferentially kicked out of the trap, while the lighter  $\text{Be}^+$  and  $\text{C}^+$

are less affected, allowing us to load clean samples of the desired species.

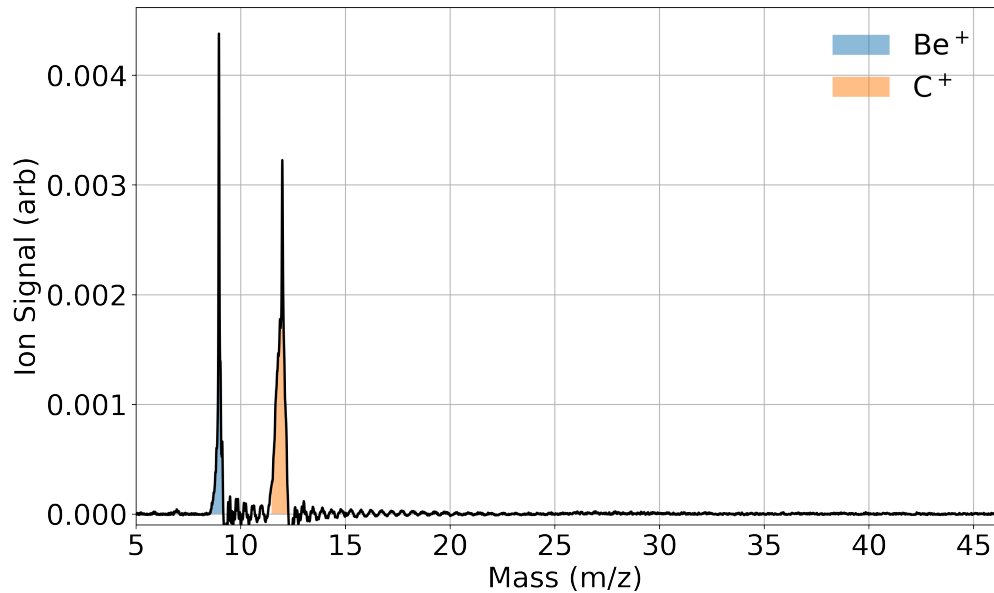
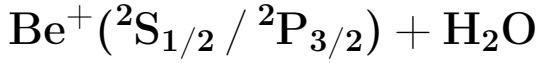


Figure 4.13: TOF trace of simultaneous  $\text{Be}^+$  and  $\text{C}^+$  ablation loading averaged over 10 shots. A soft A-ramp is applied after loading, ejecting any unintentionally loaded  $\text{C}_n^+$  clusters. The  $\text{C}^+$  peak is narrowed from sympathetic cooling with the laser cooled  $\text{Be}^+$  ions.

# CHAPTER 5



## 5.1 Optical Control of Reactions between Water and Laser-Cooled $\text{Be}^+$ Ions

### 5.1.1 Prologue

When exposing  $\text{Be}^+$  and  $\text{C}^+$  in the ion trap to  $\text{H}_2\text{O}$  vapor introduced from the leak valve, we found that the reaction  $\text{Be}^+ + \text{H}_2\text{O} \longrightarrow \text{BeOH}^+ + \text{H}$  occurs. Interestingly, it occurred at a slower rate than that of  $\text{C}^+ + \text{H}_2\text{O}$ , where by ADO, the rates should be nearly indistinguishable. Towards our goal of understanding  $\text{C}^+ + \text{H}_2\text{O}$ , we needed to understand the role that  $\text{Be}^+$  may have, as all of the charged reaction products will stay in the trap. Along the way, we gained a fuller understanding of the  $\text{Be}^+ + \text{H}_2\text{O}$  reaction, which proved to be an invaluable tool for subsequent studies. The rate constant was both experimentally and theoretically found to be excited state dependent, despite the fact that both reaction pathways are exothermic. Knowing this rate constant to a high degree of confidence allowed us to characterize the water density at the ion trap from the CBGB, which neither our RGA nor ion gauge could detect.

### 5.1.2 Introduction

Low-temperature reactions of simple ions with small molecules play a central role in astrochemical environments from interstellar clouds to cometary comae to planetary atmospheres, including that of Earth[2, 23]. The chemical evolution of interstellar molecular clouds ultimately yields the seedbed from which new stars and planets are born and the raw

materials from which life likely developed. A firm understanding of the reaction rates for a host of elementary ion-molecule reactions is essential to accurately model these environments these environments. Techniques such as selected ion flow tubes (SIFTs)[1], guided ion beams[3], and supersonic flows (CRESU)[38] have improved our empirical understanding of these processes; however, each has its own limitations.[41, 42] Theoretically, it has long been recognized that these ion-molecule reactions are often barrierless, and their rates are frequently described by capture models.[16] However, recent studies have revealed that dynamical features can sometimes prevail,[28, 25, 6] in which case statistical treatments may not be accurate.[18, 9] Therefore, new experimental and theoretical efforts are needed to accurately address ion-molecule chemistry. Furthermore, there have been very few experimental studies of gas-phase reactions between metal ions and water, especially at low temperature, despite their importance for metal ion chemistry in a range of environments.[19, 31, 49]

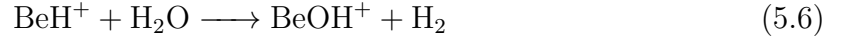
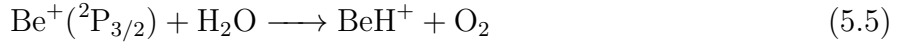
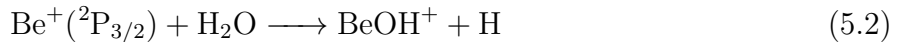
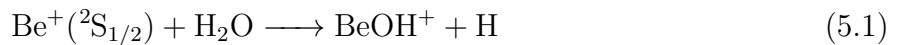
Singly ionized beryllium is a particularly attractive metallic reactant to use for such studies because it is both theoretically tractable and experimentally highly controllable. The relatively simple electronic structure of this three-electron ion allows both highly accurate characterization of its electronic structure and laser cooling,[4] and the low mass of  $\text{Be}^+$  lends itself to high motional frequencies as well as efficient sympathetic cooling of other chemically interesting atomic ions when employed in ion traps.[7, 34, 24, 37] For the molecular reaction partner,  $\text{H}_2\text{O}$  is arguably the most important molecule in chemistry, and theoretical studies of its reactions with a single atom have been reported on full-dimensional potential energy surfaces (PESs).[26, 43, 33, 27, 52] Thus this system of reagents provides an opportunity to perform a high-resolution comparison between experiments and theory for a molecule-ion system.

### 5.1.3 Experimental

To study the  $\text{Be}^+ + \text{H}_2\text{O}$  reaction,  $\text{Be}^+$  was loaded into the trap and cooled with the 313 nm laser, then exposed to  $\text{H}_2\text{O}$  vapor introduced from the leak valve.

To minimize experimental errors, a combination of fluorescence detection and TOF mea-

surements were used in tandem. Using both methods together, compared to only using the TOF, allows us to cut down the data collection time, which greatly reduces the effects of drifts in laser power and locking. The initial fluorescence signal determines the reaction time zero as well as normalize the initial ion number for the TOF traces. TOF traces are taken at various reaction times to determine the relative reaction product signals via shared fitting of solved differential equations including all possible reaction pathways shown in Figure 5.2. In total, we consider the following 8 reaction pathways, all of which are thermochemically allowed.



Typical TOF traces (10 sample average) at reaction times  $t = 0$  and 70 s with 7 and 26% relative  $\text{Be}^+(\text{^2P}_{3/2})$  state excitation are shown in Figure 1A,B, respectively. At  $t = 0$  s, a large peak of  $m/z = 9(\text{Be}^+)$  and a smaller one of  $m/z = 9(\text{BeOH}^+)$  are evidenced in the TOF trace (blue line), which indicates that  $\text{Be}^+$  ions are the main species in the trap at  $t = 0$ . The finite amount of  $\text{BeOH}^+$  at  $t = 0$  reflects the fact that reactions 5.1-5.8 happen even during the loading process and that the A-ramp mass filtering procedure is imperfect. At  $t = 70$  s, a  $m/z = 19$  peak emerges when more  $\text{Be}^+$  ions are excited to  $\text{^2P}_{3/2}$  state (figure 5.3), which we identify as  $\text{H}_3\text{O}^+$  resulting from reactions 5.3 and 5.4. The  $\text{BeOH}^+ / \text{H}_3\text{O}^+$  ratio,  $\eta(P_{\text{P}})$ , is measured by integrating both peaks for the experimentally controlled excited-state population  $P_{\text{P}}$ . The  $\text{BeOH}^+$  signal includes the amount unfiltered

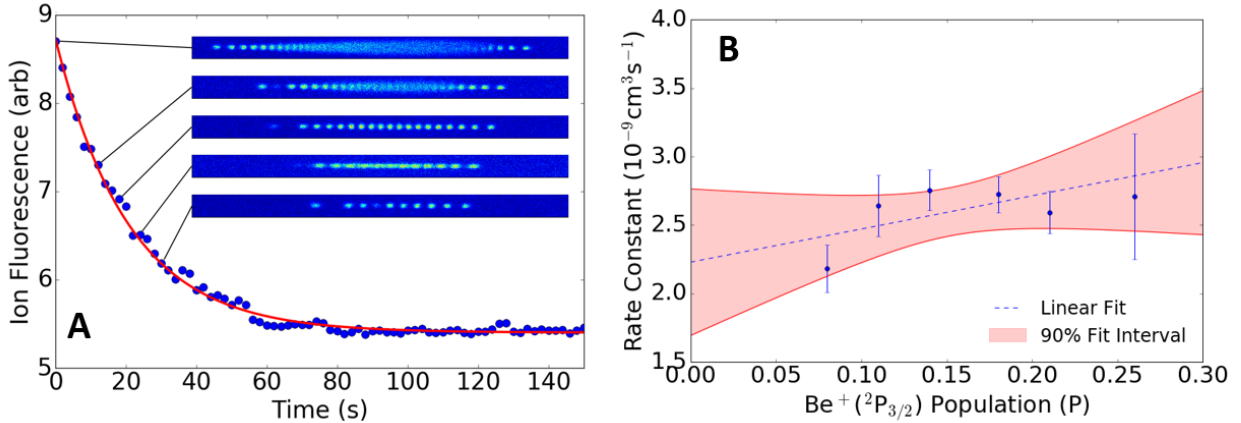


Figure 5.1: (A) Typical fluorescence decay measurement. The inset images are a subset of the original ion fluorescence images recorded by the camera. The red curve is an exponential fit (with a free offset) to the data, which gives the total reaction rate. (B) Total reaction rate coefficient as a function of  $\text{Be}^+ ({}^2\text{P}_{3/2})$  state population can be used to separate the contributions from the ground and excited states of  $\text{Be}^+$ .

during loading, products from both reactions 5.1 and 5.2, as well as, in principle, the two-step reactions 5.5, 5.6, 5.7, and 5.8. The  $\text{H}_3\text{O}^+$  signal is produced via the two-step reactions 5.3, 5.4. Whereas we do not observe products from reactions 5.5, 5.6, 5.7, or 5.8 (see Figure 5.2). They are thermochemically allowed and therefore included in our analysis, which sets upper limits on their reaction rate coefficients.

#### 5.1.4 Results and Discussion

The total reaction rate is given by  $\Gamma_t = \rho_{\text{H}_2\text{O}} k_t$ , where  $\rho_{\text{H}_2\text{O}}$  is the  $\text{H}_2\text{O}$  density measured the RGA calibrated to the ion gauge (section A) and  $k_t$  is approximated as  $k_t = P_S k_1 + P_P k_2 + P_P k_3$ , where  $P_S$  and  $P_P$  are the  $\text{Be}^+$  population in the  ${}^2\text{S}_{1/2}$  and  ${}^2\text{P}_{3/2}$  states, respectively, and  $k_i$  is the reaction rate coefficient of reaction  $i$ . Reaction eq. (5.4) has been studied by other groups, reporting a rate coefficient of  $(2.05 \pm 0.010) \times 10^{-9} \text{ cm}^3/\text{s}$ .[20] The measured

$\text{H}_3\text{O}^+ / \text{BeOH}^+$  ratio is given from the reaction rates by:

$$\eta(P_{\text{P}}) = \frac{P_{\text{P}}k_3}{P_{\text{S}}k_1 + P_{\text{P}}k_2} \quad (5.9)$$

To use equation 5.9 to extract the individual rate coefficients ( $k_i$ ), the total reaction rate  $\Gamma_t$  is first measured by monitoring the  $\text{Be}^+$  fluorescence decay with a camera, as shown in Figure 5.1A. Fluorescence decay is monitored directly after a DC voltage applied to trap electrodes is used to filter out the heavier products from the trap to allow better crystallization of the  $\text{Be}^+$  ions by reducing ion-ion heating.[8] The inset of Figure 5.1A shows typical fluorescence images of the  $\text{Be}^+$  coulomb crystal at various times. Fluorescence is used to measure the total reaction rate because the total measurement time is 30 times shorter than using the TOFMS (Figure 5.2). To determine the separate rate coefficients for the  $\text{Be}^+$  ground and excited states, we measure the total reaction rate coefficients for different excited-state fractions, shown in Figure 5.3. A linear fit (blue line) is found using the least-squares method. The vertical intercept of this fit gives the  $\text{Be}^+$  ground-state reaction rate coefficient  $k_{5.1} = (2.2 \pm 0.3_{\text{stat}}) \times 10^{-9} \text{ cm}^3/\text{s}$ , whereas the sum of the slope and intercept gives the total excited-state  $\text{Be}^+$  reaction rate coefficients  $k_{5.2} + k_{5.3} = (4.7 \pm 1.7_{\text{stat}}) \times 10^{-9} \text{ cm}^{-3}/\text{s}$ . Using equation 5.9, the reaction rate coefficients of reactions 5.2 and 5.3 are then calculated to be  $k_{5.2} = (4.2 \pm 1.6_{\text{stat}}) \times 10^{-9} \text{ cm}^{-3}/\text{s}$  and  $k_{5.3} = (0.47 \pm 0.11_{\text{stat}}) \times 10^{-9} \text{ cm}^{-3}/\text{s}$ , respectively. The ratio of reaction rate coefficients for reactions 5.3 to 5.2 is therefore  $k_{5.3}/k_{5.2} = 0.11 \pm 0.03$  independent of systematic errors in the density measurement. Charged products from reactions 5.5 and 5.7 are not directly observed and an upper bound is found to be  $< 5 \times 10^{-10} \text{ cm}^3/\text{s}$ , set by the integrated signal threshold. Reactions at these upper bounds for the rate coefficients do not significantly change the analysis above, justifying their exclusion from  $k_i$ .

It is instructive to compare these measured rate coefficients to those predicted by capture theory. Since the translational energy of the laser-cooled  $\text{Be}^+$  ions is  $< 0.5 \text{ K}$ , the energy of the room-temperature water sets the reaction kinetic energy of  $\text{Be}^+ + \text{H}_2\text{O}$  in the center of mass frame of 100K. The internal state distribution of the  $\text{H}_2\text{O}$  is assumed to be given

by the 300 K. The internal state distribution of the H<sub>2</sub>O is assumed to be given by the 300 K. Because H<sub>2</sub>O has a dipole, we use the ADO theory (equation 2.19) to estimate the rate constant. The ADO model predicts that both the ground and excited Be<sup>+</sup> states react with a rate coefficient  $k_{ADO} = 4.1 \times 10^{-9}$  cm<sup>3</sup>/s at 100 K reaction temperature, roughly two times larger than measured for the ground state, but in agreement with the measured reaction rate of the excited state. Since the experimental rate constant agrees well with the theoretical rate, we may generalize 5.1 and 5.2 to:

$$k_{5.2+5.1}(T) \approx ((0.54)k_{ADO}(P) + (0.49)k_{ADO}) \times 10^{-9} \text{ cm}^3/\text{s} \quad (5.10)$$

However, because it is long-range, the ADO model cannot provide the branching ratio and state-dependent information and is therefore insufficient for describing the observed reactions. Hua Guo at UNM helped us in making theoretical calculations on the reaction dynamics by method of Quasi-Classical Trajectory Calculations (QCT-Calculations) on a full-dimensional potential energy surface (PES).[53] They calculate that the intermediate state (IM1) in Figure 5.4 on the ground state reaction pathway causes about 46% of the incoming trajectories to reflect back to the entrance channel yielding a rate constant  $k_{5.1th} = (2.02 \pm 0.04) \times 10^{-9}$  cm<sup>3</sup>/s. The excited state pathway does not have a submerged barrier of this level, but does have a nonadiabatic transition bringing it down to the ground state product channel.

### 5.1.5 Conclusion

In short, chemical reactions of laser-cooled Be<sup>+</sup> ions with room-temperature water vapor have been studied experimentally and theoretically for the first time. Ground-state Be<sup>+</sup> ions produce only BeOH<sup>+</sup> + H with a reaction rate coefficient of  $k_{5.1} = (2.2 \pm 0.3_{\text{stat}}) \times 10^{-9}$  cm<sup>2</sup>/s, whereas the excited-state Be<sup>+</sup> not only creates BeOH<sup>+</sup> + H with a reaction rate coefficient of  $k_{5.2} = (4.2 \pm 1.6_{\text{stat}}) \times 10^{-9}$  cm<sup>3</sup>/s but also gives H<sub>2</sub>O<sup>+</sup> + Be with a reaction rate of  $k_{5.3} = (0.47 \pm 0.11_{\text{stat}}) \times 10^{-9}$  cm<sup>3</sup>/s. Electronic structure calculations indicate that these two products are both produced via nonadiabatic pathways. The ground-state reaction rate

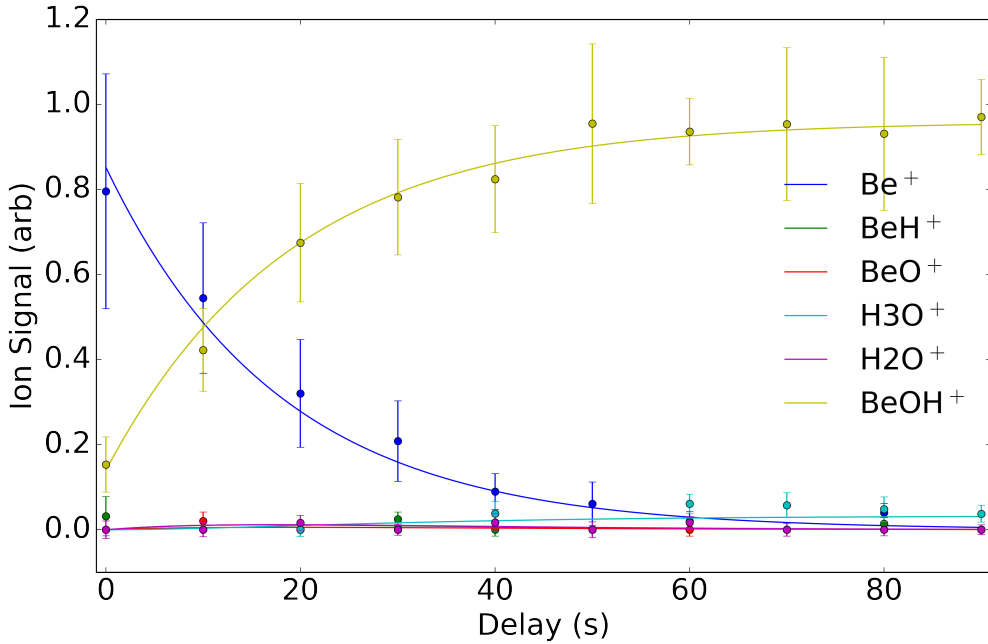


Figure 5.2: The temporal evolution of  $\text{Be}^+$  in the trap as a function of reaction time as well as the solutions of differential equations fitted to the kinetics data with  $P_{\text{P}} = 26\%$ .

is roughly half of that predicted by typically employed capture models but in good agreement with zero-point-corrected QCT calculations on an accurate full-dimensional global PES based on high-level ab initio calculations. These calculations reveal that the lower reaction rate is a consequence of chemical dynamics due to a submerged barrier in the product channel.

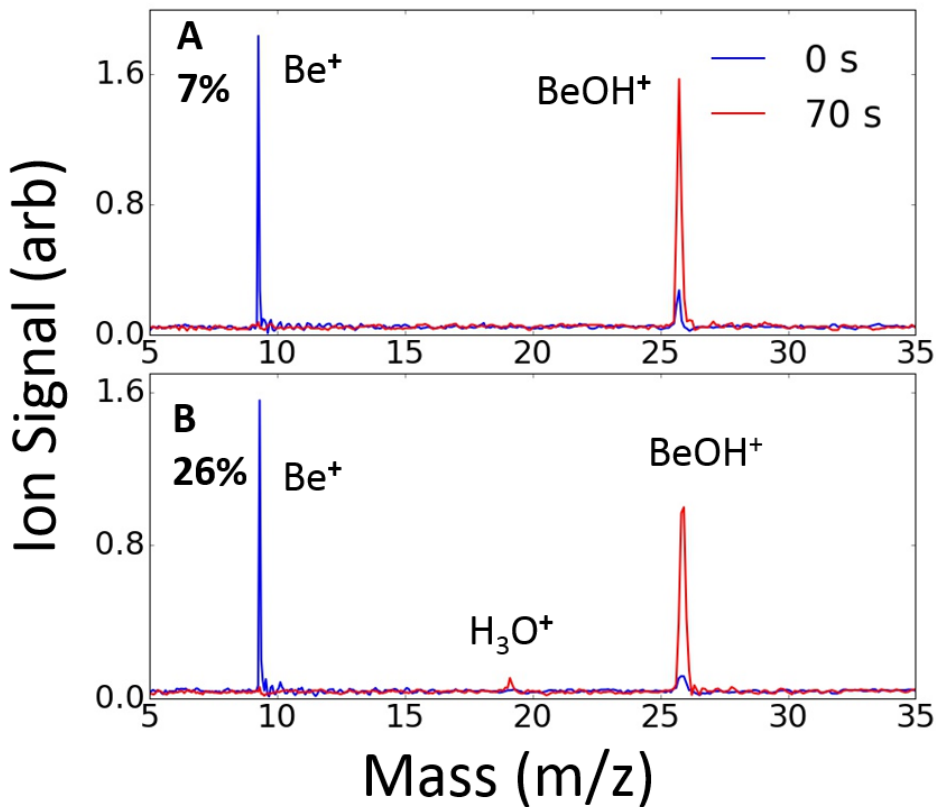


Figure 5.3: TOF signal (averaged over 10 trials) at reaction time  $t = 0$  and 70 s with (A)  $P_{\text{P}} = 7\%$  (A) and (B)  $P_{\text{P}} = 26\%$ . A clear  $m/z = 19$  peak emerges when more  $\text{Be}^+$  ions are excited to  ${}^2\text{P}_{3/2}$  state. The  $\text{BeOH}^+ / \text{H}_3\text{O}^+$  ratio for this case ( $P_{\text{P}} = 26\%$ ) is measured to be  $\eta(0.26) = 0.039 \pm 0.006$  by integrating both peaks in B when  $t = 70$  s.

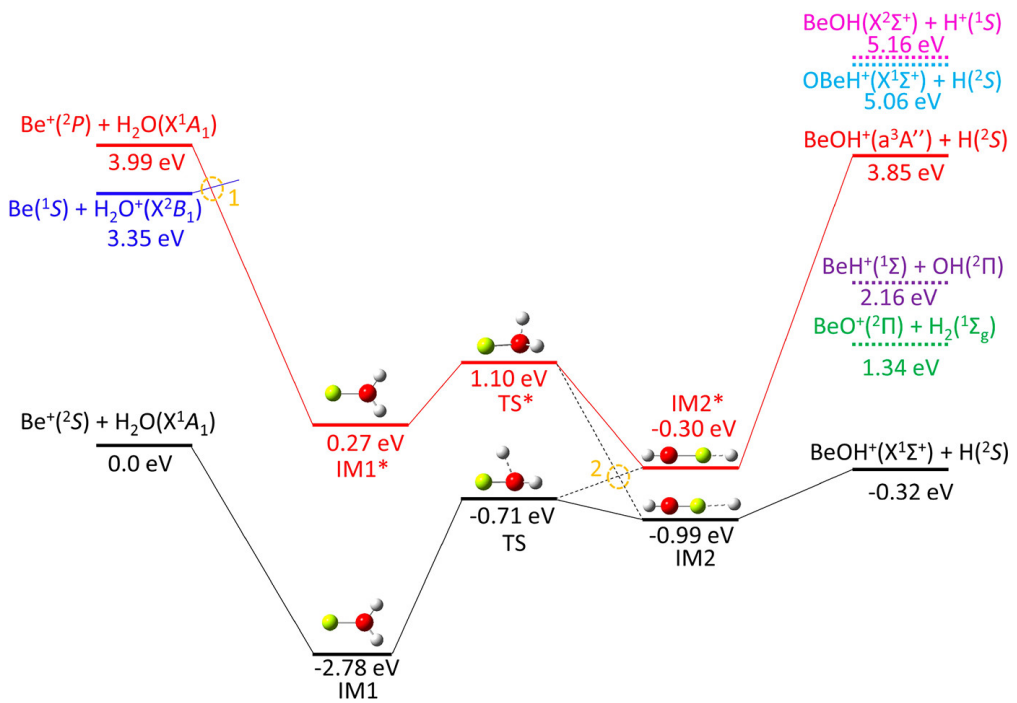


Figure 5.4: Energetics of both the ground- and excited-state reaction pathways for the  $\text{Be}^+ + \text{H}_2\text{O}$  reaction. Whereas reaction 5.1 proceeds on a single adiabatic PES, the reactions involving excited  $\text{Be}^+$  depend on nonadiabatic transitions between different PESs (yellow circles). The submerged well on the ground-state reaction pathway prevents 46% of the trajectories to reflect back to the entrance channel. (Taken from [53])

# CHAPTER 6



## 6.1 Isotope-selective chemistry in the $\text{Be}^+(\text{^2S}_{1/2}) + \text{HOD} \rightarrow \text{BeOD}^+/\text{BeOH}^+$ + H/D reaction

After finishing the work on the  $\text{Be}^+ + \text{H}_2\text{O}$  reaction, we turned our attention to focus more on branching ratios. Getting rate constants was troublesome given the requirement of having an absolute pressure measurement, while branching ratios measurements can be obtained through a single TOF trace. With our fuller understanding of the  $\text{Be}^+ + \text{H}_2\text{O}$  reaction network, we focused on reaction 5.1, for Hua Guo's group at UNM had calculated a full ground state PES. To capitalize on this, we turned to the question of whether or not there are dynamics hidden in the reaction pathway that can be seen via deuteration of  $\text{H}_2\text{O}$ . This proved to be a long process in its own right. Water is notoriously sticky inside vacuum chambers and to have a reliable reading on the isotopologue ratio, or to simply push this ratio towards more H or D, required weeks of data collection. At the end, we found what is an expected result, that the branching fractions follows statistical state counting with a (0.58:0.42), ( $\text{BeOD}^+:\text{BeOH}^+$ ) ratio.

## 6.2 Introduction

Together, isotope substitution and the measurement of the resulting product branching ratios provide important details about reaction dynamics and are often used to identify reaction pathways and understand bond-selective chemistry.[?, 10, 54] Important examples include X + HOD (X = H, F, Cl, O) reactions, where the branching ratios are experimentally controlled

by selective excitation of the O–H or O–D bond.[39, 5, 29, 55, 43, 44, 15, 57, 40] It is now understood that a highly-accurate potential energy surface (PES) is crucial for performing theoretical calculations of the product branching ratio, where subtle, difficult to identify, PES features have been found to significantly affect the results.[40]

A sophisticated understanding of radical-molecule reaction dynamics is continuing to develop from extensive experimental and theoretical studies. However, despite their importance in interstellar chemistry, where the isotopic branching ratios strongly influence the products of the interstellar cloud chemical network,far less progress has been made in the study of ion–molecule reactions at low temperature. This is largely due to the challenges associated with both the experimental and theoretical approaches to these systems.[9, 12, 1, 3, 38, 41, 42] Experimental difficulties include a lack of quantum state preparation and readout techniques, while theoretical difficulties appear when treating dynamics dominated by the long range interaction between ions and molecules. Recently, several groups have employed cold ( $\approx$ mK) and fully-controlled laser-cooled trapped ions to address these experimental issues. For instance, isotope selectivity was probed in the reaction of laser-cooled Mg $^{+}$  with HD,and the formation rate of MgD $^{+}$  was found to be 5 times greater than MgH $^{+}$ . This observation was ascribed to a dynamic mechanism in the exit channel of the reaction since statistical methods predict only a factor of approximately 2.[11] A similar experimental technique was applied to Ca $^{+}$  + HD reactions as well,[17] where the CaD $^{+}$  channel was found to have 1.5 times higher population than the CaH $^{+}$  channel; no detailed theoretical calculations have been performed for this system. With the help of laser-cooled ions, the initial quantum states are experimentally well controlled, but highly accurate PESs are still challenging to calculate with Mg $^{+}$  or Ca $^{+}$  ions due to the complexity of their electronic structures. The development of a more comprehensive understanding of ion–molecule reactions at low temperature will benefit from studies with less complex species that are amenable to theoretical treatment.

We build off the work done on the Be $^{+}$  + H<sub>2</sub>O reaction, which showed that dynamics resulting from a submerged barrier strongly affects the reaction, leading to a reduction of the overall reaction rate from the ADO capture limit. The overestimation by the capture

model was thus taken as a sign that this reaction is not completely statistical, despite the existence of a deep  $\text{BeH}_2\text{O}^+$  potential well along the reaction path. In this work, we probe the dynamics by examining the product branching ratio, which is presumably controlled by the exit channel barriers. Such a measurement is much more sensitive to the determination of the overall rates.

### 6.3 Experimental

Similar to the  $\text{Be}^+ + \text{H}_2\text{O}$  work, we load  $\text{Be}^+$  into the trap and laser cool it to create Coulomb crystals. A combination of  $\text{H}_2\text{O}/\text{HOD}/\text{D}_2\text{O}$  is introduced into the chamber via leak valve, where the reaction products are detected via the TOF. To produce HOD, we mix  $\text{H}_2\text{O}$  and  $\text{D}_2\text{O}$ .[?, ?] We mix "equal" amounts of  $\text{H}_2\text{O}$  and  $\text{D}_2\text{O}$  and leave it overnight to produce roughly 1:2:1 ratio of  $\text{H}_2\text{O}:\text{HOD}:\text{D}_2\text{O}$  as roughly verified by the RGA. We measure these fractions of deuterations via the RGA. A typical scan reveals water fractionation products at  $m/z = 18, 17$ , and  $16$ , which coincide with  $\text{H}_2\text{O}^+$ ,  $\text{OH}^+$ , and  $\text{O}^+$ . The fractionation ratios of water are found by solving the system of equations:

$$P_{\text{H}_2\text{O}} = R_{18} + R_{17} + R_{16} \quad (6.1)$$

$$R_{18} = \alpha P_{\text{H}_2\text{O}} \quad (6.2)$$

$$R_{17} = \beta P_{\text{H}_2\text{O}} \quad (6.3)$$

$$R_{16} = \gamma P_{\text{H}_2\text{O}} \quad (6.4)$$

where  $R_i$  is the pressure reading from the RGA and  $P_{\text{H}_2\text{O}}$  is the true  $\text{H}_2\text{O}$  pressure. These fragmentation ratios were found to be  $\alpha = 0.768 \pm 0.006$ ,  $\beta = 0.184 \pm 0.006$  and  $\gamma = 0.068 \pm 0.002$ . The direct readings from analog scans with deuterated samples were then adjusted to account for the fractionation for each isotopologue.

$$P_{\text{H}_2\text{O}} = \frac{1}{\alpha} \left( R_{18} - \frac{\beta}{\alpha} R_{20} - \frac{\beta}{2\alpha} R_{19} \right) \quad (6.5)$$

$$P_{\text{HOD}} = \frac{R_{19}}{\alpha} \quad (6.6)$$

$$P_{\text{D}_2\text{O}} = \frac{R_{20}}{\alpha} \quad (6.7)$$

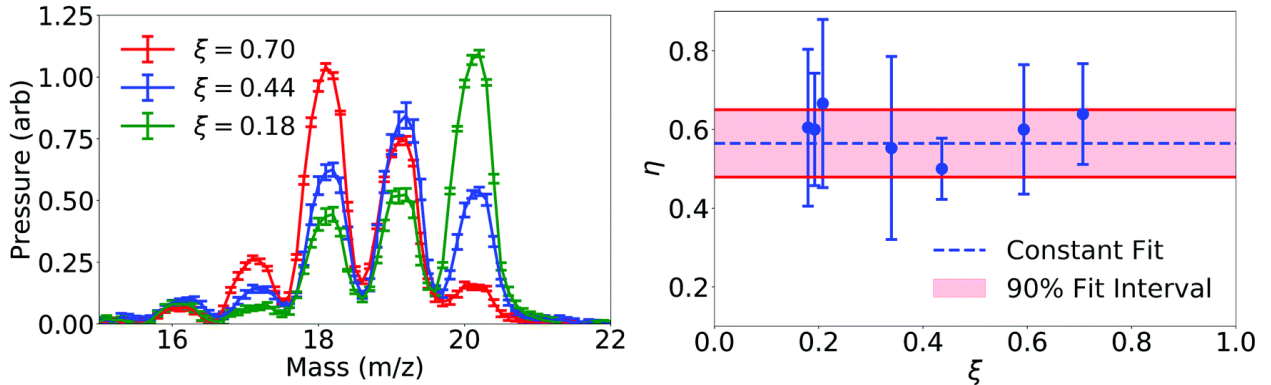


Figure 6.2: (left) Averaged (8 traces) RGA analog scan showing peaks at each isotopologue  $m/z$ . Points around the peak of each isotopologue were averaged for a more accurate partial pressure. (right) The branching ratio  $\eta$  of the reaction  $\text{Be}^+ + \text{HOD}$  into  $\text{BeOD}^+ + \text{H}$  (with a  $\text{Be}^+$  P-state fraction of  $P_P \approx 2\%$ ) as a function of initial H fraction in an HOD, H<sub>2</sub>O, D<sub>2</sub>O mixture. Shared fitting the branching ratio  $\eta$  with a constant value fit is shown with a weighted average of  $\eta = 0.58 \pm 0.14$ .

## 6.4 Results and Discussion

Because the HOD sample also contains both H<sub>2</sub>O and D<sub>2</sub>O, the product BeOH<sup>+</sup> ( $m/z = 26$ ) has contributions of the reaction of the cation with H<sub>2</sub>O, while BeOD<sup>+</sup> ( $m/z = 27$ ) has contributions from reactions with D<sub>2</sub>O. The reactions of interest are:

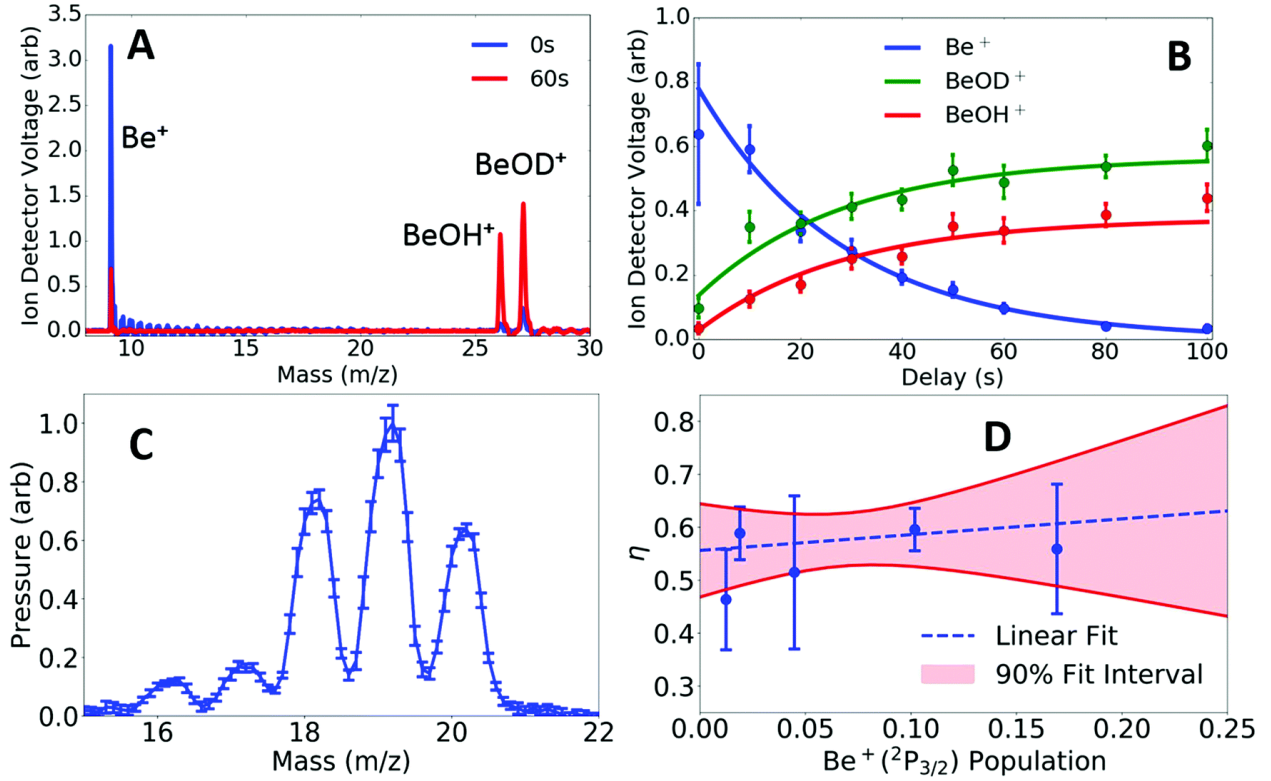
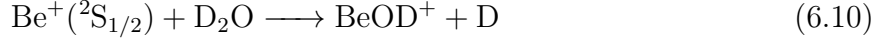
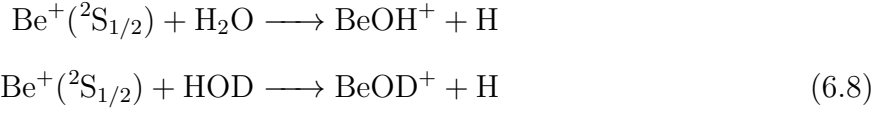


Figure 6.1: (A) A typical TOF signal (5 sample average) at reaction time  $t = 0\text{ s}$  and  $60\text{ s}$  with  $P_{\text{P}} \approx 2\%$ . (B) The temporal evolution of  $\text{Be}^+$ ,  $\text{BeOH}^+$ , and  $\text{BeOD}^+$  in the trap as a function of reaction time, as well as the solutions of differential equations fitted to the kinetics data with  $P_{\text{P}} \approx 2\%$ . (C) The RGA signal (8 traces average) gives relative initial  $\text{H}_2\text{O}$ ,  $\text{HOD}$ ,  $\text{D}_2\text{O}$  sample ratio, which is  $\rho_1 : \rho_2 : \rho_3 = (1.00 \pm 0.02) : (2.45 \pm 0.05) : (1.58 \pm 0.02)$ . (D) The product fraction for  $\text{BeOD}^+$  production ( $\eta$ ) of reactions (6.8 and 6.9) as a function of  $\text{Be}^+(^{2}\text{P}_{3/2})$  state population. The S-state branching ratio is found to be  $\eta_s = 0.56 \pm 0.03$ , in agreement with the following calculated combined value with different initial H fractions.



Thus, the differential forms and solutions of the reagents and products are solved and shown in ???. The branching ratio  $\eta \equiv k_{\text{BeOD}^+}/(k_{\text{BeOD}^+} + k_{\text{BeOH}^+})$  is the fraction of  $\text{BeOD}^+$  produced from reactions (6.8) where  $k_j$  is the rate coefficient of species  $j$ . Solutions to the rate equations B.13, B.14, and B.17 are parameterized by the density measurements of the water isotopologues taken from a RGA, and a least-squares fit is taken over data sets of integrated TOF mass spectra with shared fitting parameters  $k_1$ ,  $k_2$ ,  $k_3$ , and  $\eta$ . In order to extract the pure  $\text{Be}^+(\text{^2S}_{1/2})$  and  $\text{Be}^+(\text{^2P}_{3/2})$ -state branching ratios, the process shown in Figure ??(A)–(C) was repeated at different P-state fractions. The results are shown in Fig. 1(D) along with a least-squares linear-fit (blue line). The vertical intercept of this fit gives  $\eta_S = 0.56 \pm 0.03$  for the ground  $\text{Be}^+(\text{^2S}_{1/2})$  state reaction, while no conclusive dependence on P-state fractions is found within the confidence intervals. To further verify that our measurement is independent of reagent ratios, we repeated the measurement for different mixtures of HOD,  $\text{H}_2\text{O}$ , and  $\text{D}_2\text{O}$ , as shown in Fig. 3. The branching ratio of  $\text{BeOD}^+ + \text{H}$  in reaction  $\text{Be}^+ + \text{HOD}$  (with 2%  $\text{Be}^+(\text{^2P}_{3/2})$  state population) is consistent over different hydrogen fractions in the gas. The fraction of hydrogen atoms in the chamber ( $\xi$ ) from all water isotopologues is defined by:

$$\xi = \frac{2\rho_{\text{H}_2\text{O}} + \rho_{\text{HOD}}}{\rho_{\text{H}_2\text{O}} + \rho_{\text{HOD}} + \rho_{\text{D}_2\text{O}}} \quad (6.11)$$

Weighted averaging of the fitted values over different mixtures then gives  $\eta = 0.58 \pm 0.14$ ,  $frack_2k_1 = 0.8 \pm 0.9$ ,  $\frac{k_3}{k_1} = 0.8 \pm 0.9$ . Despite the large error bars on the relative rate coefficients, due to the significant covariance of the rate coefficients,  $\eta$  is reasonably well determined. To further check our measurement of  $\eta$ , the process was repeated for shared fits

with identical rate coefficients ( $k_1 = k_2 = k_3$ ) yielding  $\eta = 0.57 \pm 0.07$ . The calculated overall rate coefficients of the  $\text{Be}^+ + \text{D}_2\text{O}$  and  $\text{Be}^+ + \text{HOD}$  reactions are  $(2.29 \pm 0.05) \times 10^{-9} \text{ cm}^3 \text{ molecule}^{-1} \text{ s}^{-1}$  and  $(2.29 \pm 0.05) \times 10^{-9} \text{ cm}^3 \text{ molecule}^{-1} \text{ s}^{-1}$ , respectively, which are slightly larger than that  $((2.02 \pm 0.04) \times 10^{-9} \text{ cm}^3 \text{ molecule}^{-1} \text{ s}^{-1})^{25}$  of the  $\text{Be}^+ + \text{H}_2\text{O}$  reaction. The calculated  $k_2/k_1$  and  $k_3/k_1$  ratios are  $1.13 \pm 0.04$  and  $1.13 \pm 0.04$ , which are consistent with experimental values of  $0.8 \pm 0.9$  and  $0.8 \pm 0.9$ , respectively. The identical  $k_2/k_1$  and  $k_3/k_1$  ratios suggests the negligible isotopic effect in the thermal reaction probabilities of the  $\text{Be}^+ + \text{D}_2\text{O}$  and  $\text{Be}^+ + \text{HOD}$  reactions. The branching ratio was determined using the QCT method for the  $\text{Be}^+ + \text{HOD}$  reaction. Specifically, the calculated branching fraction of  $\text{Be}^+ + \text{HOD}$  ( $\eta$ ) is  $0.61 \pm 0.02$ , which is in good agreement with experimental value  $0.58 \pm 0.14$ . The branching ratio of the two products ( $\text{BeOD}^+$  and  $\text{BeOH}^+$ ) can be understood in terms of the PST model, which assumes complete energy randomization in the deep intermediate ( $\text{BeHOD}^+$ ) well. In Fig. 4, the branching fraction for the  $\text{BeOD}^+ + \text{H}$  channel is plotted as a function of the collision energy, which shows very weak temperature dependence. At the specific collisional temperature 100 K, the fraction obtained by integrating the energy dependent branching ratio with a Boltzmann weight is 0.67, which is in reasonable agreement with the QCT results provided by Hua Guo.[?]

## 6.5 Conclusion

To summarize, chemical reactions between  $\text{Be}^+(^2\text{S}_{1/2})$  and HOD have been investigated using an integrated ion trap and highresolution TOF-MS and ZPE corrected QCT calculations on an accurate global PES. Two product channels have been observed and the branching to  $\text{BeOD}^+ + \text{H}$  is accurately determined to be  $0.58 \pm 0.14$ . The experimental result is in good agreement with ZPE corrected QCT calculation result ( $0.61 \pm 0.02$ ) as well as close to the statistical PST model ( 0.67), which reveals that the branching to the two product channels is largely due to the availability of different open states in each channel. Since their rate coefficients deviate from the capture limit as reported in our earlier work, it is clear that the  $\text{Be}^+(^2\text{S}_{1/2}) + \text{H}_2\text{O}/\text{D}_2\text{O}/\text{HOD}$  reactions have a non-negligible non-statistical component.

# CHAPTER 7

## Low Temperature C<sup>+</sup> + H<sub>2</sub>O

### 7.1 Formyl Isomer Production

In the interstellar medium, many reaction occur, in photon dominated regions (PDR's), as these are the regions where both atomic ions and molecules would coexist. At low temperatures, the rate constant of ion-dipole reactions increase, while other rates decrease or do not change, meaning ion-molecule reaction dominate in these cold (10 K - 100 K) PDR's. In particular, we are interested in the cold production of the formyl isomers (HCO<sup>+</sup> / HOC<sup>+</sup>) via C<sup>+</sup> and H<sub>2</sub>O.



Of which, we verify that the rates of reactions 7.3 and 7.4 are indistinguishable in figure 7.2 such that we may instead write:



Where [HCO]<sup>+</sup> is used to represent both isomers.

By definition, these formyl isomers of reactions eqs. (7.1) and (7.2) have identical mass and thus, cannot be readily read off by the TOF system. To be able to separate the isomer

products, we need to be able to separate their masses. By introducing a gas into the system with a proton affinity in between the isomer products, we may selectively react only one the less stable  $\text{HOC}^+$  isomer. This also yields a distinct  $m/z$  peaks originating from separate isomers as seen in reactions 7.6 and 7.8. But by using an external gas, we are doing an indirect measurement, and as such, it may add unintended complications. Certain gasses are more reactive and may react with the excited  $\text{Be}^+$ ,  $\text{C}^+$ , or any other ionized species in the trap. Another possibility is that the  $\text{COH}^+$  may isomerize due to interactions with the gas as shown in reaction 7.7.[13]



|                      | Affinity (kcal/mol) |
|----------------------|---------------------|
| CO*                  | 427                 |
| Kr                   | 425                 |
| HF                   | 490                 |
| $\text{N}_2$         | 495                 |
| Xe                   | 496                 |
| NO                   | 531                 |
| $\text{CO}_2$        | 548                 |
| $\text{CH}_4$        | 552                 |
| HCl                  | 564                 |
| HBr                  | 569                 |
| $\text{N}_2\text{O}$ | 571                 |
| *CO                  | 594                 |

Table 7.1: Proton affinities of gasses between formyl isomers where (\*) indicates H bonding location.

Since all reaction products are contained in the trap and continuously exposed to the neutral reactants, we need to consider the possibility that rate constants for reactions 7.3 and 7.4 are different. Theoretically, the differing dipole moments of the isomers would produce different dipole-dipole interactions with H<sub>2</sub>O ( $C_3$ ). Literature shows that averaged dipole moments for HCO<sup>+</sup> and HOC<sup>+</sup> are 4.6 D and 2.4 D, respectively.[?] The theoretical total rate constants for these reactions are the sum of both ADO and dipole-dipole interaction rates (2.19 + 2.7). Without averaging the dipole oriented angles for the dipole-dipole case, we would have maximal rates of  $k_{7.1} = 8.0 \times 10^{-9}$  cm<sup>3</sup>/s and  $k_{7.2} = 7.0 \times 10^{-9}$  cm<sup>3</sup>/s.

We cannot deterministically measure the rate of reaction 7.4 because there is not a way to produce only HOC<sup>+</sup>, but we may produce only HCO<sup>+</sup>. Considering reactions 7.7 and 7.6, if we let X = CO, we find that both reactions can only yield HCO<sup>+</sup>, allowing us to deterministically produce one of the isomers:



By producing only HCO<sup>+</sup>, we directly observe 7.3 with a multi-step reaction procedure. With loaded Be<sup>+</sup> and C<sup>+</sup>, the trap is exposed to H<sub>2</sub>O from the CBGB, to produce a combination of the isomers [HCO]<sup>+</sup>, all the while, CO is introduced via the leak valve in the differential cross region to a pressure of  $\approx 4 \times 10^{-9}$  Torr as measured in the trap chamber. After  $\approx 10$  s of exposure to the CBGB beam, the water beam is shuttered and the trap is exposed to the CO for an additional 5 s to ensure full conversion of HOC<sup>+</sup>  $\longrightarrow$  HCO<sup>+</sup>, after which, the leak valve is closed. The CBGB is then unshuttered so that the pure HCO<sup>+</sup> is exposed to H<sub>2</sub>O again. The second exposure of the trap to the CBGB defines the reaction time seen in Figure 7.1. A simpler procedure of continuously exposing the trap to the CBGB yields a combination of the rates of reactions 7.3 and 7.4 seen in Figure 7.2.

write about the beam density determination with BeOH+

The respective rates are found with least-squares fitting of the solutions to differential equations found in section B.3.

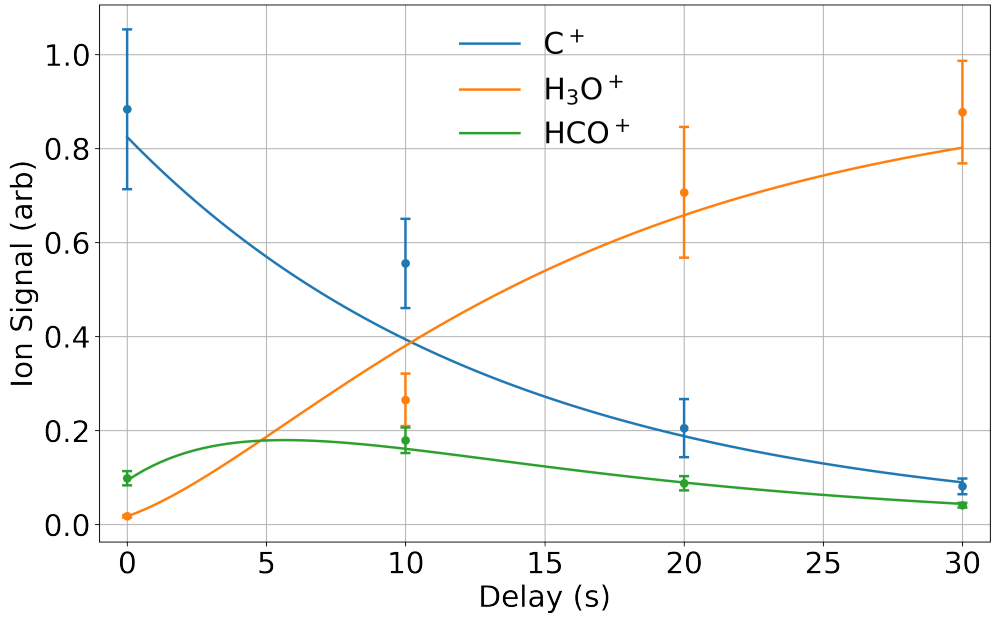


Figure 7.1: text

The resultant rate constants are

## 7.2 $\text{O}_2$ Titration

Looking at the energy difference between the two isomers, we see that

We want to figure out if the  $[\text{HCO}]^+$  isomers are still in their internally excited states, as that would change their reactivity with respect to the introduced titration gas X.

By using  $\text{O}_2$ , we can see in table 7.1, that we are only eV away from being able to react [ ] value with the more stable  $\text{HCO}^+$ . Given that the main reaction (7.1) is exothermic by 5 eV, if the molecule does not relax within the characteristic time of a collision, we may expect to see some proton exchange occur.

To start, we consider the reactions of  $\text{C}^+$  with  $\text{O}_2$ :

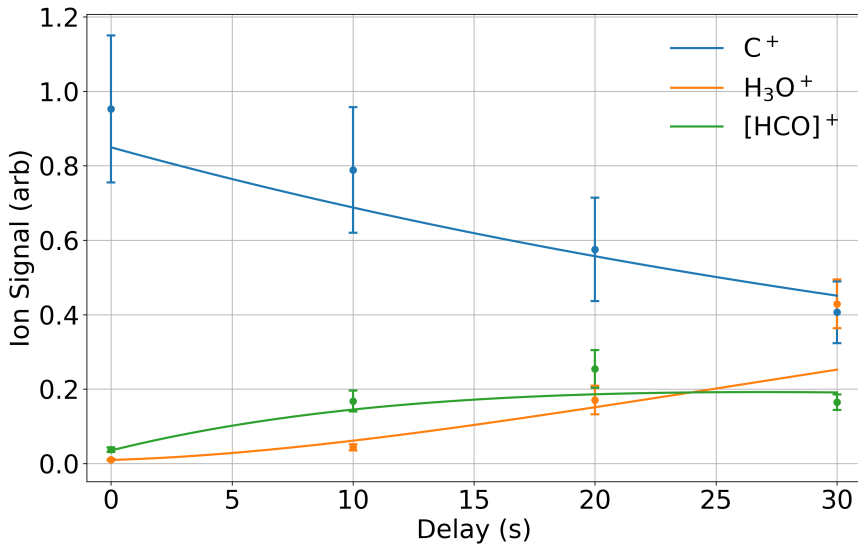


Figure 7.2: text



Where literature tells us that 7.10 7.11 both proceed at approximately  $4 \times 10^{-10} \text{ cm}^{-3}/\text{s}$ .

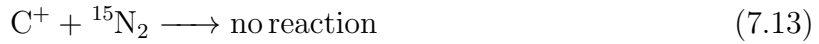
We introduce  $O_2$  into the chamber with  $Be^+$  and  $C^+$

### 7.3 $^{15}N_2$ Titration

Previous literature utilized gasses such as  $NO$ ,  $CH_4$ ,  $N_2O$ , and  $Kr$  to separate the isomers. ~~Kr~~ citations and  $Xe$  are inert and would not react with any other trapped ion but are too heavy to reliably trap after a reaction.  $NO$  is caustic and will ruin the vacuum chamber if introduced, and thus was avoided. Attempts were made with  $N_2O$  and well as  $CH_4$ , but both had their own unique complications.  $N_2O$  rapidly reacts with  $Be^+$  and made reliable TOF traces unattainable due to the loss of the coolant ion.  $CH_4$  readily reacted with most of the ions in the trap to produce a multitude of mass peaks, greatly complicating the analysis.

Normally N<sub>2</sub> would not be a good choice, due to the fact that N<sub>2</sub>H<sup>+</sup> has the same mass as the formyl isomers at  $m/z = 29$ , but we may instead introduce <sup>15</sup>N<sub>2</sub> to produce a new peak at  $m/z = 31$ .

We do not expect and do not see any reaction between the initially loaded ions of Be<sup>+</sup> and C<sup>+</sup>. But according to section 7.1, we should still have a separation of the isomers, thus:



To verify reaction 7.9, trapped Be<sup>+</sup> and C<sup>+</sup> ions are exposed to the water from the CBGB at a density of  $4.3 \times 10^6 \text{ cm}^{-3}$  while simultaneously flooded with  $\approx 3 \times 10^7 \text{ cm}^{-3}$  of CO from the leak valve connected to the differential pumping region such that  $k_{7.9} \gg k_{7.1,7.2}$ . After 10 s, the gate valve between the differential pumping and experimental ion chamber regions is manually closed, after which,  $10^9 \text{ cm}^{-3}$  of <sup>15</sup>N<sub>2</sub> is introduced for 10 s. A TOF trace for this procedure is shown in figure 7.3.

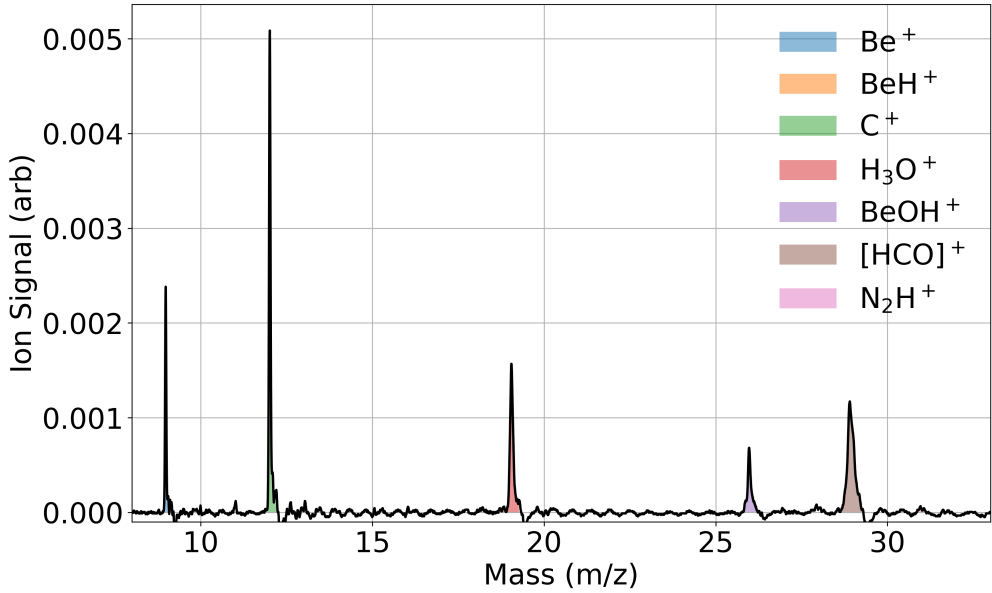


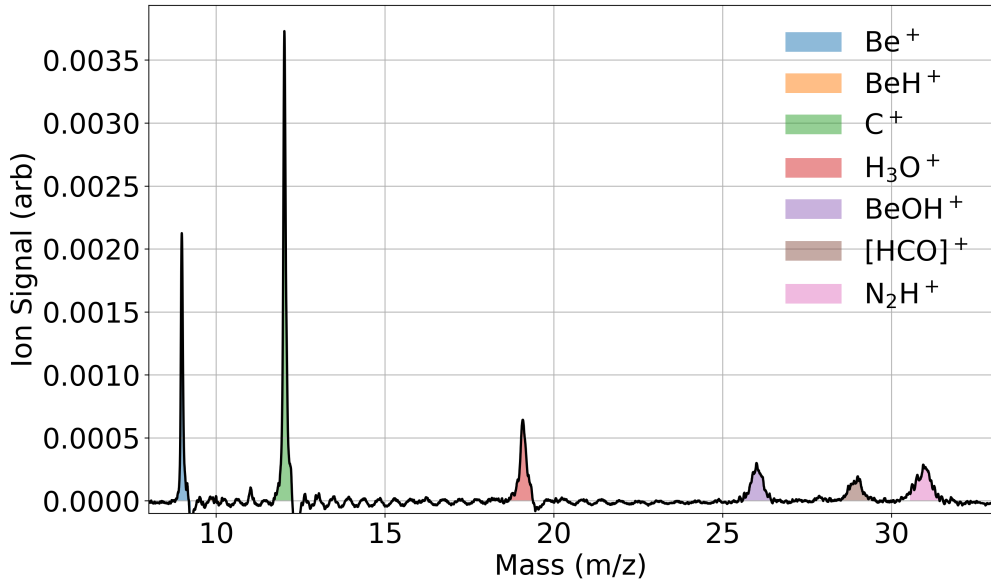
Figure 7.3: TOF trace of reaction products of  $\text{Be}^+$  and  $\text{C}^+$  after exposure to both water from the CBGB beam, and CO (10 s) before titration with  $^{15}\text{N}_2$  (10 s). There is a distinct lack of  $\text{N}_2\text{H}^+$ , indicating full conversion of  $\text{HOC}^+ \longrightarrow \text{HCO}^+$ .

Integrated  $\text{N}_2\text{H}^+$  signal was found to be below the threshold for null signal demonstrating both points that reaction 7.9 proceeds as expected, as well as experimental verification that reaction 7.14 does not occur.

### 7.3.1 Branching Ratio Determination

At room temperatures, the branching ratio has been found to be approximately 84:16 ( $\text{COH}^+:\text{HCO}^+$ )[14], but unexplored at lower regimes.

To determine the branching ratio,  $\text{Be}^+$  and  $\text{C}^+$  in the trap are exposed to the CBGB for 10 s, after which, the gate valve connecting the differential pumping region and ion trap chamber is closed.  $^{15}\text{N}_2$  is then introduced via leak valve to react with the  $\text{HOC}^+$ . Only runs taken at delay times of 10 s were taken, as we only concern ourselves with a ratio of signals.



Repeating this process over various densities of  $^{15}\text{N}_2$  allows us to determine the isomer branching ratio. We expect the ratio of  $\text{N}_2\text{H}^+$  and  $[\text{HCO}]^+$  to follow the form:

$$\eta(t) = C \left(1 - e^{-k_{7.6}\rho t}\right) \quad (7.16)$$

Where we define  $\eta(t) \equiv \frac{^{15}\text{N}_2\text{H}^+(t)}{^{15}\text{N}_2\text{H}^+(t) + [\text{HCO}]^+(t)}$ . A fit performed on the data over various densities yields a rate constant of  $k_{7.6} = ((6.2 \pm 1.0) \times 10^{-10}) \text{ cm}^3/\text{s}$ , and a final branching ratio of  $\text{HOC}^+ : \text{HCO}^+ = 0.58 \pm 0.02$ .

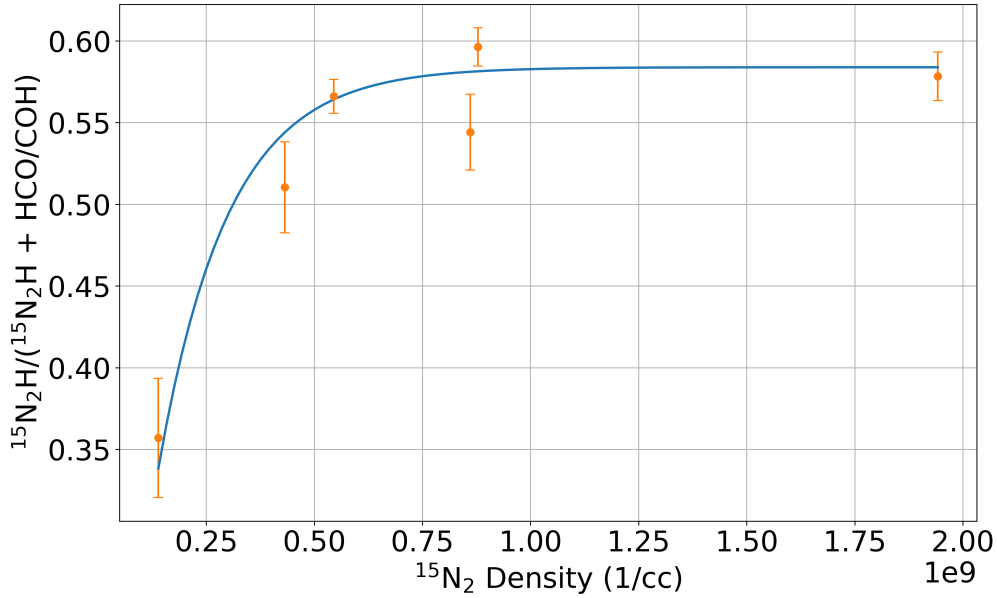


Figure 7.4:  $^{15}\text{N}_2$  introduced into the ion chamber after trapped  $\text{Be}^+$  and  $\text{C}^+$  are exposed to water from the CBGB for set times.

With this fit, we may consider putting bounds on the rate of isomerization by comparing the theoretical rate constant for reaction 7.6 with the fitted value. If reaction 7.7 plays a role, it will proportionally affect the total rate constant. We find the Langevin rate for  $\text{HOC}^+ + ^{15}\text{N}_2$  to be  $k_L = 8.0 \times 10^{-10} \text{ cm}^3/\text{s}$

To estimate a limit on the isomerization, we consider the above reaction eqs. (7.7) and (7.6), where  $\text{X} = ^{15}\text{N}_2$  in the context that we can only determine the abundance of  $[\text{HCO}]^+$  and  $^{15}\text{N}_2\text{H}^+$ . As a function of pressure, we cannot see reaction 7.7, but if it does contribute, we should see a discrepancy in the total rate constant, which we estimate to be Langevin:  $k_L = 8.0 \times 10^{-10}$ . This gives us a possible isomerization rate of 22%, which then yield a branching ratio of 70:30

# CHAPTER 8

## Conclusion and Future Outlook

The experiment has broken new ground in ion-molecule reactions at various reaction temperatures, but there is still much left unexplored. The recent inclusion of two Lioptec dye lasers will allow for more stuff and stuff.

Also stereodynamics with molecules or just atoms

We have only been exciting the  $\text{Be}^+$  into the  ${}^2\text{P}_{3/2}$  state because it is easier than the  ${}^2\text{P}_{1/2}$  manifold, but that would allow us to possibly see fine structure dependent rates and dynamics.

## APPENDIX A

### Pressure Calibration

To be able to calculate rate constants, we need to have an accurate measure of the absolute pressure of the gas of interest. This is easier said than done, various instruments may have different absolute readings and uncertainties and may not agree with one another *in situ*. To find the relative pressures of multiple gasses introduced into the chamber, we use the RGA, but Stanford Research Systems does not provide an uncertainty for its device's absolute accuracy. We calibrate it by cross-correlating our RGA measurements with the total pressure measured by an Agilent UHV-24 Bayard-Alpert Gauge Tube, which gives a quoted  $< 10\%$  error at  $5 \times 10^{-10}$  Torr (our normal operating pressure). The fact that the ion gauge is set in a nipple connected to the chamber provides at least another 30% uncertainty, but is more acceptable than the completely unknown reliability of the RGA.

The calibration consists of incrementally adding either H<sub>2</sub> or H<sub>2</sub>O into the chamber and read off the pressures from the RGA as well as the ion gauge (scaled by their species dependent specifications). By fitting the relationship between these two readings, we find that there is a mass dependent scaling factor for the RGA to ion gauge pressure shown in Figure A.1. H<sub>2</sub>O is scaled by 1.1, while H<sub>2</sub> is much less accurate, and scaled by 0.59. Using this calibrated pressure reading, our measured Be<sup>+</sup> + H<sub>2</sub> reaction rate coefficient of  $1.2 \pm 0.3_{\text{stat}} \times 10^{-9} \text{ cm}^3/\text{s}$  agrees with the literature seen in Figure A.2.

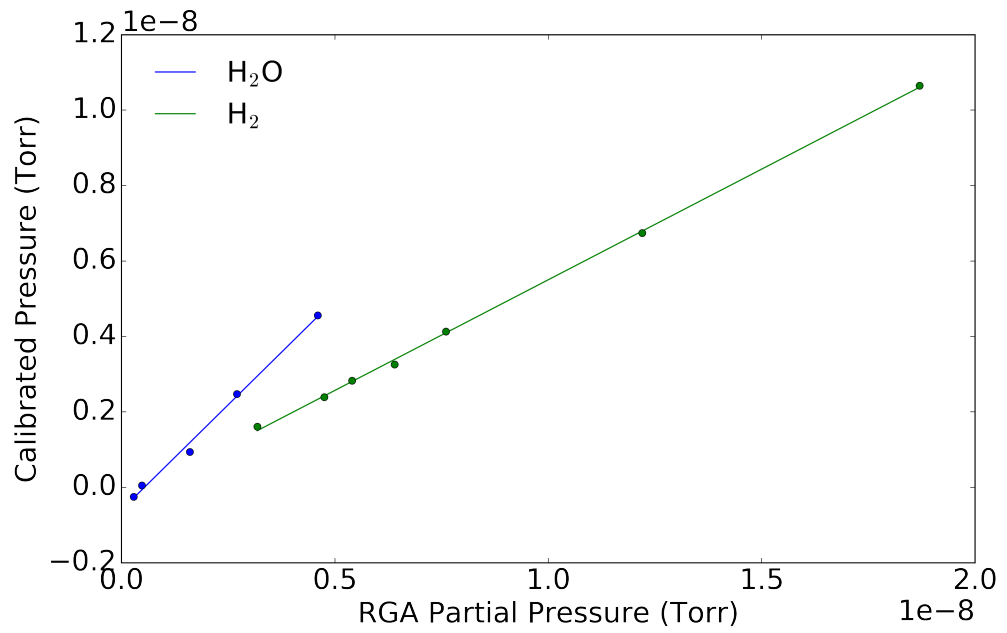


Figure A.1: Fitted curves for  $\text{H}_2$  and  $\text{H}_2\text{O}$  detection between the ion gauge and RGA. The reported pressure between the ion gauge and RGA is nearly identical for  $\text{H}_2\text{O}$  with a slope of 1.1, but noticeably different for  $\text{H}_2$  with a slope of 0.59.

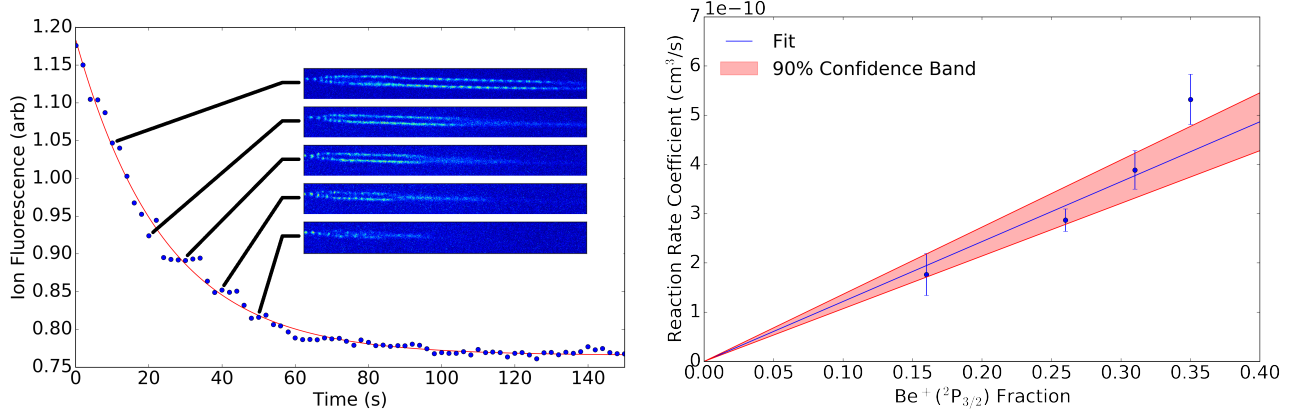


Figure A.2: (A) A typical fluorescence decay measurement of  $\text{Be}^+ + \text{H}_2$ . The inset images are a subset of the original ion fluorescence images recorded by the camera. The red curve is an exponential fit (with a free offset) to the data, which gives the total reaction rate. (B) A fit of  $\text{Be}^+ + \text{H}_2$  fluorescence decay at various P state excitation fractions. A statistical rate coefficient for full excitation of  $(1.2 \pm 0.3_{\text{state}}) \times 10^{-9} \text{ cm}^3/\text{s}$  is in agreement with existing literature.

## APPENDIX B

### Chemical Rate Equations

Rate equations used in the shared fitting programs.

#### B.1 $\text{Be}^+ + \text{H}_2\text{O} + \text{H}_2$

Differential forms for reactions 4.7, 5.6, 5.1, and 5.2 occurring concurrently:

$$\dot{\text{Be}}(t) = (-k_1\rho_1 + k_2\rho_2)\text{Be}(t) \quad (\text{B.1})$$

$$\dot{\text{BeH}}(t) = k_1\rho_1\text{Be}(t) - k_3\rho_2\text{BeH}(t) \quad (\text{B.2})$$

$$\dot{\text{BeOH}}(t) = k_2\rho_2\text{Be}(t) + k_3\rho_3\text{BeH}(t) \quad (\text{B.3})$$

Where  $\rho_1$  is the density of  $\text{H}_2$  and  $\rho_2$  is the density of  $\text{H}_2\text{O}$ . The solutions are as follows:

$$\text{Be}(t) = \text{Be}_0 e^{t(-(k_1\rho_1 + k_2\rho_2))} \quad (\text{B.4})$$

$$\text{BeH}(t) = \frac{1}{\rho_2(k_3 - k_2) - k_1\rho_1} \left[ e^{-k_3\rho_2 t} (\text{Be}_0 k_1 \rho_1 (e^{-(k_1\rho_1 + k_2\rho_2 - k_3\rho_2)t} - 1) \right. \quad (\text{B.5})$$

$$- \left. \text{BeH}_0 (k_1\rho_1 + \rho_2(k_2 - k_3)) \right] \quad (\text{B.6})$$

$$\text{BeOH}(t) = \frac{e^{-k_3\rho_2 t}}{\rho_2(k_3 - k_2) - k_1\rho_1} \left[ \text{Be}_0 (k_1\rho_1 - (k_1\rho_1 + k_2\rho_2 - k_3\rho_2)) e^{k_3\rho_2 t} \right. \quad (\text{B.7})$$

$$+ \left. \rho_2(k_2 - k_3) e^{-(k_1\rho_1 + \rho_2(k_2 - k_3))t} \right] \quad (\text{B.8})$$

$$+ ((\text{BeH}_0 + \text{BeOH}_0) e^{k_3\rho_2 t} - \text{BeH}_0) (\rho_2(k_3 - k_2) - k_1\rho_1) \quad (\text{B.9})$$

## B.2 Be<sup>+</sup> + H<sub>2</sub>O/HOD/D<sub>2</sub>O

Differential forms for reactions 5.1, 6.8, 6.9, and 6.10 occurring concurrently:

$$\dot{Be}(t) = -(k_1\rho_1 + k_2\rho_2 + k_3\rho_3)Be(t) \quad (B.10)$$

$$\dot{BeOH}(t) = (k_1\rho_1 + (1 - \eta)k_2\rho_2)Be(t) \quad (B.11)$$

$$\dot{BeOD}(t) = (k_3\rho_3 + \eta k_2\rho_2)Be(t) \quad (B.12)$$

Where  $\rho_1$  is the density of H<sub>2</sub>O,  $\rho_2$  is the density of HOD, and  $\rho_3$  is the density of D<sub>2</sub>O.

The solutions are as follows:

$$Be(t) = Be_0 e^{-(k_1\rho_1 + k_2\rho_2 + k_3\rho_3)t} \quad (B.13)$$

$$BeOD(t) = \frac{1}{k_1\rho_1 + k_2\rho_2 + k_3\rho_3} [Be_0(\eta k_2\rho_2 + k_3\rho_3)(1 - e^{-(k_1\rho_1 + k_2\rho_2 + k_3\rho_3)t}) + BeOD_0(k_1\rho_1 + k_2\rho_2 + k_3\rho_3)] \quad (B.14)$$

$$BeOH(t) = \frac{1}{k_1\rho_1 + k_2\rho_2 + k_3\rho_3} [Be_0(k_1\rho_1 - (\eta - 1)k_2\rho_2)(1 - e^{-(k_1\rho_1 + k_2\rho_2 + k_3\rho_3)t}) + BeOH_0(k_1\rho_1 + k_2\rho_2 + k_3\rho_3)] \quad (B.16)$$

$$+ BeOH_0(k_1\rho_1 + k_2\rho_2 + k_3\rho_3)] \quad (B.17)$$

## B.3 C<sup>+</sup> + H<sub>2</sub>O

Differential forms for 7.1, 7.2, and 7.5.

$$\dot{C}(t) = -k_1\rho C(t) \quad (B.18)$$

$$[\dot{HCO}](t) = \rho(k_1C(t) + k_2[HCO](t)) \quad (B.19)$$

$$\dot{H_3O}(t) = k_2\rho[HCO](t) \quad (B.20)$$

Where  $\rho$  is the density of H<sub>2</sub>O. The solutions are as follows:

$$C(t) = C_0 e^{-k_1 \rho t} \quad (B.21)$$

$$[HCO](t) = \frac{e^{-(k_1+k_2)\rho t}}{k_1 - k_2} (e^{k_1 \rho t} ((C_0 + [HCO]_0)k_1 - [HCO]_0 k_2) - C_0 e^{-(k_1+k_2)\rho t}) \quad (B.22)$$

$$H_3O(t) = H_3O_0 + [HCO]_0(1 - e^{-k_2 \rho t}) + \frac{C_0 (k_1 (1 - e^{-k_2 \rho t}) + k_2 (e^{-k_1 \rho t} - 1))}{k_1 - k_2} \quad (B.23)$$

## REFERENCES

- [1] N. G. Adams and D. Smith. The selected ion flow tube (SIFT); A technique for studying ion-neutral reactions. *International Journal of Mass Spectrometry and Ion Physics*, 21(3-4):349–359, 1976.
- [2] Marcelino Agúndez and Valentine Wakelam. Chemistry of Dark Clouds: Databases, Networks, and Models. *Chemical Reviews*, 113(12):8710–8737, 2013.
- [3] PB Armentrout. Reactions and Thermochemistry of Small Transition Metal Cluster Ions. *Annual Review of Physical Chemistry*, 52(1):423–461, 2002.
- [4] J J Bollinger, J S Wells, D J Wineland, and Wayne M Itano. Hyperfine structure of the  $2p^2P_{1/2}$  state in  ${}^9\text{Be}^+$ . *Physical Review A*, 31(4):2711–2714, 1985.
- [5] Michael J. Bronikowski, William R. Simpson, Bertrand Girard, and Richard N. Zare. Bond-specific chemistry: OD:OH product ratios for the reactions H+HOD(100) and H+HOD(001). *Journal of Chemical Physics*, 95(11):8647–8648, 1991.
- [6] Eduardo Carrascosa, Jennifer Meyer, and Roland Wester. Imaging the dynamics of ion-molecule reactions. *Chemical Society Reviews*, 46(24):7498–7516, 2017.
- [7] Kuang Chen, Scott T. Sullivan, and Eric R. Hudson. Neutral gas sympathetic cooling of an ion in a Paul trap. *Physical Review Letters*, 112(14):1–5, 2014.
- [8] Kuang Chen, Scott T. Sullivan, Wade G. Rellergert, and Eric R. Hudson. Measurement of the coulomb logarithm in a radio-frequency Paul trap. *Physical Review Letters*, 110(17):1–5, 2013.
- [9] D. C Clary. Fast Chemical Reactions: Theory Challenges Experiment. *Annual Review of Physical Chemistry*, 41(1):61–90, 1990.
- [10] F. Fleming Crim. Bond-selected chemistry: Vibrational state control of photodissociation and bimolecular reaction. *Journal of Physical Chemistry*, 100(31):12725–12734, 1996.
- [11] N. F. Dalleska, Kevin C. Crellin, and P. B. Armentrout. Reactions of alkaline earth ions with hydrogen, deuterium, and hydrogen deuteride. *The Journal of Physical Chemistry*, 97(13):3123–3128, 2005.
- [12] C. E. Dateo and D. C. Clary. Rate constant calculations on the  $\text{C}^+ + \text{HCl}$  reaction. *The Journal of Chemical Physics*, 1989.
- [13] Colin G. Freeman, John S. Knight, Jonathan G. Love, and Murray J. McEwan. The reactivity of  $\text{HOC}^+$  and the proton affinity of CO at O. *International Journal of Mass Spectrometry and Ion Processes*, 80(C):255–271, 1987.

- [14] Colin G. Freeman and Murray J. McEwan. A selected-ion flow tube study of the  $\text{C}^+ + \text{H}_2\text{O}$  reaction. *International Journal of Mass Spectrometry and Ion Processes*, 75(1):127–131, 1987.
- [15] Bina Fu and Dong H. Zhang. A full-dimensional quantum dynamics study of the mode specificity in the  $\text{H} + \text{HOD}$  abstraction reaction. *Journal of Chemical Physics*, 142(6), 2015.
- [16] George Gioumousis and D. P. Stevenson. Reactions of gaseous molecule ions with gaseous molecules. V. theory. *The Journal of Chemical Physics*, 29(2):294–299, 1958.
- [17] Anders K. Hansen, Magnus A. Sørensen, Peter F. Staanum, and Michael Drewsen. Single-ion recycling reactions. *Angewandte Chemie - International Edition*, 51(32):7960–7962, 2012.
- [18] William L. Hase, Jochen Mikosch, Roland Wester, Jiaxu Zhang, Rico Otto, and Jing Xie. Identification of Atomic-Level Mechanisms for Gas-Phase  $\text{X}^- + \text{CH}_3 \rightarrow \text{S}_{\text{N}}2$  Reactions by Combined Experiments and Simulations. *Accounts of Chemical Research*, 47(10):2960–2969, 2014.
- [19] J L Highberger, C Savage, J H Bieging, and L M Ziurys. HEAVY-METAL CHEMISTRY IN PROTO-PLANETARY NEBULAE: DETECTION OF MgNC, NaCN, AND AlF TOWARD CRL 2688. *the Astrophysical Journal*, 562:790–798, 2001.
- [20] W. T. Huntress and R. F. Pinizzotto. Product distributions and rate constants for ion-molecule reactions in water, hydrogen sulfide, ammonia, and methane. *The Journal of Chemical Physics*, 59(9):4742–4756, 2004.
- [21] Nicholas R Hutzler, Hsin-I Lu, and John M Doyle. The buffer gas beam: an intense, cold, and slow source for atoms and molecules. *Chemical reviews*, 112(9):4803–27, sep 2012.
- [22] NR Nicholas R Hutzler, MF Maxwell F Parsons, Yulia V Gurevich, Paul W Hess, Elizabeth Petrik, Ben Spaun, Amar C Vutha, David Demille, Gerald Gabrielse, and John M Doyle. A cryogenic beam of refractory, chemically reactive molecules with expansion cooling. . . . *Chemistry Chemical . . .*, 13(42):1–16, 2011.
- [23] Vladimir A Krasnopolsky. Chemical composition of Titan’s atmosphere and ionosphere: Observations and the photochemical model. *Icarus*, 236:83–91, 2014.
- [24] D. J. Larson, J. C. Bergquist, J. J. Bollinger, Wayne M. Itano, and D. J. Wineland. Sympathetic cooling of trapped ions: A laser-cooled two-species nonneutral ion plasma. *Physical Review Letters*, 57(1):70–73, 1986.
- [25] Adan Li, Jianzheng Song, Yang Sun, and Tifeng Jiao. The application of resonance-enhanced multiphoton ionization technique in gas chromatography mass spectrometry. *Journal of Spectroscopy*, 2014, 2014.

- [26] Jun Li, Bin Jiang, and Hua Guo. Spin-orbit corrected full-dimensional potential energy surfaces for the two lowest-lying electronic states of  $\text{FH}_2\text{O}$  and dynamics for the  $\text{F} + \text{H}_2\text{O} \rightarrow \text{HF} + \text{OH}$  reaction. *Journal of Chemical Physics*, 138(7), 2013.
- [27] Jun Li, Bin Jiang, Hongwei Song, Jianyi Ma, Bin Zhao, Richard Dawes, and Hua Guo. From ab initio potential energy surfaces to state-resolved reactivities:  $\text{X} + \text{H}_2\text{O} \leftrightarrow \text{HX} + \text{OH}$  [ $\text{X} = \text{F}, \text{Cl}$ , and  $\text{O}({}^3\text{P})$ ] reactions. *Journal of Physical Chemistry A*, 119(20):4667–4687, 2015.
- [28] U. Lourderaj, M. Weidemuller, W. L. Hase, J. Mikosch, R. Otto, R. Wester, C. Eichhorn, J. X. Zhang, and S. Trippel. Imaging Nucleophilic Substitution Dynamics. *Science*, 319(5860):183–186, 2008.
- [29] Ricardo B. Metz, John D. Thoemke, Joann M. Pfeiffer, and F. Fleming Crim. Selectively breaking either bond in the bimolecular reaction of  $\text{HOD}$  with hydrogen atoms. *Journal of Chemical Physics*, 99(3):1744–1751, 1993.
- [30] Edvardas Narevicius, Adam Libson, Christian G. Parthey, Isaac Chavez, Julia Narevicius, Uzi Even, and Mark G. Raizen. Stopping supersonic oxygen with a series of pulsed electromagnetic coils: A molecular coilgun. *Physical Review A - Atomic, Molecular, and Optical Physics*, 77(5):1–4, 2008.
- [31] M. Oppenheimer and A. Dalgarno. The Fractional Ionization in Dense Interstellar Clouds. *The Astrophysical Journal*, 192(12):29, 2002.
- [32] Hans Pauly. *Atom, Molecule, and Cluster Beams I: Basic Theory, Production and Detection of Thermal Energy Beams*, volume 28. Springer, 2000.
- [33] Amelia W. Ray, Jianyi Ma, Rico Otto, Jun Li, Hua Guo, and Robert E. Continetti. Effects of vibrational excitation on the  $\text{F} + \text{H}_2\text{O} \rightarrow \text{HF} + \text{OH}$  reaction: Dissociative photodetachment of overtone-excited  $[\text{F}-\text{H}-\text{OH}]^-$ . *Chemical Science*, 8(11):7821–7833, 2017.
- [34] B. Roth, P. Blythe, H. Wenz, H. Daerr, and S. Schiller. Ion-neutral chemical reactions between ultracold localized ions and neutral molecules with single-particle resolution. *Physical Review A - Atomic, Molecular, and Optical Physics*, 73(4):1–9, 2006.
- [35] Christian Schneider, Steven J. Schowalter, Kuang Chen, Scott T. Sullivan, and Eric R. Hudson. Laser-Cooling-Assisted Mass Spectrometry. *Physical Review Applied*, 2(3):1–7, 2014.
- [36] Steven J. Schowalter, Kuang Chen, Wade G. Rellergert, Scott T. Sullivan, and Eric R. Hudson. An integrated ion trap and time-of-flight mass spectrometer for chemical and photo- reaction dynamics studies. *Review of Scientific Instruments*, 83(4), 2012.
- [37] Steven J. Schowalter, Alexander J. Dunning, Kuang Chen, Prateek Puri, Christian Schneider, and Eric R. Hudson. Blue-sky bifurcation of ion energies and the limits of neutral-gas sympathetic cooling of trapped ions. *Nature Communications*, 7:1–8, 2016.

- [38] Ian R Sims. Gas-Phase Reactions and Energy Transfer at Very Low Temperatures. *Annual Review of Physical Chemistry*, 46(1):109–137, 2002.
- [39] Amitabha Sinha, Mark C. Hsiao, and F. Fleming Crim. Bond-selected bimolecular chemistry:  $\text{H} + \text{HOD}(4\nu_{\text{OH}}) \rightarrow \text{OD} + \text{H}_2$ . *The Journal of Chemical Physics*, 92(10):6333–6335, 1990.
- [40] Dimitris Skouteris, David E. Manolopoulos, Wensheng Bian, Hans Joachim Werner, Lih Huey Lai, and Kopin Liu. Van der Waals interactions in the Cl + HD reaction. *Science*, 286(5445):1713–1716, 1999.
- [41] I. W M Smith and Bertrand R. Rowe. Reaction kinetics at very low temperatures: Laboratory studies and interstellar chemistry. *Accounts of Chemical Research*, 33(5):261–268, 2000.
- [42] Theodore P. Snow and Veronica M. Bierbaum. Ion Chemistry in the Interstellar Medium. *Annual Review of Analytical Chemistry*, 1(1):229–259, 2008.
- [43] Hongwei Song and Hua Guo. Vibrational and Rotational Mode Specificity in the Cl + H<sub>2</sub>O → HCl + OH Reaction: A Quantum Dynamical Study. *Journal of Physical Chemistry A*, 119(24):6188–6194, 2015.
- [44] Hongwei Song, Soo Ying Lee, Yunpeng Lu, and Hua Guo. Full-Dimensional Quantum Dynamical Studies of the Cl + HOD → HCl/DCl + OD/OH Reaction: Bond Selectivity and Isotopic Branching Ratio. *Journal of Physical Chemistry A*, 119(50):12224–12230, 2015.
- [45] Timothy Su and Michael T. Bowers. Ion-polar molecule collisions: the effect of ion size on ion-polar molecule rate constants; the parameterization of the average-dipole-orientation theory. *International Journal of Mass Spectrometry and Ion Physics*, 12(4):347–356, 1973.
- [46] Timothy Su and Michael T. Bowers. Theory of ion-polar molecule collisions. Comparison with experimental charge transfer reactions of rare gas ions to geometric isomers of difluorobenzene and dichloroethylene. *The Journal of Chemical Physics*, 58(7):3027–3037, 1973.
- [47] Timothy Su and Michael T. Bowers. Ion-polar molecular collisions: the average quadrupole orientation theory. *International Journal of Mass Spectrometry and Ion Physics*, 17(3):309–319, 1975.
- [48] J. Troe. Statistical adiabatic channel model of ion-neutral dipole capture rate constants. *Chemical Physics Letters*, 122(5):425–430, 1985.
- [49] Ewine F. van Dishoeck, Eric Herbst, and David A. Neufeld. Interstellar Water Chemistry: From Laboratory to Observations. *Chemical Reviews*, 113(12):9043–9085, 2013.

- [50] D. J. Wineland and Wayne M. Itano. Laser cooling of atoms. *Physical Review A*, 20(4):1521–1540, 1979.
- [51] Paul Wolfgang. Electromagnetic Traps For charged And Neutral Particles, 1990.
- [52] Chunlei Xiao, Xin Xu, Shu Liu, Tao Wang, Wenrui Dong, Tiangang Yang, Zhigang Sun, Dongxu Dai, Xin Xu, Dong H Zhang, and Xueming Yang. Experimental and theoretical differential cross sections for a four-atom reaction:  $\text{HD} + \text{OH} \rightarrow \text{H}_2\text{O} + \text{D}$ . *Science*, 333(6041):440–442, 2011.
- [53] Tiangang Yang, Anyang Li, Gary K Chen, Changjian Xie, Arthur G Suits, Wesley C Campbell, Hua Guo, and Eric R Hudson. Optical Control of Reactions between Water and Laser-Cooled  $\text{Be}^+$  Ions. *J. Phys. Chem. Lett.*, 9:28, 2018.
- [54] Richard N. Zare. Laser Control of Chemical Reactions. *Science*, 279(5358):1875–1879, 1998.
- [55] Dong H Zhang and John C Light. Full-dimensional quantum study. 93(5):691–697, 1997.
- [56] Dongdong Zhang and Stefan Willitsch. Cold ion chemistry. 2017.
- [57] Rui Zheng, Yongfa Zhu, and Hongwei Song. Mode specific dynamics in bond selective reaction  $\text{O}'(^3\text{P}) + \text{HOD} \rightarrow \text{O}'\text{H} + \text{OD}/\text{O}'\text{D} + \text{OH}$ . *Journal of Chemical Physics*, 149(5), 2018.